Experimental Investigations of the Transport Properties of Flow Suspensions

I: Measurement of Velocity Distributions of Suspension Flows in a Rectangular Channel.

II: Experimental Study of the Effective Thermal Conductivity in Shear Flow of a Suspension.

III: The Use of Fluorescence Correlation Spectroscopy to Measure Molecular Diffusion and Velocity Distributions.

by

Ernest Ying-Chee Chung

In Partial Fulfillment of the Requirements
for the Degree of Doctor of Philosophy

California Institute of Technology
Pasadena, California

1980

(Submitted December 20, 1979)

Acknowledgment

Many people have contributed to the completion of this thesis and deserve special recognition.

It is with great pleasure that I acknowledge the guidance and support of my research advisor, Dr. W. H. Corcoran. I am appreciative of his confidence in me and the freedom allowed me in my research. His infinite kindness and patience made my stay at Caltech truly enjoyable.

I would also like to acknowledge the assistance of my research advisor, Dr. L. G. Leal, who provided invaluable insights and suggestions and made this work possible.

Special thanks must go to George Griffith, Henry Smith, Seichi Nakawatase, John Yehle and Ray Reed for their technical assistance in the design and fabrication of equipment and in the laboratory. Their kindness and friendship have greatly enriched my life.

I am grateful to Dr. N. George for his assistance in the analysis on the use of fluorescent tracers to measure velocity, to Dr. A. Rembaum of the Jet Propulsion Laboratory for supplying the fluorescent tracers, and to the American Red Cross for supplying the outdated blood used in the experiments.

I gratefully acknowledge the Donald E. Baxter Foundation for financial support of my research.

The experiments were made possible with the assistance of Kris Larson, Hock Chuen So and Hon Chung Lau.

I am very grateful to Kathy Lewis for the excellent job of typing the thesis.

Abstract

This study was directed towards the understanding of transport properties of flowing suspensions. The first part of the thesis detailed the experimental study undertaken to investigate the characteristics of flowing suspensions. An experimental method capable of measuring the velocities of both the dispersed and suspending phases of a flowing suspension was first developed. The method was shown to be capable of measuring the velocity distributions of moderately concentrated suspensions. By using a modified laser Doppler anemometer, the velocity distribution of the suspended fluid was approximated by measuring the velocity of small fluorescent tracers, while the scattered signal from the suspended particles gave a direct measurement of their velocity distribution. Suspensions of rigid latex spheres, red blood cells, and ghost red blood cells were used. The observed behavior of the different suspensions were similar. However, the behavior of suspensions of rigid latex spheres showed a stronger dependence on the concentration of suspended particles, and a dependence on flow rates which was not observed with suspensions of ghost cells.

The second part of the thesis describes the measurements of the effective thermal conductivity of sheared suspensions of rigid spherical particles. The objective was to verify the theoretical prediction of Leal (1973) for a dilute suspension undergoing shear at low particle Peclet number, and to extend the range of the experiments to conditions beyond the scope of the theory. Surprisingly, reasonable agreement with the theoretical prediction was observed even for suspensions of moderate concentrations ($\phi \leq 0.25$) and higher Peclet numbers ($Pe \sim O(1)$). The trend of the data,

however, verifies the obvious fact that the theory does not completely describe the transport behavior at higher concentrations and Peclet numbers. The range of quantitative applicability of Leal's result is apparently only for $Pe < 0.01$ and $\phi < 0.01$, but the changes in the effective thermal conductivity in this domain were too small to be measured in our apparatus.

In the third part of the thesis, an analysis on the use of fluorescence correlation spectroscopy to measure molecular diffusion and velocity distributions in a sheared flow is presented. The superior spatial resolution of the method allows local measurements of molecular diffusion and/or velocity distributions. The method can also be used to measure self-diffusion of the suspended particles in a sheared suspension.

Table of Contents

		Page
Part I:	Measurement of Velocity Distributions of Suspension Flows in a Rectangular Channel	1
	I. Introduction	2
	II. Literature Review	5
	III. Objectives	12
	IV. Experimental Approach	13
	V. Results and Discussions	44
	VI. Conclusions	51
	VII. Suggestions for Future Work	51
	References	54
	Appendices I—IV	59
	Figures	87
Part II:	Experimental Study of the Effective Thermal Conductivity in Shear Flow of a Suspension of Rigid Spherical Particles	112
	I. Introduction	113
	II. Theoretical Background	115
	III. Objectives of the Experimental Study	118
	IV. Experimental Apparatus and Procedure	120
	V. Derivation of the Operating Equations	124
	VI. Error Analysis	133
	VII. Experimental Results and Discussion	135

Table of Contents (continued)

Page

VIII. Conclusion 149

Appendices 150

Nomenclature 172

References 174

Tables 176

Figures 181

Part III: The Use of Fluorescence Correlation Spectroscopy to Measure Molecular Diffusion and Velocity Distribution. . . 199

Part I: Measurement of Velocity Distributions of Suspension Flows in a Rectangular Channel.

I. Introduction

The rheological behavior of suspensions, a disperse system of rigid or deformable particles in a continuous phase, covers a wide range of areas of technical importance. Some examples are the dynamics of pollutant separation, flow through fluidized beds, transport through the flow of blood in biological systems, and the flow of macromolecular solutions.

Suspensions are generally treated as homogeneous fluids whenever the length scales describing the macroscopic behavior of the entire system are much larger than either the average particle size or the average separation distance between particles. This condition is very often satisfied because of the smallness of the particles encountered in most suspensions. When the suspension is treated as homogeneous, it is characterized by effective fluid properties.

Indeed, one long-standing problem in the study of heterogeneous dispersions has been the determination of its effective rheological properties. Einstein (see Einstein, 1956) first calculated the effective viscosity of a dilute suspension in terms of the properties of its constituents. Since then a large body of experimental and theoretical work on the rheological properties of suspensions has been performed. It has become clear that many of the complex phenomena associated with a flowing suspension cannot be explained by assuming that the suspension acts like a Newtonian fluid with an effective viscosity. In fact, suspensions frequently exhibit such rheological anomalies as non-Newtonian viscosity and time-dependent thixotropy. These rheological anomalies are often a result of the hydrodynamic and nonhydrodynamic forces on the particles in suspension. The nonhydrodynamic forces include thermal (Brownian) forces,

electrical forces arising from charges on the particles and London van der Waals forces, as described by the Deryagin-Landau-Verwey-Overbeek theory. Interactions between the particles, inertia forces acting on the particles as well as the shape and deformation of the particles also contribute to the non-Newtonian behavior of suspensions. The results of recent experimental and theoretical studies can be found in a number of review articles (Jeffrey and Acrivos, 1976; Jinescu, 1974; Krieger, 1972; Batchelor, 1974; Brenner, 1972) and will not be repeated here.

Of equal importance to the study of suspensions is the mechanics of flow of suspensions with moderate to high concentrations of suspended particles. Dilute suspensions of rigid spherical particles with a Newtonian suspending fluid are known to be Newtonian rheologically. When the concentration of the dispersed phase goes beyond the dilute limit, however, the behavior of a suspension undergoing flow cannot be predicted solely by an effective viscosity. For example, when suspensions with a moderate concentration of rigid spherical particles (volume fraction of particles, $\phi \leq 0.20$) suspended in a Newtonian fluid undergo flow in a circular tube, the radial velocity distribution deviates from that of the well-known Poiseuille profile, even when the effective viscosity, when measured either in tubes or in Couette viscometers, shows no dependence on shear rate (Karnis et al., 1966; Krieger, 1972). A knowledge of the velocity distributions of both phases and the concentration distribution of the suspended particles is therefore important to the understanding of the fluid mechanics and energy and mass transport properties of flowing suspensions. Such knowledge first has to come from experimental observations. Because of the difficulties and complexities involved in these

experimental observations, as will be detailed in Section II, only a limited number of experimental studies have been undertaken. A brief review of the available experimental observations will be summarized in Section II.

One of the goals of this study was to develop an effective experimental method to observe the mechanics of flowing suspensions. It was demonstrated that velocity distribution of the dispersed phase of flowing suspensions could be measured with a modified laser Doppler anemometer (LDA) while that of the suspending phase could be approximated by using small fluorescent tracers. The same experimental approaches can also be utilized to measure concentration distribution of the suspended particles though, due to the lack of the necessary recording equipments, no such measurements were made in this study. Due to our interest in transport processes in blood circulation as well as clinical applications to artificial kidneys and heart-lung machines, measurements were performed with suspensions of human red blood cells. A review of the presently available experimental results on blood flow will be included in Section II.

II. Review of Literature

Due to interests in application to physiological systems, the first detailed observations of two-phase fluids were probably made on the flow of blood. Vertebrate blood has often been viewed as a concentrated suspension of deformable, disclike particles which circulates in distensible vessels of sizes ranging from less than 1 to approximately 3000 red cell diameters. As early as the 17th Century, Malpighi (see Copley and Blair, 1968) reported the presence of a cell-free maginal layer when observing the flow of blood in peripheral vessels under a microscope. Poiseuille (1842), a French physician, performed his well-known experiments on the effects of pressure, temperature, length and size on the flow rate of water through a tube, with the thought of applying the results to blood circulation. Poiseuille (1835), when studying blood flow in a tube, also observed the presence of a cell-free layer near the tube wall, and found it to decrease in size as velocity increased. Leeuwenhoek and Hales (see Wayland and Johnson, 1967) first attempted to measure velocities of red cells. Krogh (1929) observed that the extent of the cell-free plasma layer was a function of flow rate and the size of corpuscles and vessels.

Copley et al. (1960, 1962, 1968) studied blood flow in the microvessels (19-114 μm in lumen) of the hamster's cheek pouch, and measured the extent of the peripheral plasma layer. The layer was reported to decrease as velocity was increased, but no data were given on the magnitude of the velocity and other flow parameters. By using high speed cinematography, Block (1962) studied the microcirculation in the mesentary, lung and skeletal muscles of frogs, mice, rats and rabbits, and concluded that

the ratio of peripheral layer thickness to vessel radius increased as the vessel radius decreased, and that wide variations occurred in flow and pressure, without a significant alteration in the size of the peripheral plasma layer.

Methods other than cinematography were also used for the study of flows of disperse systems. Estimates of erythrocyte velocities have been obtained by a flying spot system (Branemark and Jonsson, 1963) and by a rotating prism device (Munro, 1966). But these methods depend upon the judgment of the observer and do not lend themselves to frequent readings (Wayland and Johnson, 1967). Velocity profiles of erythrocytes were also measured by analyzing the frequency modulation of a light beam by the passage of erythrocyte images across a slit of photomultiplier tube (Wiederhielm, 1966). This method, however, suffers from poor temporal and spatial resolutions, and cannot differentiate flow directions. The use of photoelectric microscopy to study flow rate in the microcirculation was suggested by Asano et al. (1966). Wayland and Johnson (1967) attempted continuous velocity measurements of erythrocytes from the characteristic patterns generated by a red cell in two photometric outputs. But the spatial resolution of this photometry method was later found by the same investigators to be much worse than first expected, and the device can only be used to measure average velocities. Other investigators (Taylor and Robertson, 1954; Wiederhielm and Billig, 1968) attempted to measure the concentration and orientation of erythrocytes in microscopic vessels by photoelectric microscopy.

Application of these methods has remained in general of an exploratory nature. The quantitative information obtained from these in vivo observations

was limited by the lack of a controlled geometry, and the uncertainty as to the effect of the boundaries.

In order to overcome the uncertainties, the need to perform studies on better defined systems was realized. This need can be realized by in vitro or model investigations which are designed to study isolated aspects of the complex flow mechanisms occurring in living systems and other flows of disperse materials. Goldsmith et al. (1966, 1967, 1968, 1975) performed extensive experimental studies on model suspensions as well as on suspensions of red blood corpuscles. Of particular interest to this study are the results of measurements with cinematography of velocity distributions in various suspensions flowing in tubes with different radii. For tube flows of suspensions of rigid spherical particles it was found that sufficiently small particles (e.g. $a/R_0 \leq 0.028$ where R_0 is the tube radius) and volume fraction ϕ of suspended particles (e.g. $\phi \leq 0.14$) the particle and suspending velocity profiles were identical and parabolic. As ϕ or a/R_0 or both were increased, velocities of the two phases continued to be equal, but the velocity profiles were blunted in the center of the tube, resulting in a partial plug flow with a core of radius R_c. At a given a/R_0 the radius of the core increased with increasing ϕ and similarly for increasing a/R_0 at a constant ϕ, until an apparent plug flow was present across the whole tube. The relative velocity profiles were found to be independent of flow rate and viscosity of the suspension, provided the particle Reynolds number, $Re_p < 10^{-5}$, above which radial migration due to inertia effects became appreciable. The behavior of suspensions of rigid rods and discs showed a similar behavior. To overcome the problem of multiple reflection and refraction of the transmitted

light in suspensions of red blood cells, Karnis et al. (1966) studied the flow behavior of suspensions of ghost erythrocytes. The ghost erythrocytes were prepared from whole erythrocytes with the hemoglobin molecules removed, and the cells reconstituted to their original shape. The velocity distributions paralleled those found in model suspensions of rigid particles. At $\phi > 0.2$, the velocity profile of ghost cells in a tube with $R_0 < 50$ μm began to deviate from the parabolic profile for Newtonian fluids, but less so than in comparable suspensions of rigid discs. It was also found that the deviation from the parabolic profile in ghost cell suspensions was somewhat greater at low flow rates than at higher flow rates. More detailed summaries of these experimental results can be found in Goldsmith and Mason (1967), Goldsmith (1968), and Goldsmith and Skalak (1975),

Bugliarello and Sevilla (1970) observed the flow of human blood through hollow glass fibers of 40 to 70 μm in lumen with high speed microcinematography, both under steady and pulsating conditions. The data, however, showed substantial scatter and were thus inconclusive. Within experimental errrors, the velocity distributions in pulsatile flow were in phase with the pressure gradient.

Gaylor (1973) attempted to overcome the difficulties in tracking optically the red cell velocities by analyzing the residence time curves of radioactive labelled blood exiting from a semi-infinite parallel plate channel. For a plate separation gap of 239 μm and estimated wall shear rates of 117-226 sec^{-1}, red cells possessed a lower residence time, hence inferring a higher mean velocity than plasma within the duct. The assumptions required in the analysis of data, however, made interpretation

of data difficult.

Goldstein and Kried (1971) first attempted to use laser Doppler anemometry to measure velocity profile in suspensions of ghost erythrocytes flowing in a rectangular channel. Velocities of the ghost cells were obtained from the Doppler frequencies of the scattered laser light. Blunting of the velocity profile in the center of the flow channel at high concentrations of ghost cells ($\phi > 0.20$) was observed. Because of the relatively large measurement volume used, the spatial resolution was less than ideal and the results degraded.

Durst (1972) demonstrated that Doppler signals could be obtained from laser light scattered by red blood cells flowing in the venules of a mouse mesentary, but did not attempt spatially local measurements. Vlachos and Whitelaw (1974) demonstrated that the quality of the Doppler signal diminished with increasing hematocrit (concentration of red cells) and that with whole blood, with a hematocrit of approximately 0.45, Doppler signals were not measurable from capillaries of inside diameter greater than around 250 μm, because of multiple scattering and attenuation of the laser light.

The problem of attenuation and multiple scattering of the light source in the measurement of velocities in suspension flows is universal to all optical or flow visualization methods. Optical methods, however, are at the present the only methods suitable to the study of suspension flows. The conventional techniques, such as the Pitot tube and hot wire or hot film anemometry, usually perturb the flow and introduce significant errors due to the free convection and variations in viscosity. Even the most sophisticated hot-wire probe will produce, if ever possible, only

the very rough spatially averaged values of fluid velocity because of its large size relative to the size of the suspended particle. Its readings in regions close to the solid wall will, as is commonly known, be greatly disturbed due to the interference, both mechanical and thermal, of the wall. For concentrated suspensions, the interactions between the suspended particles and probe will be significant, and aggregation of particles on the probe is likely. Probes such as the hot wire or hot film also lack the ability to measure the flow properties of the two phases simultaneously.

Because of its non-invasive nature, most of the available experimental data were obtained by using optical methods. In the case of model suspensions, the problem of multiple scattering and attenuation can be partially solved by matching the refractive indices of the two phases. For suspensions of red blood cells, studies are limited to flows in microchannels and capillaries, or by using suspensions of ghost erythrocytes. Matching the refractive indices in the case of model suspensions or preparation of ghost cells does not produce perfectly transparent suspensions and therefore the limitation on the size of the macroscopic system is only relieved and not eliminated.

The very popular method of microcinematography, which requires examination of the film frame by frame, is a most laborious procedure. Often there is an upper limit on the measurable velocities imposed by the need to translate the entire optical setup in order to track the velocities of the particles. The use of laser Doppler anemometry has provided an improvement in spatial and temporal resolution, as well as greatly reducing

the labor involved in data processing. Laser Doppler anemometry, however, has only previously been applied to the measurement of velocities of the dispersed phase of suspensions, and not directly to simultaneous measurement of the velocities of both phases.

III. Objectives of This Study

This study was aimed at understanding the characteristics of flowing suspensions. In particular, it was our interest to study the behavior of moderately concentrated suspensions so that the results would be applicable to blood flow in physiological conditions. In order to perform the study, it was necessary to develop an appropriate experimental method. The first objective of this study was therefore the development of an experimental method of simultaneously measuring the velocities of both phases that would eliminate the problems encountered in methods used by previous investigators. Of foremost concern, was the fact that the method had to have good temporal and spatial resolution. The technique described here has all of these characteristics. In addition, it is possible, in principle, to adapt the method for measurement of concentration distributions of the suspended particles. After the development of the experimental method, it was our objective to study flows of both model suspensions and suspensions of human erythrocytes. The effects of the concentration of the suspended particles, the relative size of the suspended particles to the size of the flow channel, and the flow rates used were to be investigated.

IV. Experimental Approach

In the study of suspension flows, one major reason for the lack of experimental data is the difficulty in making measurements of velocity fields. As discussed in Section II, the most useful methods for the observation of velocity distributions in flowing suspension are optical methods. In this study, measurement of velocity distributions of the dispersed phase of flowing suspensions was attempted by utilizing laser Doppler anemometry. The suspended particles in suspensions are ideal for the scattering of the laser light. The Doppler frequency of the laser light scattered from the suspended particles is proportional to the velocity of the particle. The velocity distribution of the suspended particles can therefore be found directly by measuring the frequency of this Doppler signal. As will be seen later, the regular optical arrangements of laser Doppler anemometry do not provide the optimal spatial resolution. Modifications of the optical arrangements were made in this study to improve the spatial resolution of the measurement. The standard LDA measurement, however, does not give the velocity distribution of the suspending fluid. A complementary method which allowed the velocity distribution of the suspending phase to be approximated was developed for this study. This method allowed the use of an experimental setup virtually identical to that used in laser Doppler anemometry. A description of this method, together with a description of the modifications performed to the regular laser Doppler anemometer is presented in this section. As an introduction to the discussion of the modifications, the principle of operation of laser Doppler anemometry is also presented.

Of equal importance in the study of suspension flows is the problem of choosing the proper suspensions for experimental observation. Ideally, the suspensions used should be well defined so that the dependence of flow behavior on variables such as size distribution and concentration of the dispersed phase, the rheological properties of the suspending fluid, the difference in density of the two phases, etc., can be studied. For application to the flow of blood in physiological or clinical systems, on the other hand, a suspension of red blood cells or a close analog of such a suspension is necessary. In order to use any optical methods, the suspension has to allow the transmission of the source light. Therefore, within the flow channel, the suspension has to be transparent at the frequencies of the light source used. The usual approach is to render the suspension transparent by matching the refractive indices of the two phases of the suspension.

In this study, only neutrally buoyant suspensions or nearly neutral buoyant suspensions were used. The use of neutrally buoyant particles was intended to simplify the interpretation of rheological measurements by eliminating the effect of gravity. The requirement of simultaneously matching the refractive indices and the densities of the dispersed and suspending phases imposes a serious constraint on the choice of material and was a formidable problem in this study.

Three different kinds of suspensions were actually used: (i) model suspensions of near monodisperse rigid spherical latex particles suspended in a Newtonian fluid, (ii) suspensions of whole red blood cells in isotonic buffer, and (iii) suspensions of ghost red blood cells in isotonic buffer. The model suspensions provided well-defined systems in terms of

the physical properties such as shape, rigidity and size distribution of the particles. Suspensions of whole red blood cells and ghost cells, on the other hand, provided good analogs to whole blood. For adequate transmission of light, ghost cell suspensions were also necessary in the higher concentration range. A more detailed description of the suspensions is presented in this section.

1) Experimental Method

A description of the experimental method employed in this study is presented here. The primary experimental tool was a laser Doppler anemometer (LDA). The use of LDA for measurements of velocity is now an established method (Durst et al., 1976; Durani and Greated, 1977). In order to improve the spatial resolution, however, the optical arrangement of LDA used in this study was different from the regularly encountered arrangements. It is, therefore, useful to first present a discussion of the normal arrangements of LDA before discussing the modifications performed.

a) Laser Doppler Anemometry

Introduction

The Doppler effect has been widely exploited as a powerful tool for sensing relative motion. In the visible range of the electromagnetic spectrum, this effect has been used on a cosmic scale to measure the velocity of distant astronomical bodies, and on a microscopic scale to obtain information about the thermal motion of atoms and molecules in gases. On a macroscopic scale, however, use of the Doppler effect to measure relative motion has been somewhat impractical due to the limited

resolution obtainable by spectrographic techniques. Spectroscopic measurement of a wavelength shift $\Delta\lambda$ in the visible spectrum with an accuracy of a few percent, for example, requires a relative wavelength shift $\Delta\lambda/\lambda$ at least as large as 10^{-4}, which corresponds to a relative velocity of roughly 10^5 feet per second between source and observer. On the other hand, microwave Doppler radar systems can readily resolve wavelength shifts on the order of 10^{-7}. The essential difference between the situations is the fact that a radar transmitter serves as a source of coherent electromagnetic radiation, and hence, detection of the Doppler shift can be accomplished by coherent mixing techniques.

With the advent of the gas laser, a source of continuous coherent electromagnetic radiation at optical wavelengths became available and the technique of coherent mixing at optical wavelengths, now commonly referred to as optical heterodyning, was developed into a practical laboratory tool. These two developments brought the concept of optical Doppler radar into the realm of feasibility. Doppler heterodyning experiments involving lasers have now become commonplace. Application of the optical Doppler radar principle to fluid flow measurements requires the use of optical heterodyning to sense the Doppler shift in laser light which is scattered from small tracer particles in the fluid. In general, the size, shape, and volume distribution of these particles cannot be closely controlled. Thus, it might be expected that the coherence of a laser light scattered from an irregular array of particles would be poor, therefore precluding optical heterodyning. But, Cummins, Knable, and Yeh (1964) demonstrated that heterodyning of laser light scattered from suspensions of

polystyrene spheres was feasible. Yeh and Cummins (1964) then constructed a laser flowmeter for measurement of localized liquid flow velocities. Foreman, George, and Lewis (1965) developed a laser Doppler anemometer (LDA) for measurement of localized flow velocities in gas using smoke as scattering particles, thus verifying the feasibility of Doppler heterodyning with laser light scattered from particles of irregular size and shape. Since then, progress has been made rapidly on many aspects of the subject. Among these are the analysis and design of new and improved optical geometries, the development of pre-aligned optical systems readily adaptable to different flow situations, the development of systems with direction-sensing capabilities, design of signal-processing equipment specifically suited to handle laser Doppler signals, in-depth studies of scattering of tracer particles, and the use of LDA to measure flows inaccessible to other instruments.

The use of LDA for fluid flow measurements has many advantages over various conventional methods. The Doppler shift is a linear and direct response to velocity, therefore eliminating the need for any calibrations. It has good spatial resolution and a virtually instantaneous response to velocity. This method is essentially non-invasive in nature, making it ideal for study of suspensions.

Many optical arrangements of LDA are currently available. The different arrangements are very similar in nature as they are all designed from the same principle. The system used in this study was a modified version of a commercial system utilizing two beams and real fringes. Before the modifications are described here, the unmodified two beam, real fringe system is first discussed.

Two Beam, Real Fringe LDA

A two beam, real fringe LDA system, first proposed by Rudd (1969), is shown schematically in Figure 3. Rudd pointed out that two parallel beams focused in the flow with a simple lens would in fact produce Young's interference fringes (Fig. 1). The laser beam is split into two and re-focused to form the interference pattern in the flow region. After emerging from the other side of the lens, the two beams are masked off and only the scattered light from particles present at the fringe pattern is allowed to fall on the surface of a photodetector.

Before considering the scattering by particles in a two-beam system, the Doppler shift of scattered light from one laser beam by one particle is first considered (Fig. 2).

The electric field of the laser beam propagating in a homogeneous medium is given by the real part of the vector $\vec{E}$,

$$\vec{E} = \vec{E}_o e^{i(\vec{k}_1 \cdot \vec{x} - \omega t)} \tag{1}$$

where $\vec{k}_1$ is the propagation vector ($|k_1| = 2\pi/\lambda$), λ is the wavelength and ω is the angular frequency of the laser. If the beam strikes a particle moving with constant velocity at $\vec{x}$, where

$$\vec{x} = \vec{x}_o + \vec{v}t \ ,$$

the electric field at the particle is

$$\vec{E}_{particle} = \vec{E}_o e^{i\left[\vec{k}_1 \cdot \vec{x}_o - (\omega - \vec{k}_1 \cdot \vec{v})t\right]} \tag{2}$$

The frequency of the wave registered on the particle is therefore

$$\omega_{particle} = \omega - \vec{k}_1 \cdot \vec{v} \tag{3}$$

So relative to a coordinate frame on the particle, the light scattered by the particle will be radiated with this frequency. If $\vec{k}_{sc}$ is the propagation vector of the scattered light, the scattered field is given by

$$\vec{E}_{sc} = \vec{E}_{o_{sc}} e^{i(\vec{k}_{sc} \cdot \vec{x}_1 - \omega_{particle} t)} \tag{4}$$

with the intensity of the scattered light given by $|E_{o_{sc}}|^2$ and $\vec{x}_1$ is the position of observation measured in coordinates on the particle. In a fixed coordinated frame this observation position is

$$\vec{r} = \vec{x} + \vec{x}_1 = \vec{x}_o + \vec{x}_1 + \vec{v}t$$

Substituting the above expression into Eq. (4) results in

$$\vec{E}_{sc} = \vec{E}_{o_{sc}} e^{i\left[\vec{k}_{sc} \cdot (\vec{r} - \vec{x}_o) - \left[\omega + (\vec{k}_{sc} - \vec{k}_1) \cdot \vec{v}\right] t\right]} \tag{5}$$

It is obvious that the Doppler shift frequency observed is given by

$$\omega_o = (\vec{k}_{sc} - \vec{k}_1) \cdot \vec{v} \tag{6}$$

Now for the dual scatter system (Fig. 3), the electric fields are given by

$$\vec{E}_j = \vec{E}_{o_j} e^{i(\vec{k}_j \cdot \vec{x} - \omega t)} \qquad j=1,2 \text{ for the two beams} \tag{7}$$

The scattered radiation from the two incident beams are:

$$\vec{E}_{sc_j} = \vec{E}_{o_{sc_j}} e^{i\left[\vec{k}_{sc} \cdot \vec{x}_o - (\omega + (\vec{k}_{sc} - \vec{k}_j) \cdot \vec{v}) t\right]} \tag{8}$$

At the surface of the photodetector these two electric fields give a resultant intensity of

$$I = E_{o_{sc_1}}^2 + E_{o_{sc_2}}^2 + 2 E_{o_{sc_1}} E_{o_{sc_2}} \{\cos(\vec{k}_2 - \vec{k}_1)\cdot\vec{v}t\} \quad (9)$$

As the two incident beams have the same wavelength, the Doppler shift frequency F_o is thus

$$F_o = \frac{2V_x}{\lambda} \sin\frac{\theta}{2} \quad (10)$$

This frequency is independent of the direction of the scattered ray. An optical detector with a large solid angle can therefore be constructed to improve the signal strength.

The same result can be obtained by considering the interference fringe pattern formed at the intersection of the two equal intensity beams (Fig. 4):

The wavelength of the fringes is

$$S = \frac{\lambda}{2 \sin\frac{\theta}{2}} \quad (11)$$

For a particle passing through the pattern with a velocity normal to the fringe of V_x, the frequency of the scattered light is

$$F = \frac{V_x}{S} = \frac{2V_x}{\lambda} \sin\frac{\theta}{2}$$

which is identical to the Doppler frequency calculated above.

Frequency Shifting

Since frequency shifting was incorporated in the LDV system used in

this study, a brief description of the method is presented here.

In many flow situations the velocities are continuously reversing in direction between positive and negative values. The LDA system described above would not be able to resolve this sign ambiguity. Difficulties in processing the Doppler frequency could also arise when the velocities exhibit large fluctuations. The design of most electronic frequency processors also prohibits the measurement of low frequencies arising from near-zero velocities. By shifting the frequency of one or both of the laser beams, either electro-optically or acousto-optically, these difficulties can be resolved down to the spectral width of the shifted frequencies. In the discussion here, attention is devoted to the acousto-optic cells, called Bragg cells, used in this study.

Bragg cells are either in the form of a block of solid transparent material or a small cell filled with liquid, the principle of operation being the same in either case. Along one side of the cell is a piezoelectric transducer coupled to a high frequency electrical supply. This produces a train of plane acoustic waves which move across the cell at the speed of sound and are absorbed at the far end by some damping material. Since the sound waves cause variations in the refractive index of the medium, the effect is that of a three-dimensional moving diffraction grating. At a certain angle of incidence, the Bragg angle, nearly all of the incident light is diffracted into the first order and the beam emerges being frequency shifted by an amount equal to the frequency of the sound wave. Typical efficiency of Bragg cells is approximately 70%. A detailed review of the properties of Bragg cells, as well as other electro-optic cells, can be found in the literature (Gorden, 1966; Chenoweth et al., 1966; Kaminov and Turner, 1966).

Frequency Counter

An analysis of the operating principles of frequency counters used in the experiment for processing the Doppler signal is not presented here as they are quite well known. Detailed reviews of the operating principles of counter-processors, together with descriptions of other laser Doppler systems and analyses of accuracy of the laser Doppler methods, can be found in the literature (Durst et al., 1976; Durrani and Greated, 1977).

Modified LDA System

With LDA, spatial resolution of the measurements usually is not a problem in most flow situations with length scales of the order of centimeters. When the observation volume is formed by focusing two laser beams into the flow region, the size of the measurement region is determined by the diffraction-limited spot size of the focused beams (Fig. 5). The size of the measurement volume decreases with decreasing focal length of the focusing lens and increasing separation of the two parallel beams. Typically, the measurement volume is $\lesssim$ 1 mm in length and $\sim$ 0.1 mm or more in width. Problems arise when the characteristic dimensions of the flow, such as fluid flows in thin channels and capillaries, become comparable to the dimensions of the measurement volume. Attempts have been made by various researchers to reduce the measurement volume. Vlachos and Whitelaw (1974), for example, used an intersecting angle of 90^{o} between the two laser beams to reduce the length of the measurement volume to 60 μm with a He-Ne laser. This arrangement, however, is limiting to the geometry of the flow channels. Born, Vlachos and Whitelaw (1975) used an argon laser instead of a He-Ne laser to reduce this length to around

20 μm in water and air, as a consequence of the larger beam diameter and shorter wavelength. Optical transmission and collection were achieved by using a microscopic lens aperture. A similar approach was used by Mishima, Asakura and Nagai (1974), who called their instrument a laser Doppler microscope. In essence, an ordinary microscope with white light illumination is combined with a real fringe LDA operating in backscatter, which allows the operator to visually align the probing position. It remains to be determined if the aberration resulting from transmitting light through the edges of a single focusing lens, as available in a microscope, can be reduced sufficiently to allow spatially local measurements in flow channels.

In this study, a rectangular flow channel of approximately 0.8 mm in width was used. The shortest measurement volume achievable at the maximum beam separation and with the focusing lens of shortest focal length available to the LDA before modifications was approximately 0.6 mm. In order to obtain useful spatial resolutions, modifications on the focusing and/or receiving optics had to be implemented. Conceivably, the size of the measurement volume could be reduced by enlarging the diameters of the laser beams as well as reducing the focal length of the lens, which is used to focus the two beams to form the interference pattern. Since the size of the diffraction limited spot is proportional to the focal length of the lens which is used to focus the two beams to form the interference pattern and inversely proportional to the original beam diameter (Fig. 5), a smaller measurement volume could conceivably be produced by altering these two quantities. The disadvantages of this approach are in the limitation imposed on the geometry of the flow channel due to the closeness of the lens and its

focus as a result of the short focal length, and, more important, in the substantial distortion to the wavefronts of the laser light due to the drastic reduction in the size of beam diameters. This distortion would result in spherical aberration and the fringe spacings within the interference pattern would vary, resulting in broadening of the Doppler frequency. It was decided to rearrange, instead, the receiving optics of the LDA. A description of the modifications and an approximate analysis of the requirements of this method and presented here. Description of hardware as well as the dimensions of interest will be presented later in the section on experimental procedures.

Figure 6 shows a schematic representation of the modified LDA. The idea of this arrangement is: instead of using a sufficiently small measurement volume to locate the point of measurement, a measurement volume larger than the width of the flow channel is used. The measurement volume is then aligned across the whole channel. A sufficiently narrow slit is placed in front of the photodetector which is positioned at the magnified image of the measurement volume formed by appropriate light collecting optics. By scanning the slit across the magnified image, the location of the point of measurement within the flow channel can be determined.

In order to determine the point of measurement with the narrow slit, the receiving optics has to be approximately perpendicular to the plane formed by the two laser beams and AB (Fig. 6), instead of positioning the receiving optics in front of AB and in the plane of the laser beams, as in the case of forward scattering. This arrangement could possibly create difficulty in the detection of scattered light when both the power of the laser is low and the size of the scatterers is small. This problem was

not encountered in this study due to the relatively powerful argon laser and the sufficiently large particles used. Geometric optics can be used to determine the relation between the position of any point within the measurement volume to that of the image as follows (Fig. 7).

The photodetector is assumed to be at the same vertical level as the measurement volume AB. Consider now the points A_1B_1 within the measurement volume and at a distance h, apart, with B_1 lies on the principal axis of the receiving optics. For B_1 and its image B_1'

$$M = \frac{l_2}{l_1} = \frac{f}{l_1 - f}$$

where M is the linear magnification.

Equivalently,

$$l_2 = \frac{l_1 f}{l_1 - f}$$

Similarly for A_1 and A_1',

$$l_3 = \frac{(l_1 + h_1 \sin\theta) f}{l_1 + h_1 \sin\theta - f}$$

Now, $h_2 \sin\phi = l_2 - l_3$

$$= \frac{h_1 M f \sin\theta}{l_1 - f + h_1 \sin\theta} \qquad (12)$$

If $l_1 - f >> h_1 \sin\theta$, this expression becomes

$$h_2 \sin\phi \approx \frac{h_1 M f \sin\theta}{l_1 - f} \qquad (13)$$

For fixed M, f and θ, h_2 can therefore be expressed as

$$h_2 \propto \frac{h_1}{\sin\theta} \qquad (14)$$

By using similar triangles,

$$\frac{l_1 + h_1 \sin\theta}{l_3} = \frac{h_1 \cos\theta}{h_2 \cos\phi}$$

so,

$$h_2 \cos\phi = \frac{fh \cos\theta}{l_1 - f + h \sin\theta} \tag{15}$$

Substituting Eq. (12) into the above expression yields:

$$\cot\phi = \frac{f}{M} \cot\theta \tag{16}$$

i.e., ϕ is constant for fixed f, M and θ, and is independent of h.

Equation (16) can therefore be written as

$$h_2 \propto h_1 \tag{17}$$

As long as $h_1 \sin\theta \ll l_1 - f$, which, as will be shown, was the case in this study, any point within the image is linearly proportional in distance to its corresponding point within the measurement volume. The velocity profile of the flow within the flow channel can be measured by simply moving the narrow slit across the image and its position can be used to determine the position of the point being measured within the flow channel.

In the description of the method given above, the image of the measurement volume was assumed to be perfectly sharp so that the slit could be placed exactly at the plane of the image. This assumption, however, cannot be achieved in reality. An uncertainty in the focus of the image is always present, and degrades the spatial resolution of the method. The width of the slit has to be chosen properly to ensure the degree of accuracy desired. This width can be determined by examining the effect of

displacing the slit by a distance x in front of or behind the actual position of the image (Fig. 8).

The diameter D and focal length f of the focusing lens are assumed to be fixed. By choosing a given magnification M and a slit width d, the corresponding linear dimension of the 'point' of detection with the measurement volume can be determined for a given x as follows:

The magnification M is given by

$$M = \frac{f}{s_1 - f} = \frac{s_2}{s_1}$$

Referring to Fig. 8, the length h is

$$h = h_2 - h_1$$

The corresponding length of the image, Δ, passing through the slit is given by

$$\Delta = \frac{s_2}{s_1} h$$

The angles θ_1 and θ_2 can be determined from the following expressions:

$$\sin\theta_1 = \left(\frac{s_2}{s_1} h_1 - \frac{D}{2}\right) / s_2$$

$$\sin\theta_2 = \left(\frac{s_2}{s_1} h_1 + \frac{D}{2}\right) / s_2$$

Now the slit width d is given by

$$d = \Delta + x(\sin\theta_1 - \sin\theta_2)$$

$$= Mh - \frac{(Mh + D)x}{(M + f)} \qquad (18)$$

By rearranging the above expression, h is given by

$$h = \frac{df(1 + M) + xD}{M[f(1 + M - x]} \qquad (19)$$

x, the ambiguity in focusing, depends on the quality of the lens used. Its value can be determined by observing an image of a point source formed by the lens and measuring the distance over which the sharpness of the image remains apparently constant. The length h can then be obtained for a given combination of d, f, D and M. Conversely, the width of the slit, d, can be determined for any desired h, a function of the length of the entire measurement volume and the number of independent data points desired.

Since the measurement volume has a finite width (usually much smaller than the length), it has an effect on the actual length of detection h of each data point within the measurement volume. This calculation, however, is very simple and will not be presented here.

Measurement of Velocity with Fluorescent Tracers

As mentioned above, LDA measures the velocity of the particles present in any fluid flows, instead of the velocities of the fluid directly. If the concentration of the particles is low and the particle size sufficiently small, the fluid flow is not greatly disturbed by the presence of the particles. The velocity of the particles in this case is usually assumed to be the same as that of the fluid. This is not necessarily always the case. The velocity of the particles might deviate in the direction and magnitude from the fluid velocity. For example, Segré and Silberberg (1962) observed that a single, rigid, neutrally buoyant spherical particle suspended in a Poiseuille flow migrates across the

streamlines until attaining a stable position at about 0.6 tube radius away from the axis. By proper choice of particles, however, the difference between the velocity of the particles and the fluid can be very small, and one might obtain very reasonable experimental results. Information on this subject can be found in the literature (Cox and Mason, 1971; Somerscales, 1971; Merzhirsch, 1974).

For flows of suspensions at moderate to high concentrations and when the particle size is comparable to the dimensions of the channel, the velocity measured with LDA gives directly the velocity of the particles, which might be very different from the velocity of the fluid. In order to measure the fluid velocity more accurately, it is necessary to use tracer particles which are much smaller than the spacing between suspended particles to follow the flow more closely. The signal from these particles must be sufficiently different from that of the particles in the suspensions so they can be differentiated. Lee and Einav (1972) successfully used the dependence of the amplitude of the scattered light on particle size to measure the velocities of two distinct distributions of suspended particles in a laminar boundary layer. Due to the usually high attenuation of the scattered light in concentrated suspensions, this method can only be used for dilute suspensions. Another possibility is the use of fluorescent particles as tracers. In our laboratory the feasibility of this approach was demonstrated by using solid fluorescent particles. Stevenson et al. (1975) used the same idea and published the first experimental observation on the use of liquid fluorescent particles to measure fluid velocity, but no analysis of the method was given. Durst (1975) claimed to have made the same observation, again using liquid fluorescent particles. In the

following a quantitative description of the method is presented. Since tracer particles must be very small in size, it is conceivable for many tracers to be present within the measurement volume simultaneously. The effect of multiple particles within the measurement volume is also analyzed and the results presented in Appendix I.

When two laser beams of frequency $\frac{\omega_o}{2\pi}$ and equal intensity cross, the beams would set up a bright and dark interference pattern (Fig. 4). Ignoring the Gaussian distribution of the laser beam intensity, the intensity of the fringe pattern, A, can be represented by a cosine function:

$$A = A_o \left(\frac{\cos\pi x}{d} + 1\right) \tag{20}$$

where $d = \frac{c}{\omega_o}\frac{1}{2\sin\theta} = \frac{\lambda}{2\sin\theta}$ = fringe separation (21)

c = velocity of light

λ = wavelength of laser.

$$\text{So,} \quad A = A_o \left[\cos\left(\frac{2\pi x}{\lambda}\sin\theta\right) + 1\right] \tag{22}$$

The electric field pattern at the crossing of the two beams can therefore be written as

$$E = A_o \left[\cos\left(\frac{2\pi x}{\lambda}\sin\theta\right) + 1\right] e^{i2\pi\omega_o t} \tag{23}$$

For a fluorescent particle of size much smaller than the fringe spacing, the absorption and subsequent fluorescence are proportional to EE^*, E^* being the complex conjugate of E. For a particle traveling at velocity V_x in the x-direction, its emission field E_f is given by

$$E_f \sim e^{i\phi(t,t_n)} \left[(EE^*)\delta(x - vt)\right]^{\frac{1}{2}} \tag{24}$$

where δ = Dirac delta function.

Here, t_n is the time at which the particle enters the fringe pattern. The phase of the fluorescence is denoted by $\phi(t,t_n)$, which accounts for the very broad frequency spectrum involved as well as the noncoherent emission.

The anode current i, generated at the photodetector, is proportional to $E_f E_f^*$:

$$i \alpha EE_f^* \alpha A_o \cos^2\left(\frac{2\pi x}{\lambda} \sin\theta\right) \delta(x - vt) \tag{25}$$

By summing over the illuminated x, the total current for a single particle, the detected current, started at time zero, is given by:

$$i \alpha A_o^2 \cos^2\left(\frac{2\pi}{\lambda} V_x t \sin\theta\right) \text{rect}\left(\frac{V_x t}{D}\right)$$

$$\alpha \frac{A_o^2}{2}\left[1 + \cos\left(\frac{4\pi}{\lambda} V_x t \sin\theta\right)\right] \text{rect}\left(\frac{V_x t}{D}\right) \tag{26}$$

The anode current thus contain the same velocity information as with regular laser Doppler anemometry. The method makes use of intensity measurements instead of optical heterodyning as in LDA. The intensity of the fluorescent signal depends on the intensity of the laser light, the concentration of particles and the quantum yield of the fluorescent dye. Except for the need for optical filtering, as discussed below, the method utilizes virtually the same experimental setup as LDA.

Description of Experiment

Flow Channel

All the experiments were performed with a vertically mounted thin rectangular channel (Fig. 9). The channel was constructed of lucite with dimensions of 28 cm x 2 cm x 0.0794 cm. The dimensions were chosen such that the flow in the channel, as will be shown, approached that between semi-infinite parallel plates while the width of the channel is small enough for good optical transmission but much larger than the size of any particles in the suspensions. The lucite was 1.59 mm in thickness. The channel was mounted vertically and the circular inlet and outlet were located at the bottom and top of the channel, respectively, each having an internal diameter of 15.9 mm. In the middle of the channel, circular glass windows of 12 mm in diameter were mounted flush with the two inner walls of the channel. Each glass window was 0.141 mm thick. The glass windows were used instead of lucite for improved transmission of the laser beams and detection of the Doppler signals. The use of a rectangular channel eliminated the curvature effects encountered in tube flows. Measurement of blood flow in the channel also has direct application to artificial kidney dialysers.

For a laminar flow of a Newtonian fluid in a rectangular channel, the fully developed velocity field is given by Han (1960):

$$\frac{u}{\bar{u}} = \left(\frac{\pi}{4}\right)^2 \left\{ \sum_{m,n=1,3,5\ldots}^{\infty} \frac{(-1)^{\frac{m+n}{2}-1} \cos(m\pi x/2a)\cos(n\pi y/2b)}{mn(m^2 + n^2\gamma^2)} \right\} \Bigg/ \left\{ \sum_{m,n,=1,3,5\ldots}^{\infty} \frac{1}{m^2n^2(m^2 + n^2)\gamma^2)} \right\} \tag{27}$$

where the x,y coordinate directions are parallel to the sides of the cross-section of the channel and the origin of the coordinates at the center of channel,

u = velocity field at point (x,y)

$2a,2b$ = cross-sectional dimensions of the channel

and $\gamma = \frac{b}{a}$ = aspect ratio of the channel

For the flow channel used,

$$\frac{u_{max}}{\bar{u}} = 1.539 \qquad (28)$$

where u_{max} = velocity at the center of the flow channel and $\bar{u}$ = average velocity.

For a Newtonian fluid flowing between two semi-infinite parallel plates, the ratio $u_{max}/\bar{u}$ is 1.50. The flow field away from the corners of the flow channel used in this study therefore resembled closely that between semi-infinite parallel plates.

Suspensions

Three types of suspensions were used in the experiments: model suspensions of rigid particles, suspensions of whole red blood cells, and suspensions of ghost erythrocytes.

Model Suspensions

Rigid spherical particles of polystyrene copolymers were used in the model suspensions. The particles, manufactured by Diamond Shamrock Chemical Co., had a narrow distribution in size (Fig. 10). The mean

diameter was 34.6 μm and the standard deviation in diameter was 2.8 μm. The particles had a density of 1.05 gm cm^{-3}. In order to be used with optical methods, the suspensions have to be nearly transparent. A close match in refractive index and density was found by using as suspending fluid a mixture of approximately 13% by volume n-hexanol and 87% by volume cinnamaldehyde, resulting in a refractive index of 1.5938 at 20°C. The n-hexanol was obtained from Baker Chemical and the cinnamaldehyde from Aldrich Company. The density of the mixture was determined to be 1.03 gm cm^{-3}. In preparation of the suspensions, carefully weighed amounts of particles were suspended in a 12.5:83.5 (V/V) mixture of n-hexanol/cinnamaldehyde. The suspensions were then sealed and refrigerated and allowed to equilibrate for 1 - 2 days. Before each experiment, the suspensions were brought up to room temperature (20°C). Drops of n-hexanol and/or cinnamaldehyde were added to obtain the best match in refractive indices possible. Since there were minor variations in the refractive index of the polystyrene spheres, a perfect match of the refractive indices was impossible. Instead, the match was made by minimizing absorption of the laser beam at 488.0 nm through a sample of 1 mm in thickness. The spheres swelled by approximately 6% in diameter after suspended in the mixture for about one day, and no further increase in size could be detected with time. Photomicrographs of the particles indicated that the swelling had no apparent effect on the shape or rigidity of the particles. The volume fraction of the particles in the suspensions were determined from the weight of the particles and the actual amount of suspending fluid used. For the experiments, the volume fraction of the dispersed phase was varied from approximately 0.1 to 0.20.

The mixture of n-hexanol and cinnamaldehyde was found to be Newtonian. At 20°C, the viscosity of the mixture was determined to be 4.79 cp. The viscosity of the suspensions as a function of volume fraction of the dispersed phase was measured in a Couette flow type viscometer and the results presented in Figure 11.

Suspensions of Whole Red Blood Cells

The suspensions were prepared from outdated packed red blood cells obtained from the American Red Cross. The red cells were approximately five weeks old when they were used in the experiments. The red blood cells were biconcave discoid in shape and had an average major diameter of approximately 8 μm and a thickness of 2 μm. The packed cells contained approximately 12% by volume of the anticoagulant citrate phosphate dextrose. They were washed by resuspending in an isotonic Dodge buffer (2.842 gm l^{-1} of sodium phosphate monobasic and 12.47 gm l^{-1} of sodium phosphate dibasic in water, pH adjusted to 7.4), centrifuged at 1100 g for 25 min. The supernatant and the buffy coat of white cell layers were removed by aspiration. This washing process was repeated three times for each sample of blood. The washed red blood cells were stored at 4°C before use. For each experiment, appropriate dilutions with the isotonic buffer were made for the desired volume concentration (hematocrit) of red cells and the resulting suspensions brought up to room temperature (20°C). Hematocrit was determined by using the Wintrobe method (Wintrobe, 1967) at the end of each experiment. Due to problems in optical transmission, the hematocrits used ranged from approximately 1 to 8 only. The density of the red blood cells was approximately 1.09 gm cm^{-3}, while the density of the isotonic

buffer was 1.02 gm cm^{-3}. In order to inhibit bacterial growth, all containers and pipets used for washing and storage of blood were rinsed with dilute formaldehyde solution and then rinsed thoroughly with isotonic buffer. The viscosity of the isotonic buffer at $20^{o}C$ was measured to be 1.04 cp. Viscosities of the red blood cell suspensions at various concentrations were also measured and the results presented in Figure 10.

Ghost Suspensions

The objective in the preparation of ghost cells from the erythrocytes was to remove the homoglobin molecules from the erythrocytes, thereby rendering the erythrocytes virtually transparent. This was achieved by hemolysis in hypotonic solutions. The ghost cells were prepared from outdated packed red cells obtained from the American Red Cross. Before each preparation, the red cells were examined visually with a phase contrast microscope to make sure they were mostly biconcave in shape. The procedure used in the preparation of ghost cells was similar to that of Dodge, Mitchell and Hanahan (1963), generally referred to as the Dodge method. The following is a summary of the procedure:

Dodge Method

Solutions Required: 310 im Osm Dodge Buffer (DB)-isotonic at pH = 7.4. 2.742 g/l $NaH_2PO_4 \cdot H_2O$; 12.747 g/l Na_2HPO_4 + traces of Mg^{++} and ATP ; 20 im Osm Dodge Buffer at pH = 7.4.

Procedure: (i) Washing of red blood cells: To 150 ml of packed red cells add approximately 100 ml of 310 DB.

Perform 4 washes as follows:

(a) Centrifuge suspension at 1085 g for 20 min. Remove supernatant and white cell layer (buffy coat) by aspiration.

(b) Resuspend red cell pellets in ∿150 ml 310 DB. Centrifuge suspension with clinical centrifuge at IEC clinical setting 5 for 25 minutes, or with Sorvall ultracentrifuge at 2000 g for 5 minutes. Again remove supernatant and buffy coat.

(c) Repeat (b) two times.

(ii) Hemolysis: Add 28 ml of 20 DB to 2 ml red blood cell suspension in 310 DB. With Sorvall ultra-centrifuge, centrifuge at 13 K (20,000 g) for 20 minutes. Remove supernatant.

(iii) Washing Membrane: Resuspend membrane in ∿180 ml of 20 DB. Wash at 20,000 for 5 - 10 minutes. Remove supernatant. Repeat procedure until desired color of ghost cells obtained.

(iv) Storage: Resuspend pellet from final wash in 310 DB and store at $4^{o}C$.

In order to avoid extensive damage to the membrane of the cells and for the preparation of osmotically active ghost cells, the number of washes after lyzing the cells was limited to four or less. The ghost cells produced, as a result, were slightly pinkish in color and not totally transparent.

To inhibit bacterial growth, all glassware used in the preparation of ghost cells was rinsed with dilute formaldehyde solution and then rinsed with isotonic buffer.

The volume concentration of the ghost cells was determined by Wintrobe's method (1967), with correction for the buffer trapped between the ghost cells. The correction factor used was 0.90, as suggested by Goldsmith (1975). Proper dilutions were then made to obtain the desired volume concentrations, ϕ, of ghost cells. In the present experiments, ϕ was varied from 1% to 33%.

Fluorescent Tracers

The fluorescent tracers were supplied by Dr. A. Rembaum of the Jet Propulsion Laboratory. They were monodisperse hydroxyl-ethyl-methacrylate (HEMA) particles of 0.8 μm in diameter. The fluorescent dye fluorescein isothiocyanate was chemically attached to render the particles fluorescent when excited. The density of the particles was approximately 1.0 gm cm^{-3}. For the concentration of the various suspensions and the sizes of the suspended particles used, these tracer particles were at least 50 times smaller than the average separation of the suspended particles.

Circulation of the Suspensions

The suspensions were circulated through the flow channel by using a syringe pump. When used with a 50 cm^3 syringe, the pump supplied flows at 8 fixed flow rates, ranging from 2.3×10^{-3} cm^3 sec^{-1} to 0.55 cm^3 sec^{-1}. Since the slow flow rates gave flows too slow to be

measured by the experimental system, only the 5 higher flow rates were used. They were: 2.48×10^{-2} cm^3 sec^{-1}, 4.93×10^{-2} cm^3 sec^{-1}, 1.06×10^{-1} $cm^3 sec^{-1}$, 2.71×10^{-1} cm^3 sec^{-1} and 0.55 cm^3 sec^{-1}. By defining the Reynolds number of the flow as

$$Re = \frac{De\ \bar{u}}{\nu}$$

where the hydraulic diameter $De = \frac{4ab}{a + b} = 0.191$ cm., Re varied from 2.33 to 51.9 for the mixture of n-hexanol/cinnamaldehyde, and from 0.512 to 11.4 for the Dodge isotonic buffer. For the suspensions, Re varied with the volume fraction of the particles. For a Newtonian fluid, the wall shear rate at the center of the flow channel varied from 5.61 sec^{-1} to 134.26 sec^{-1} for the corresponding flow rates used.

LDA

The laser Doppler anemometer used in the experiments consisted basically of a model 165 argon laser from Spectra Physics Inc., and a Type 55 L laser Doppler anemometer Mark II from DISA Electronics (Fig. 13). The argon laser was operated with the power stabilizer on and at 4880 Å. The laser beam entered the optical section of the anemometer, the 55L88 LDA transducer from DISA. The LDA transducer consisted of a beam splitter, an acousto-optic cell (Bragg cell) which translated the frequency of one laser beam by 40 MHz, a beam separator and a focusing lens. The focal length of the focusing lens used in the experiments was 120 mm. Together with a beam separation of 20 mm, the angle between the two laser beams, θ, was 9.52^{o}. The measurement volume at the e^{-2} points was 43 μm wide and

640 μm long. For detection of scattered light or fluorescence, a lens with a focal length of 135 mm and an F stop of 2.3 was placed approximately 1 cm from the measurement volume, and this provided an image of the measurement volume magnified approximately eight times. The lens was positioned at the same level as the measurement volume and approximately 20^{o} from the plane perpendicular to the plane formed by the two laser beams. The image of the measurement volume was projected onto the photodetector which consisted of a slit of 0.212 mm in width and 1 mm in length and a RCA Type C70042K photomultiplier. The dimensions of the slit were chosen to satisfy Eq. (18) and signal coherence. Because of the need for critical focusing of the image as well as the measurement volume, a ten times magnifier was used as a focusing aid. When detecting the fluorescence from the fluorescent tracers, two dielectric filters (custom made by Oriel Corporation) together with a Wratten number 12 filter were placed between the slit and the photomultipler. The glass substrate used for fabrication of the dielectric filters has virtually no detectable fluorescence due to excitation at 4880 $\mathring{A}$. This combination of optical filters was very effective and necessary in filtering the laser light (Fig. III-3)(see Appendix 3). To facilitate the positioning of the slit, the entire signal detection section was mounted on a precision linear range traversing platform, which was in turn mounted on an optical rail with vibration isolation.

Signal Processing

The anode current output from the photomultiplier carried the Doppler frequency and the acousto-optic modulation frequency when the Bragg cell

was in use. To optimize processing of this frequency, it was first mixed with a chosen frequency from the DISA 55L72 Range Translator. The frequency shifts provided by the range translator was adjustable between zero and 50 MHz in steps of 10k Hz. The AC component of the mixed output was then amplified by using a Hewlett-Packard 463A Precision Amplifier. This amplified signal was in turn filtered with an active narrow bandpass filter. This bandpass filter was designed specifically to handle the frequencies resulting from the flow rates used in the experimental system. Finally, the filtered signal was processed with a frequency counter fabricated in our laboratory. The frequency counter determined with precision the time durations of 5 and 8 cycles of the filtered signal. A comparison of the two times was then made and, if within the pre-set accuracy tolerance, the time duration of 8 cycles was converted into time duration of one cycle by scaling and then stored in a storage register. Different logics were incorporated to eliminate various erroneous signals. The accuracy of the 5:8 cycles comparison was set to be no larger than 4%. A digital output of the most recently validated data could be obtained from the storage register. Because of the lack of capability to handle digital data in our laboratory, the digital output was converted into analog output by a digital-to-analog converter. The analog output was given as a voltage proportional to the time of one cycle of the signal, thus was inversely proportional to the frequency of the signal. A Hewlett-Packard 3465A digital multimeter was used to read the analog voltage output.

Data Acquisition

In each experiment, a suspension of a predetermined concentration

was circulated through the flow channel at the five given flow rates. Velocity profile across the center of the flow channel was measured by translating the slit in front of the photodetector across the images of the measurement volume for each flow rate. Since the measurement volume was shorter than the width of the flow channel, the measurement volume was positioned across the channel from one wall of the channel and the velocity profile measured across approximately 60% of the channel. Nine data points were obtained for each scan of the slit across the image. Each 'point' was approximately 3.8% of the width of the channel. The data scanning was repeated from two to three times. The location at which the maximum frequency was recorded was taken to be the center of the channel. From the data points, the velocity profile across half of the channel was determined. An advantage in using half of the channel instead of lengthening the measurement volume was, besides the limitation of optics, a reduction in the error caused by the dispersion of the laser beam by the suspensions.

The measurements of velocities of the suspensions without fluorescent tracers produced velocity profiles of the suspended phase in the suspensions. After the measurements of particle velocity were completed, approximately 10^{-3}% by volume of the fluorescent tracers were then added to the suspensions. This very dilute concentration of tracers ensured the presence of not more than one tracer particle in the 'point' of measurement at each instant. The experiments were then repeated, with the addition of the optical filters, to obtain a better approximation of the velocities of the fluid phase. A complication arose from the use of fluorescence: the relaxation time of fluorescence was approximately 10 μsec, while the use

of a 40 MHz modulation in the Bragg cell gave rise to a timescale of interference fringe movement of 25 nsec. The closeness of the two timescales reduced greatly the modulation in the intensity of fluorescence due to the presence of the fringe pattern. To circumvent this problem, the Bragg cell was turned off when velocity was measured from the tracers, requiring the realignment of the laser beams. The fluorescence modulation, with a frequency equal to the Doppler frequency, was at a much lower frequency than the scattered signal. Noise from the electronics used, however, was much larger at lower frequencies, and could not be filtered out directly with the bandpass filter. This noise placed a lower limit of approximately 800 Hz, or equivalent to a velocity of approximately 0.3 cm sec^{-1}, on the measurable frequency. Velocities of the tracers very close to the wall or at very low flow rates were therefore not measured. This limitation could have been relieved by processing the signal differently (Appendix 2), but this was not attempted here because of time requirements. Another possible approach would be to use a frequency lower than 40 MHz to modulate the laser beam, achievable by using a rotating diffraction grating instead of a Bragg cell.

For each velocity point, about 30 or more data points were taken from the analog output to calculate the average velocity. For the dispersed phase, this required approximately 1 - 2 minutes of data collection. Because of a lower data rate, a time of approximately 3 minutes was used for each velocity point of the tracers.

V. Results and Discussion

A check on the performance of the entire experimental system was first undertaken by circulating tap water through the channel and measuring the velocity distribution across the channel. The velocity field was measured from both the Doppler frequency from light scattered by natural contaminant in the water as well as by seeding the flow with fluorescent tracers and measuring the amplitude fluctuations of the fluorescence. The axis of the measurement volume, as formed by the intersection of the laser beams, was positioned along the median plane of the flow channel. The resultant normalized velocity profiles are given in Fig. 14. As can be seen, the two measurements gave virtually the same velocity distribution. This measured velocity distribution agreed well with the theoretical velocity profile of the flow when fully developed (Eq. (27)), plotted as a solid line in Fig. (14). The velocity profile did not change when the measurement volume was moved along the vertical axis of the flow channel over a distance of approximately 6 mm, again showing that the flow was fully developed. Only when the point of measurement was very close to the wall, $x(h \simeq 0.97)$, was there a small, but noticeable departure of the measured velocity from the theoretical value. This could have been caused by a slight error in the location of the point, resulting in a noticeable error due to the presence of a large velocity gradient near the wall. The large velocity gradient near the wall could also have resulted in a biasing of the measured velocity, resulting from the finite size of the 'point' of measurements (Edwards et al., 1971).

Figures 15 - 24 are plots of the measured velocity profiles of the different suspensions at various flow rates. The velocities were

normalized with respect to the velocity of a Newtonian fluid at the center of the channel at the corresponding flow rates. The position of the point of measurement was normalized with respect to the half width, h, of the flow channel. For the model suspensions of polystyrene latex spheres, the velocity profiles of both the suspended particles and the tracers, at low volume concentrations, ϕ, were essentially the same as for a Newtonian fluid. A slight blunting of the velocity profile of the suspended particles near the center of the channel was observed at $\phi = 0.048$, while the velocity profile of the fluorescent tracers still resembled that of a Newtonian fluid. At $\phi = 0.097$ and above (Fig. 15 - 17), the velocity profiles of both the suspended particles and the tracers were blunted near the center of the channel. The difference in the velocities of the suspended particles and the tracers was greatest at the center of the channel. It vanished at about half way between the center and the wall, and increased again near the wall of the channel. The tracers moved faster than the suspended particles near the center of the channel and slower than the suspended particles near the wall. Both the bluntness of the velocity profiles and the difference in velocities increased with increasing ϕ, (Figs. 15 - 19). At $\phi = 0.20$ and a flow rate of 0.55 cm^3 sec^{-1}, the velocity of the suspended particles at the center of the channel was approximately 11% below that of a Newtonian fluid, while the velocity of the tracers was approximately 6% below that of a Newtonian fluid. For a given ϕ, the blunting of the velocity profiles also showed a slight increase with increasing flow rate. At $\phi = 0.20$, the normalized velocity of the suspended particles at the center of the channel at $Q = 2.48 \times 10^{-2}$ cm^3 sec^{-1} was approximately 5% greater than the corresponding velocity at $Q = 0.55$ cm^3 sec^{-1}.

For the suspensions of whole red blood cells, there was more noise in the scattered and fluorescent signal. The higher noise level introduced more fluctuations in the anode current, in terms of both amplitude and frequency. The increase in the noise level was most likely a result of the increased attenuation and dispersion of the laser beams by the suspensions. In order to improve the accuracy of measurement, more data points were used for the calculation of each average velocity point, and only dilute suspensions of red blood cells were used. The highest hematocrit used was 7.8. For these dilute suspensions of whole red blood cells, the velocity profiles of both the erythrocytes and tracers were essentially the same as that of a Newtonian fluid at all flow rates.

For the suspensions of ghost erythrocytes, the velocity profiles of both the ghost cells and the tracers resembled that of a Newtonian fluid, up to a volume fraction of 0.20, a value much higher than for the suspensions of latex spheres. At ϕ = 0.20, the velocity profiles of the ghost cells and the tracers became slightly blunted at the center while the velocity profile of the tracers remained about the same as that of a Newtonian fluid. Above ϕ = 0.20, the velocity profiles of both the ghost cells and the tracers were blunted at the center of the channel (Figs. 20 - 22). As in the case of suspensions of rigid latex spheres, the bluntedness increased with increasing ϕ (Figs. 23 - 24). At ϕ = 0.33, the velocity of the ghost cells and the tracers at the center of the channel were approximately 16% and 11%, respectively, below that of a Newtonian fluid at the corresponding flow rates. The difference in the velocity profiles of the ghost cells and the tracers also increased gradually with increasing concentration. However, no dependence on the flow rate of the

normalized velocity profiles was observed.

At volume fractions, ϕ, of 0.29 and 0.33 (Figs. 22 - 23), the velocity of the ghost cells, $\bar{V}_p$, was less than that of the tracers, $\bar{V}_t$, at the center of the channel. Away from the center of the channel, $\bar{V}_p$ gradually became greater than $\bar{V}_t$. Close to the wall of the channel, $\bar{V}_p$ was again smaller than $\bar{V}_t$. This change near the wall of the channel was not observed with the ghost cell suspensions at lower ϕ, or with the suspensions of latex spheres.

The dependence of the normalized velocity distributions of the suspensions of the latex spheres on the flow rates and the lack of such a dependence for suspensions of ghost cells was unexpected. The ghost cells are fluid-like and deformable under shear. It is therefore reasonable to expect suspensions of ghost cells to behave as shear-thinning fluids, so that the normalized velocity profiles vary with flow rates. The pressure drop along the flow, which was not measured in the experiment, should also have a non-linear dependence on flow rate. The rheological behavior of the suspension of latex spheres, on the other hand, was expected to be only a function of the volume fraction ϕ for the moderate values of ϕ used (Krieger, 1972). In the experimental study performed by Karnis et al. (1966), the velocity distribution of the dispersed phase was not observed to depend on flow rate. The slight dependence on flow rates of the normalized velocity profiles was therefore unexpected.

It was possible that at the shear rates experienced by the ghost cells, they behaved like rigid disk and the shear thinning behavior was not significant. For suspensions of rigid disks, Karnis et al. (1966) observed that for $\phi \leq 0.30$, velocity distribution was independent of flow

rate. Goldsmith and Marlow (1972) observed no deformation of the ghost cells up to a shear stress of 1 dyne cm^{-2}, or equivalently to a shear rate of approximately 100 sec^{-1} for the suspending fluid used in this study. The maximum shear rate experienced by the ghost cells was of the order of 150 sec^{-1}, and any shear-thinning behavior that might have been present was probably too small to be detected.

The small dependence on the flow rate of the normalized velocity profile for the suspensions of latex spheres could have been caused by the relatively large size of the particles used. The average diameter of the polystyrene spheres was approximately 1/22 the width of the channel. Interactions between particles and the walls of the channel could have been substantial (Goldsmith and Mason, 1967), and the suspensions possibly could not be viewed as homogeneous within the channel. This hypothesis can be tested by varying the size of the particles used. The effect of interactions between the particles and the wall should increase with increasing size. This test was not carried out due to the lack of particles of different sizes at the time the study was made.

The cause of the observed difference in velocity distributions between the two phases in more concentrated suspensions cannot be readily understood either. For the experimental conditions used, this difference in velocities was mostly a function of the concentration of the suspended particles. The relative difference in velocities of the two phases increased with concentration but remained approximately the same at different flow rates. This difference in velocities did not appear to be simply an effect of large particle sizes as it was present in suspensions of ghost cells as well as in the model suspensions.

As mentioned in Section II, few attempts have been made to measure simultaneously the velocity distributions of both phases in suspension flows. The only detailed study available was performed by Karnis et al. (1966a,b), in the study of suspensions of rigid particles undergoing Couette and Poiseuille flows. Karnis et al. approximated the fluid phase velocity by measuring the average velocity of aluminum tracers, and concluded in Poiseuille flow, the velocities of the suspended particles and suspending liquid were identical at all ϕ and flow rates used. It should be noted, however, that the aluminum tracers used were relatively large in size, approximately equal to the size of the suspended particles in some cases. Furthermore, the experimental conditions of the study of Karnis et al. were different from those employed in this study: the Poiseuille flows were flows in tubes and, because of the use of a photographic method, the maximum flow rates and the resultant wall shear rates were lower than those in this study.

In the study of Karnis et al. (1966a), it was observed that the velocity profile of the suspended particles corresponded to complete plug flow at sufficiently high ϕ when the particle size was large with respect to the radius of the channel ($\phi \geq 0.33$ and $a/R_o \geq 0.112$). The plug flow extended from the center to a distance equal to the diameter of the suspended particles from the wall. The particles next to the wall were seen to rotate, though the rotation often stopped after a time and sometimes started again, suggesting stick-slip behavior. As the size of the suspended particles was reduced, the blunting of the velocity profile was seen to decrease and the velocity gradually vanished as the wall was approached. Thus for the same flow rate, the velocity of larger suspended

particles was slower than smaller suspended particles near the center of the channel and faster than smaller particles near the wall. This result, however, does not directly explain the difference in velocity between the suspended particles and the fluorescent tracers in this study. The suspended particles and fluorescent tracers constituted particles of two distinct sizes in the same suspension. While in the study of Karnis et al., particles of different size distributions existed in different suspensions. The behavior of suspensions with suspended particles of two or more sizes cannot be directly extrapolated from the rheological behaviors of monodisperse suspensions.

It thus seems useful to perform an extensive study of multidisperse suspensions. One approach to such a study is to vary both the size and concentration of the fluorescent tracers in suspensions with another distribution of suspended particles of a different size. The observed behavior of such suspensions not only will give further insight to the results observed in this study, but also will be applicable to naturally occurring, and seldomly monodisperse, suspensions.

The difference in velocities between the suspended particles and the tracers raised the possibility of a non-uniform spatial distribution in the concentration of the suspended particles. The experimental method used in this study could be adopted to measure the concentration distribution of the suspended particles (see Appendix 4). Because of the lack of the proper recording facilities in the laboratory, this measurement was not carried out in the study.

VI. Conclusions

It was demonstrated that the experimental method developed in this study was capable of measuring the velocity distributions of moderately concentrated suspensions. The use of small tracers provided an approximation to the velocity distribution of the suspending fluid, while the scattered signal from the suspended particles gave a direct measurement of their velocity distribution. The accuracy of the method was confirmed by flowing water through the channel and measuring its velocity distribution using both techniques.

The observed behavior of the model suspensions of rigid latex spheres was similar to the suspensions of ghost cells. However, the behavior of suspensions of rigid latex spheres showed a stronger dependence on concentration, and a dependence on flow rates which was not observed with suspensions of ghost cells. The difference in the observed behavior of the two types of suspensions indicated that each type of suspension cannot be represented by the other. Since the volume fraction of the ghost cell suspensions was varied to 0.33, a value close to the hematocrit of human blood under normal physiological conditions, the results of the experiments are applicable to blood flow and, because of the geometry of the flow channel used, to artifical hemodialysers.

VII. Suggestions for Future Work

In this study, a large amount of time was spent on the development of an appropriate experimental method to study flowing suspensions. Now that the experimental method developed has been tested and shown to be efficient in the measurement of velocity distributions in suspension flows,

it should be taken advantage of and used for more extensive studies of different suspensions. Based on some of the observations of this study, the following is a list of suggestions to be incorporated in future studies:

(1) Increase the Range of Concentrations of Suspended Particles. Since both the velocity profiles and the observed difference in velocities of the two phases were strongly dependent on ϕ, it will be useful to perform a more extensive study by extending the range of ϕ. In order to study more concentrated suspensions of latex spheres, a better match of the refractive indices of the two phases will be necessary. For suspensions of ghost cells, increasing the concentration by an additional 10 - 15% should not create any drastic degradation in the transparency of the suspensions.

(2) Increase the Range of Flow Rates. The flow rate was seen to affect the normalized velocity distribution of the suspensions of latex spheres, while the suspensions of ghost cells were unaffected. The effect of inertia of the particles and deformation of the ghost cells can be studied by increasing the range of flow rates.

(3) Measure the Pressure Drop along the Flow. As discussed in Section V, suspensions of ghost cells were expected to be shear-thinning rheologically, while suspensions of rigid latex spheres were not expected to exhibit shear-thinning (in fact, sufficiently concentrated suspensions of rigid particles were observed to be shear-thickening (Krieger, 1972)). The

behavior of the suspensions can be identified by measuring the pressure drop along the flow at different flow rates.

(4) Determine the Effect of the Relative Size of the Particles to the Width of the Channel. Wall effects, if present, should be a function of the relative size of the suspended particles to the size of the flow channel. For latex particles, it is possible to obtain particles of different sizes from commercial suppliers. The size of the red blood cells, however, cannot be readily changed (small changes can be affected by using bloods other than human blood). In this case, the size of the channel can be varied.

(5) Measure the Spatial Concentration Distribution of the Suspended Particles. The concentration distribution of the suspended particles is important to the transport properties of the flowing suspensions. It is known that the transport of heat and mass, for example, is dependent on the concentration (Batchelor and Green, 1972; Leal, 1973; Nir and Acrivos, 1976). By using the method outlined in Appendix IV, the concentration distribution can be measured.

(6) Study Multidisperse Systems. For reasons given in Section V, it will be useful to study multidisperse suspensions. The approach outlined in Section V can be used to distinguish particles of different size distributions suspended in the same suspensions.

References

Asano, M., Yoshida, K. and Tatal, K., Bulletin Institute Public Health 13, pp. 201-204, 1966.

Batchelor, G. K. 'Transport Properties of Two-Phase Materials with Random Structure', Ann. Rev. Fluid Mech. 6, pp. 227-255, 1974.

Batchelor, G. K., Green, J. T., 'The Determination of the Bulk Stress in a Suspension of Spherical Particles to Order C^2', J. Fluid Mech. 56, pp. 401-427, 1972.

Block, E. H., 'A Quantitative Study of the Hemodynamics in the Living Microvascular System', Am. J. Anat. 110, p. 125, 1962.

Born, G. V. R., Vlachos, N. and Whitelaw, J. H., 'Measurements of Blood Velocity and Their Implications for Non-Uniform Viscosity Laws', Imperial College, Mech. Eng. Dept. Report, 1975.

Branemark, P. I., Jonsson, I., 'Determination of the Velocity of Corpuscles in Blook Capillaries, a Flying Spot Device', Biorheology 1, p. 143, 1963.

Brenner, H., 'Suspension Rheology', in Progressive Heat and Mass Transfer, Vol. 5, Pergamon Press, Oxford, England, W. R. Schowalter, ed., 1972.

Bugliarello, G. Sevilla, J., 'Velocity Distribution and Other Characteristics of Stead and Pulsatile Blood Flow in Fine Glass Tubes', Biorheology, I, pp. 85-107, 1970.

Chenoweth, A. J., Gaddy, O. L. and Holshoreser, D. F., 'Carbon Disulfide Traveling Wave Kerr Cells', Proc. IEEE 54, pp. 1414-1429, 1966.

Copley, A. L., 'Flow Properties of Blood and Other Biological Systems', edited by Copley, A. L. and Stainsby, G., p. 97, Pergamon Press, Oxford, 1960.

Copley, A. L., Staple, P. H., 'Haemomeological Studies of the Plasmatic Zone in the Microcirculation of the Cheek Pouch of Chinese and Syrian Hamsters', Biorheology 1, 3, 1962.

Copley, A. L., Scott Blair, G. W., Rheologia Acta. Band. 1, 170, 1968.

Cox, R. G., Mason, S. G. (1971), 'Suspended Particles in Fluid Flow through Tubes', Ann. Rev. Fluid Mech. 3, pp. 291-318, 1971.

Cummins, H. Z., Knable, N., Yeh, Y., 'Observation of Diffusion Broadening of Rayleigh Scattered Light', Phys. Rev. Letters 12, pp. 150-153, 1964.

Dodge, J. T. Mitchell, C., Hanahan, D. J., 'The Preparation and Chemical Characteristics of Hemoglobin-Free Ghosts of Erythrocytes', Arch. Biochem. Biophys. 100, pp. 119-130, 1963.

Durrani, T. A. and Greated, C. A., 'Laser Systems in Flow Measurement', Plenum Press, New York, 1977.

Durst, F., Development and Application of Optical Anemometers. PhD Thesis, University of London, 1972.

———, Personal Communication, 1975.

———, Melling, A., Whitelaw, J. H., Principles and Practice of Laser Doppler Anemometry. Academic Press, 1976.

Edwards, R. V., Angus, J. C., French, M. J., Dunning, Jr., J. W., 'Spectral Analysis of the Signal from the Laser Doppler Flowmeter: Time-Independent Systems', J. Appl. Phys. 42, 1971.

Einstein, Albert, 'Investigations on the Theory of the Browian Movement', Dover, New York, 1956.

Foreman, Jr., J. W., George, E. W., Lewis, R. D., 'Measurement of Localized Flow Velocities in Gases with a Laser Doppler Flowmeter', Appl. Phys. Letters 7, p. 77-78, 1965.

Gaylor, J. D. S., 'Thin Film Blood Flow in Rectangular Channels with Application to Artificial Kidney Haemodynamics', J. Biomechanics 6, pp. 241-251, 1973.

Goldsmith, H. L., 'Red Cells and Rouleaux in Shear Flow', Science 153, pp. 1406-1407, 1966.

————, 'The Microrheology of Red Blood Cell Suspensions', J. Gen. Physiol. 52, pp. 55-285, 1968.

————, Mason, S. G., 'The Microrheology of Dispersions', Rheology, Vol. 4, Ed. F. R. Eirich, Academic Press, 1967.

————, Marlow, J., 'Flow Behavior of Erythrocytes. I. Rotation and Deformation in Dilute Suspensions', P. Roy. Soc. B 182, pp. 351-384, 1972.

————, Personal Communication, 1975.

Goldstein, R. J., Kried, D. K., 'Measurement of Velocity Profiles in Simulated Blood by Laser-Doppler Technique', B. Am. Phys. S., Series II. 15, p. 1539, 1970.

Gordon, E. I., 'A Review of Acousto-Optical Deflection and Modulation Devices', Proc. IEEE 54, pp. 1391-1401, 1966.

Han, L. S., 'Hydrodynamic Entrance Lengths for Incompressible Laminar Flow in Rectangular Ducts', J. Appl. Mech., pp. 403, 1960.

Jeffrey, D. J. and Acrivos, A., 'The Reolgoical Properties of Suspensions of Rigid Particles', AIChE J. 22, pp. 417-432, 1976.

Jinescu, V. V., 'The Rheology of Suspensions', Intern. Chem. Eng. 14, pp. 397-420, 1974,

Kaminow, I. P., Turner, E. H., 'Electro-Optic Light Modulators', Proc. IEEE 54, pp. 1374-1390, 1966.

Karnis, A., PhD Thesis, McGill University, Montreal, Canada, 1966.

———, Goldsmith, H. L., Mason, S. G., 'The Kinetics of Flowing Dispersions. I. Concentrated Suspensions of Rigid Particles', J. Colloid. Interface Sci. 22, pp. 531-553, 1966a.

———, 'The Flow of Suspensions through Tubes. V. Inertia Effects', Can. J. ChE 44, pp. 181-193, 1966b.

Krieger, I. M., 'Rheology of Monodisperse Latices', Adv. Colloid, Interface Sci. 3, pp. 111-136, 1972.

Krogh, A. The Anatomy and Physiology of Capillaries. Hafner, New York, 1929.

Leal, L. G., 'On the Effective Conductivity of a Dilute Suspension of Spherical Drops in the Limit of Low Particle Peclet Number', Chem. Eng. Comm. 1, pp. 21-31, 1973.

Lee, S. L., Einav, S., 'Migration in a Laminar Suspension Boundary Layer Measured by the Use of a Two-Dimensional Laser-Doppler Anemometer', Prog. in Heat and Mass Transfer 6, pp. 385-402, 1972.

Madge, D., Elson, E. L. and Webb, W. W., 'Fluorescence Correlation Spectroscopy. II. An Experimental Realization', Biopolymers 13, pp. 24-60, 1974.

Merzkirch, W., Flow Visualization. Academic Press, 1974.

Mishima, H., Asakura, T., Nagai, S., 'A Laser Doppler Microscope', Opt. Comm. 11, pp. 99, 1974.

Munro, P. A. G. Advances in Optical and Electron Microscopy (Edited by Barer, R. and Cosslett, V. E.). Academic Press, New York, 1966.

Nir, A., Acrivos, A., 'The Effective Thermal Conductivity of Sheared Suspension', J. Fluid Mech. 78, pp. 33-40, 1976.

Rudd, M. J., 'A New Theoretical Model for the Laser Dopplemeter', J. Phys. E.: Sci. Instrum. 2, p. 55, 1969.

Segre, G., Silberberg, A., 'Behavior of Macroscopic Rigid Spheres in Poiseuille Flow. Part I. Determination of Local Concentration by Statistical Analysis of Particle Passages through Crossed Light Beams', J. Fluid Mech. 14, pp. 115-135, 1962.

Somerscales, E. F. C., 'Fluid Velocity Measurement by Particle Tracking', 1st Symposium on Flow - Its Measurement and Control in Science and Industry. Paper No. 1-4-163. The Inst. Society of America, Pittsburgh, Pennsylvania, 1971.

Stevenson, W. H., Santos, R. D. Mettler, S. C., 'A Laser Velocimeter Utilizing Laser-Induced Fluorescence', Appl. Phys. Letters 27, pp. 395-396, 1975.

Taylor, M., Robertson, J. S., Inst. J. Exp. Biol. 32, p. 731, 1954.

Vlachos, N., Whitelaw, J. H., 'Measurement of Blood Velocity with Laser Anemometry', Proc. of 2nd Int. Workshop on Laser Anemometry, Purdue University 1, 521, 1974.

Wayland, H., Johnson, P. C., 'Erythrocyte Velocity Measurement in Microvessels by a Two-Slit Photometric Method', J. Appl. Physiol. 22, pp. 333, 1967.

Wiederhielm, C. A., Meth. Med. Res. 11, p. 212, 1966.

Wiederhielm, C. A., Billig, L. Hemorheology, p. 681 (Edited by Copley, A. L.). Pergamon Press, Oxford, 1968.

Wintrobe, M. M., Clinical Hematology. Lea and Febiger, Philadelphia, 1967.

Yeh, Y., Cummins, H. Z., 'Localized Flow Measurements with an He-Ne Laser Spectrometer', Appl. Phys. Letters 4, p. 176, 1964.

Appendix I: Velocity Measurement with Fluorescent Particles: The Case of Many Particles.

In Section IV, the problem of measurement of velocity by using fluorescent tracers was discussed. It was shown that fluctuations in the amplitude of fluorescence, due to the presence of the interference pattern, have the same frequency as the Doppler frequency in the case of light scattering. Since the tracer particles are necessarily small in size, it is possible for many tracers to be present within the measurement volume simultaneously. The problem of detecting the fluorescence amplitude from many particles and still being able to extract the frequency information is different from the similar problem of measuring the Doppler frequency from light scattering by many particles. As will be shown, the frequency cannot be measured directly from the resultant amplitude from the fluorescence of all the particles, but can be recovered from the autocorrelation of the resultant amplitude.

As shown in Section IV, the anode current, I, from the photodetector, as a result of the fluorescence emission from one particle, can be written as

$$I \sim \left[1 + \cos\left(\frac{4\pi}{\lambda} vt \sin\theta\right)\right] \text{ rect } \left(\frac{vt}{D}\right) \qquad (I.1)$$

If N particles are present in the measurement volume simultaneously, the detected current for the nth particle, I_n, that enters the measurement volume at time t_n, would be

$$I_n \sim \left[1 + \cos\left(\frac{4\pi v}{\lambda} (t - t_n)\sin\theta\right)\right] \text{ rect } \left[\frac{v(t - t_n)}{D}\right]$$

The total current, I, resulting from all N particles, is

$$I \sim \left[\sum_{n=1}^{N} 1 + \cos\left(\frac{4\pi v}{\lambda}(t - t_n)\sin\theta\right)\right] \text{ rect}\left[\frac{v(t - t_n)}{D}\right] \qquad (I.2)$$

The above expression assumes the amplitude of fluorescence from each tracer particle is identical. I is simply a sum of the contribution from each particle because fluorescence is an amplitude (incoherent) measurement.

For a continuous flow of particles, the number N can be interpreted as the average number of particles within the measurement volume of length D at any time. The expression can therefore be simplified by dropping the rect-function:

$$I \sim \sum_{n=1}^{N} \left\{1 + \cos\left[\frac{4\pi v}{\lambda}(t - t_n)\sin\theta\right]\right\}$$

The expected value of I, $\langle I \rangle$, can be found if the density function of t_n is known. For a sufficiently large N, the density function can be approximated by a uniform distribution. In this case,

$$\langle I \rangle \sim N. \qquad (I.3)$$

$\langle I \rangle$ therefore does not contain any frequency information. The frequency, however, can be retrieved from the autocorrelation of I, as shown in the following:

The detected current can be idealized and represented by the real part of the function g(t):

$$g(t) \sim \sum_{n=1}^{N} e^{i(\omega t + \phi_n)}$$

where $w = \frac{4\pi v}{\lambda}\sin\theta$ and $\phi_n = \frac{4\pi v}{\lambda} t_n \sin\theta$

Now consider the autocorrelation of g(t). Starting with g(t), the following expression is formed:

$$g(t + \Delta t)xg(t) \sim \sum_m \sum_n e^{i\left[\omega(t+\Delta t) - \omega t + \phi_m - \phi_n\right]}$$

$$\sim e^{i\omega\Delta t} \sum_m \sum_n e^{i(\phi_m - \phi_n)}$$

$$\sim e^{i\omega\Delta t}\left[N + \sum_{m\neq n}\sum e^{i(\phi_n - \phi_n)}\right] \qquad (I.4)$$

The expected value, Rg, is given by

$$Rg = \langle g(t + \Delta t)xg(t)\rangle \sim N\, e^{i\omega\Delta t} + N(N - 1)\Phi(1)\Phi^*(1) \qquad (I.5)$$

Here the phases ϕ_m, ϕ_n are assumed to be independent for different m, n. Φ is the Fourier transform of the probability density of ϕ_n.

For a uniform distribution or a normal distribution with large standard deviation, it can be shown that the second term on the right-hand side of Eq. (I.5) vanishes. Thus, with this idealized model, the autocorrelation Rg has a simple sinusoidal term ω and its transform, the spectral intensity, is a delta function at ω.

APPENDIX II. Noise Reduction in the Measurement of Velocity Utilizing Fluorescent Tracers.

Introduction

The problem of processing signals with high levels of noise, as applicable to this experimental study of suspension flows, is discussed here. The problem often appears when the strength of the signal is weak and a high gain is necessary for its detection. This was the case in this experimental measurement of velocities in suspensions. In the experiment, fluorescent tracers were used to track the velocity of the suspending fluid. The extremely weak fluorescence from the tracers was sometimes totally masked by the comparatively high levels of noise. Because of the random nature of the noise, a relatively straightforward procedure could be used to greatly reduce the noise and to recover the signal.

Problems in the Detection of Signal from Fluorescent Tracers

In this experimental study of suspension flows, one of the objectives was to measure the velocities of both the fluid and the dispersed phase in the flow. The velocity of the fluid could be approximated by tracking the velocity of very small tracers seeded in the suspension. Small fluorescent tracers were used in the study. The tracers used were spherical latex particles with a diameter of 0.8 micron. The fluorescent dye used, fluorescein isothiocyanate, was chemically attached to render the particles fluorescent when excited. The small size of the particles set a limit on the amount of dye inside each particle. The best one could do was to use the highest possible concentration of dye within each particle. Because

of the high quantum yield of the dye, the spatial extinction coefficient was very high and the dye molecules that actually contributed to the fluorescence were the ones on the surface of each particle. The fluorescence signal was often of $O(10^{-3})$ the signal strength from scattered light by particles constituting the dispersed phase of the suspensions. In order to detect this very weak fluorescence signal, the current amplification of the photodetector was typically set at $\sim 7 \times 10^6$. The output from the photodetector was further amplified $\sim 10^2$ times before it was processed electronically. As a result of this very large amplification used, high levels of random noise often interfered with the processing of the signal and reduced the rate of data acquisition, and sometimes completely masked the fluorescence signal. Figure II-1 shows a record of a typical 'acceptable' signal from the photodetector after electronic filtering. The frequency of the signal was counted using a frequency counter. The noise in this case reduced the rate of data acquisition of the counter to approximately 15% of the maximum rate possible, as determined from the frequency of the signal. Because of the logic used in the validation of data by the frequency counter, a very low rate in data acquisition could introduce a bias in the output for inputs with modulation in frequency. In addition, the time period used in the measurement had to be lengthened.

Reduction of Noise

Since most of the noise in the experimental system came from the use of high amplification, it was suspected that the noise was random in nature, and therefore should be mostly uncorrelated temporally. In this case the noise could be greatly reduced by performing an autocorrelation

on the signal.

The experimental procedure was quite straightforward and similar to the procedure used in Section IV. The main difference was: instead of feeding the amplified and filtered signal from the photodetector into the frequency counter, the signal was recorded on magnetic tape using a Hewlett Packard 3960 Instrumentation Recorder. The recording was made at a speed of 15 ips in order to make use of the widest bandwidth of the recorder. The recorded signal was then played back at 3 3/4 ips and digitized using an analog-to-digital converter. The slower playback speed allowed the use of a slower rate of digitization. To prevent any loss of data in digitizing the signal, the rate of digitization used was at least five times the expected frequency of the recorded signal. An autocorrelation on the digitized data was then calculated by using the following expression:

$$R(k\Delta t) = \frac{1}{n} \sum_{m=1}^{n} x(m\Delta t) \cdot x\left[(m+k)\Delta t\right] \qquad k = 1,2,\ldots$$

where Δt = time internal between two consecutive digitized data points

= 1/(rate of digitization)

n = number of digitized points used in autocorrelation

$x(m\Delta t)$ = digitized data point at time $m\Delta t$

$R(k\Delta t)$ = autocorrelation of x at a time lag of $k\Delta t$

A fast Fourier transform was then performed on R to obtain its power spectrum. The mean frequency and the bandwidth of the fluorescence signal could then be obtained directly from the power spectrum.

The above procedure was necessary because of the lack of on-line

computation capability in our laboratory. It is conceivable to use the frequency counter with a mini-computer to improve the efficiency of the above procedure.

In this study, the recorded signals were obtained from locations close to the wall of the flow channels, where difficulties in the detection of signals were experienced before. Moderately concentrated suspensions ($\sim$25% by volume of dispersed phase) of rigid latex spheres were used for the flows. The frequencies of the signals were calculated from the known flow rates and the points of measurement for comparison with the measured values. In order to facilitate the recording, a slightly higher amount ($\sim 10^{-2}$% by volume) of the fluorescent tracers was used in each suspension.

Results

Figures II-1, II-4 and II-7 are plots of data recorded on magnetic tape. The signal in figure II-1 was typical of an 'acceptable' signal to the frequency counter. In this case the rate of data validation by the counter was approximately 15% of the maximum rate. The autocorrelated signal, as seen in figure II-2, showed a definite reduction in noise and the appearance of 'bursts' of signal. These 'bursts' of signal, due to the passage of individual particles through the measurement volume, is characteristic of laser Doppler anemometry as well as of fluorescent particles at low concentration of particles. Figure II-4 was a record of an 'unacceptable' signal to the frequency counter. Visual inspection of the record did not give any indication of existence of any signal. The autocorrelated signal, shown in figure II-5, seemed to indicate a signal contaminated by higher frequency noise. The power spectrum of the signal,

given in figure II-6, showed a very distinct peak at about the expected frequency. Figure II-7 gives a plot of a signal recorded under identical conditions as the signal in figure II-4. The autocorrelated signal, in figure II-8, gave sign of a signal becoming uncorrelated quickly. The peak in the power spectrum, given in figure II-9, gave the correct frequency with a much lower amplitude. The scheme worked well for these signals with such extremely large amount of noise. However, the scheme would only work for the time period when a signal existed. Since it was impossible in many cases to determine whether a signal existed by visual examination of the digitized signal, it was important to use sufficient fluorescent particles to ensure a signal to exist at all times.

Conclusions

An effective way to reduce the noise and retrieve signals in this experimental measurement of velocity in suspension flows was demonstrated. The method worked well enough to detect signals when they seemingly were totally masked by noise. Though signals from fluorescent particles in this study were used, the method should work equally well for laser Doppler anemometry. It should also be applicable to signals with frequency modulation, such as in the case of turbulence.

APPENDIX III: Optical Filtering in Measurements Utilizing Fluorescence.

The need and application of optical filtering in experimental measurements involving fluorescence is discussed here. Since the excitation source used in this experimental study was an argon laser, this discussion is limited to a laser exciting source. Furthermore, the dye fluorescein isothiocyanate, used in coating the tracer particles, is used as an example in the discussion. The principles involved, however, are applicable to systems utilizing other excitation and dyes.

The advantage of using laser light for excitation of a fluorescent dye lies, of course, in its highly concentrated intensity at one single frequency, thus providing a well-described light source. Extreme care must be exercised, however, to avoid any of the direct or scattered laser light getting into the photodetector. Scattering is especially important with suspensions as the suspended particles are usually excellent scatterers of light.

With fluorescence, the fluorescent emission is usually a broad spectrum while the laser is of a single frequency. There is usually a separation of 10-30 nm in frequency between the optimal excitation frequency and the fluorescence emission. With fluorescein, for example, the emission spectrum is approximately 510-590 nm (green-yellow) with a peak at approximately 515 nm, while the excitation with an argon laser is 488 nm. This relatively large separation makes it quite easy to filter out most of the laser light unless an extremely high sensitivity is required. This is the case in the use of fluorescent tracers in this study. The scattered light from 30 μ polystyrene particles, depending on the direction of detection

relatively to the direction of the laser beam, could be as high as 5000 times stronger than the fluorescence from the tracer particles. So the optical filter needed had to have a transmittance of less than 0.002% at 488 nm and little attenuation at or above 510 nm in order to have the fluorescence to be ten times stronger than the scattered signal.

In most studies involving fluorescence, it is adequate to use a long-pass color filter to filter out the excitation. These filters contain different color dyes and utilize the different absorbance characteristics of the dyes for filtration of different bandwidths. To filter out the 488 nm light and pass frequencies above 510 nm, for example, a yellow filter such as an $O(G_1)$ filter or the Kodak number 12 or 15 filter can be used. These filters almost totally absorb the 488 nm line. The dyes contained in these filters, however, emit a weak yellow-red fluorescence excited by the 488 nm light. So the measured transmittance of these filters at 488 nm, typically $\sim$0.1%, is actually a measurement of the intensity of fluorescence of these filters. This can be demonstrated as follows:

The transmission of the filter is governed by

$$I^{(n)} = I_o e^{-\varepsilon(n)}$$

where I_o = intensity of excitation at frequency n

$I^{(n)}$ = intensity of transmitted light at frequency n

$\varepsilon(n)$ = extinction coefficient of filter at frequency n.

The transmittance of the filter at frequency n, $T^{(n)}$, is defined as

$$T^{(n)} = \frac{I^{(n)}}{I_o} = e^{-\varepsilon(n)} .$$

If two filters are put together, the total transmittance should be

$$T^{(n)} = T_1^{(n)} T_2^{(n)}$$

where $T_1^{(n)}$, $T_2^{(n)}$ are the transmittances of the two filters, respectively. However, if the transmitted light is mostly fluorescence of the filter, the measured $T^{(n)}$ would be

$$T^{(n)} \approx T_1^{(n)}$$

where $T_1^{(n)}$ is the transmittance of the filter through which the unfiltered light first passes through. This is because the fluorescence from the first filter is of longer wavelength and thus passes through the second filter essentially unimpeded. The following table shows the expected and measured transmittance of the filters numbers 12 and 15.

%Trans-mittance / Filter Wavelength (nm)	#12(T_1)	#15(T_2)	#12 and #15 (expected = $T_1 \times T_2$)	#12 and #15 (observed)
480	0.19	0.14	0.0003	0.16
490	0.30	0.15	0.00045	0.25
500	0.39	0.24	0.00094	0.32
510	6.82	3.04	0.21	2.37
520	38.9	6.47	2.52	2.49

Thus at the shorter wavelengths, the transmittance measured was due mostly to fluorescence. Only at ~520 nm was the fluorescence sufficiently weak compared to the transmitted light at that frequency.

It would be more efficient to use an interference filter in place of

a color filter. However, most of the commercially available interference filters contain zinc sulphate, which is fluorescent in the green-yellow range.

In this study, a customized dielectric filter fabricated by Oriel Corporation was used. It has a transmittance of 0.21% at 488 nm and an average transmittance of 75% for wavelengths longer than 520 nm (Fig. III-1). As the diameter of the dielectric filter was almost twice as large as that of the photodetector used, the filter was split into two and stacked together without any adverse effects. The transmission characteristics of the two filters combined was very close to the expected value calculated from the values obtained from one filter (Fig. III-2).

In order to determine the transmittance of the filter system at 488 nm, the output of the argon laser at that line was used. The laser was operated at an output of 1 watt, and the transmittance was determined by measuring the power of the incident and transmitted light beam with a Spectra Physics power meter. At an output of 1 watt from the laser, the sensitivity of the measurement can be down to a transmittance of 0.0015%. The measured transmittance of the two dielectric filters combined was 0.039%. Combined with a number 12 filter, the overall transmittance was too low to be measured (Fig. III-3). The goal of a filter system with less than 0.002% transmittance at 488 nm was therefore accomplished.

It should be stressed that the goal cannot be accomplished by using a combination of color filters. This approach, however, had been taken by various investigators (Madge et al., 1974; Stevenson et al., 1975) in studies requiring similar sensitivity as in this study.

APPENDIX IV: Measurement of Concentration Distribution of Suspended Particles in a Flowing Suspension.

A scheme for measuring the concentration distribution of suspended particles in a flowing suspension is presented here. The scheme makes use of the laser Doppler system used in this study with the addition of a bandpass filter, to measure the concentration distribution.

The concentration of the suspended particles is to be measured directly from the Doppler signal. Consider first the case of a dilute suspension. A typical signal from the photodetector, represented graphically in Fig. (IV-1), consists of bursts of signals. Each burst is a result of a particle crossing the measurement volume. The frequency of the fluctuations within each burst is the Doppler frequency while the envelope has a frequency f governed by the time taken to transit the entire measurement volume:

$$f = \frac{v_x}{d}$$

where d is the width of the measurement volume and v_x is the component of velocity of the particle perpendicular to the longitudinal axis of the measurement volume.

On the other hand, the Doppler frequency, f_o, is given by

$$f_o = \frac{v_x}{s}$$

where s is the spacing between adjacent fringes within the measurement volume.

Since d is typically much larger than s, the frequency f_o is much higher than f. The two frequencies can therefore be easily differentiated

by using appropriate filters.

The Doppler signal was processed with a frequency counter in this study. The frequency counter, fabricated in this laboratory, used a design similar to frequency counters used in most LDA systems. An illustration of the working principles of frequency counters is given in Fig. IV-2. The DC-component and the envelop of the Doppler bursts are first removed with a high pass filter. The Doppler frequency is then converted into rectangular waves by using a zero-crossing technique. The time period of each cycle is timed with a high frequency clock ($\sim$500 MHz) in the counter. A comparison of the time periods of two different numbers of cycles (e.g. 5 cycles and 8 cycles) is then made. If the two time periods agree to some predetermined value, the time of one cycle is given as a data point. At the same time, a sync pulse is given in the output to signify the validation of a data point. By counting the number of sync pulses, the number of data points validated in a given time period can be found.

Since each Doppler burst is a result of a particle crossing the measurement volume, the number of particles crossing the measurement volume within a given time interval is equal to the number of Doppler bursts within that time interval. The number of bursts can be counted by modifying the above procedure slightly (Fig. IV-3). Instead of using a high-pass filter, a bandpass filter is used to remove the Doppler frequency and the DC-component, but retain the envelopes of the bursts. Here, the number of bursts rather than the frequency of each burst is of interest. The time period of each burst is therefore not counted in this case. Instead, a sync pulse is generated for each cycle by using some crossing at a prede-

termined amplitude. The number of sync pulses in a given time period is then counted to yield the number of bursts. The concentration of the particles, ϕ, at the point of measurement is proportional to the number of bursts, n, in a unit time interval and the velocity of the particles. The velocity is measured separately by LDA. To find the concentration, n is divided by the velocity of the particles at that point. The relative concentration distribution across the flow channel is measured by moving the point of measurement across the flow channel. Since the average concentration of the suspension is known, the concentration distribution can be calculated readily.

The above procedure can be applied to fluorescent particles as well since the anode current in this case looks the same as from scattered signals.

As the concentration of the suspended particles increases, the Doppler bursts begin to overlap. Eventually, it becomes impossible to distinguish individual bursts at high concentrations. This problem can be circumvented by coating a small percentage of the suspended particles with a fluorescent dye and by detecting only the bursts from the fluorescent signal. By knowing the relative concentration of the fluorescent particles to the particles with no fluorescent dye, the concentration distribution of the particles can again be found.

Figure Captions

Figure 1: Projected interference fringe pattern.

Figure 2: Light scattering from a small particle.

Figure 3: Dual scatter system.

Figure 4: Fringe pattern from two intersection laser beams of equal frequencies.

Figure 5: Diffraction limit d in the focusing of a laser beam.

Figure 6: Modified laser Doppler system.

Figure 7: Geometric considerations in the focusing of the measurement volume.

Figure 8: Geometric considerations in determining the width of the slit.

Figure 9: Flow channel.

Figure 10: Photomicrograph of polystyrene latex shpers.

Figure 11: Relative viscosity, μ_s/μ_f, of suspensions of polystyrene latex spheres as a function of concentration.

Figure 12: Relative viscosity, μ_s/μ_f, of suspensions of red blood cells as a function of concentration.

Figure 13: Components of the LDA system used.

Figure 14: Velocity profiles of contaminants and fluorescent tracers in water.

Figures 15-24: Plots of normalized velocity profiles $u/\underline{u}$ vs. normalized distance from the wall, x/h.

Figure Captions (Appendix II)

Figure II-1: A record of an 'acceptable' signal to the frequency counter.

Figure II-2: Autocorrelation of the signal shown in figure II-1.

Figure II-3: Fourier transform of signal shown in figure II-2.

Figure II-4: A record of a signal with high level of noise.

Figure II-5: Autocorrelation of signal shown in figure II-4.

Figure II-6: Fourier transform of figure II-5.

Figure II-7: A record of a signal recorded under identical experimental conditions to the signal in figure II-4.

Figure II-8: Autocorrelation of signal shown in figure II-7.

Figure II-9: Fourier transform of signal shown in figure II-7.

Figure Captions

Appendix III

Figure III-1: Transmittance curve of customized Oriel filter.

Figure III-2: Transmittance curve of a combination of two Oriel filters.

Figure III-3: Transmittance curve of a combination of two Oriel filters and a number 12 filter.

Appendix IV

Figure IV-1: Bursts of Doppler signal.

Figure IV-2: Operating principle of frequency counter.

Figure IV-3: Scheme for burst counting.

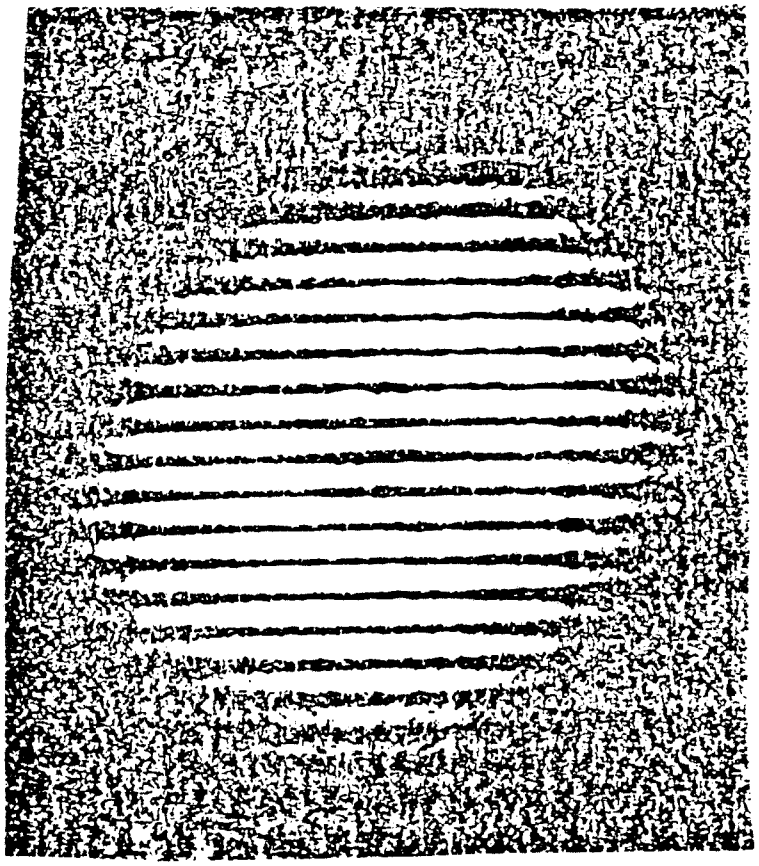

Fig.1: Projected Interference Fringe Pattern

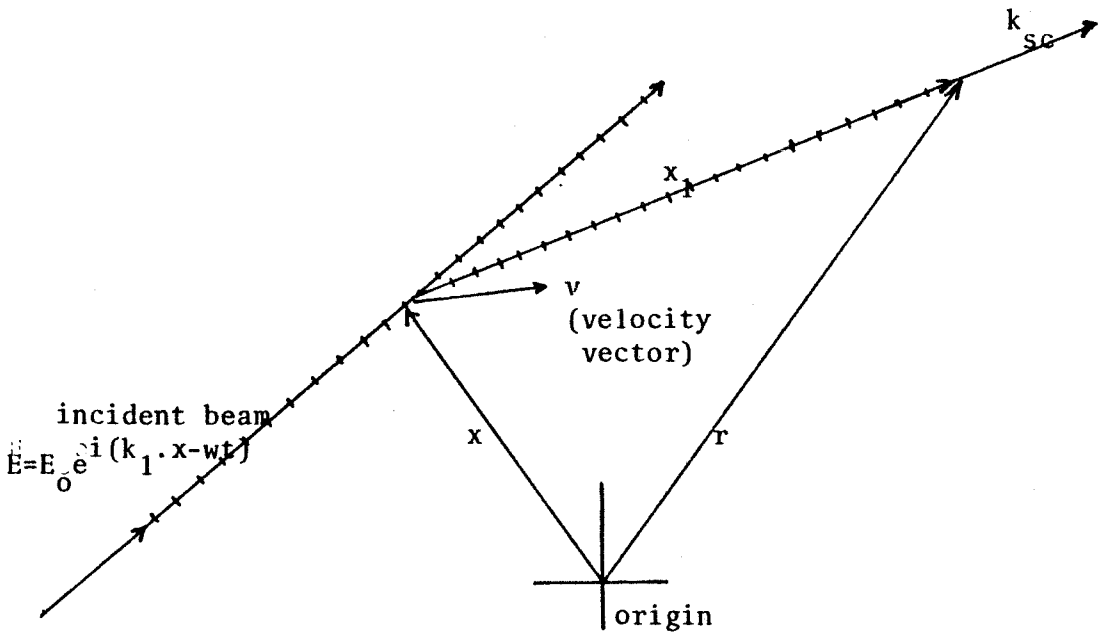

Fig.2: Scattering from a small particle

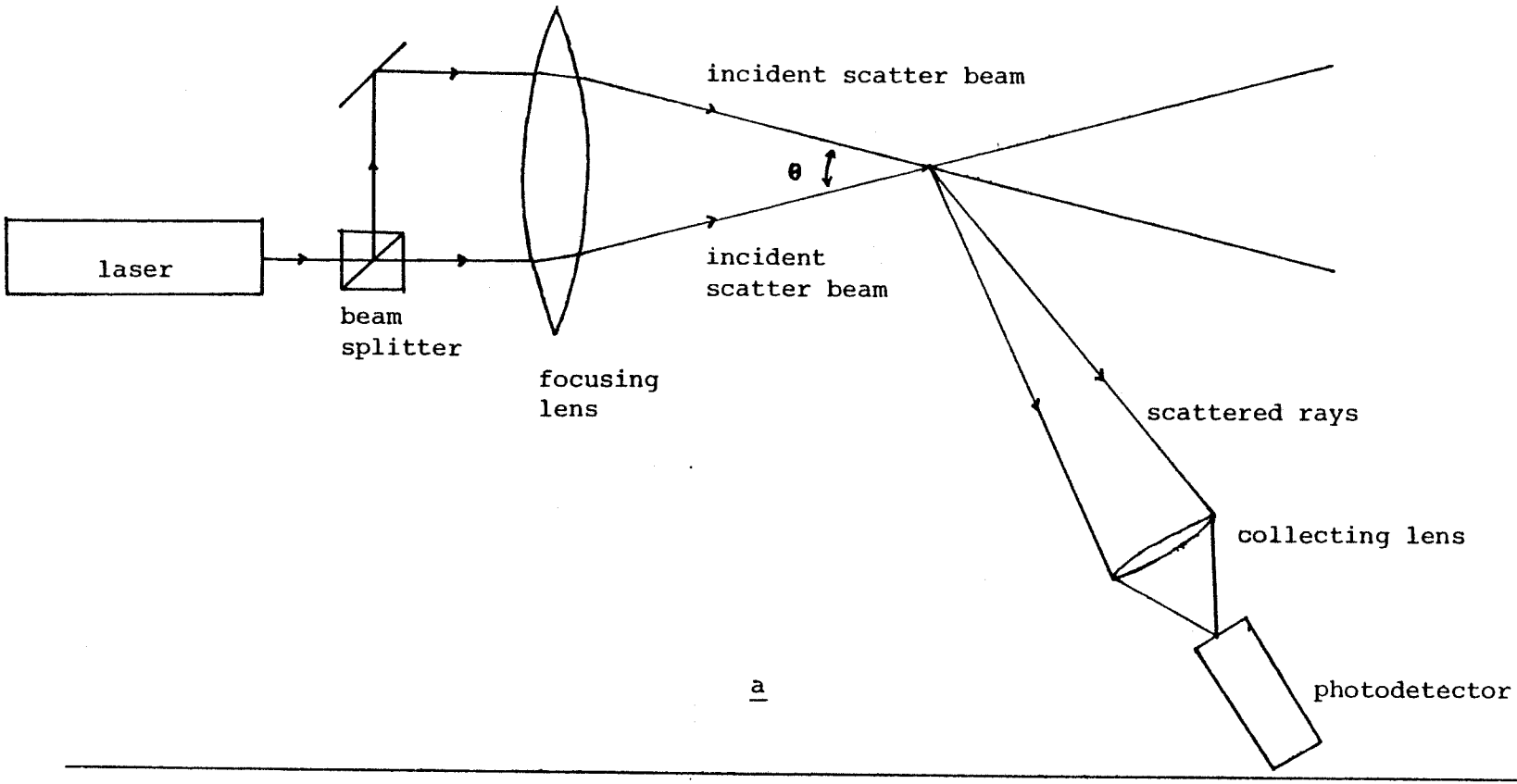

a

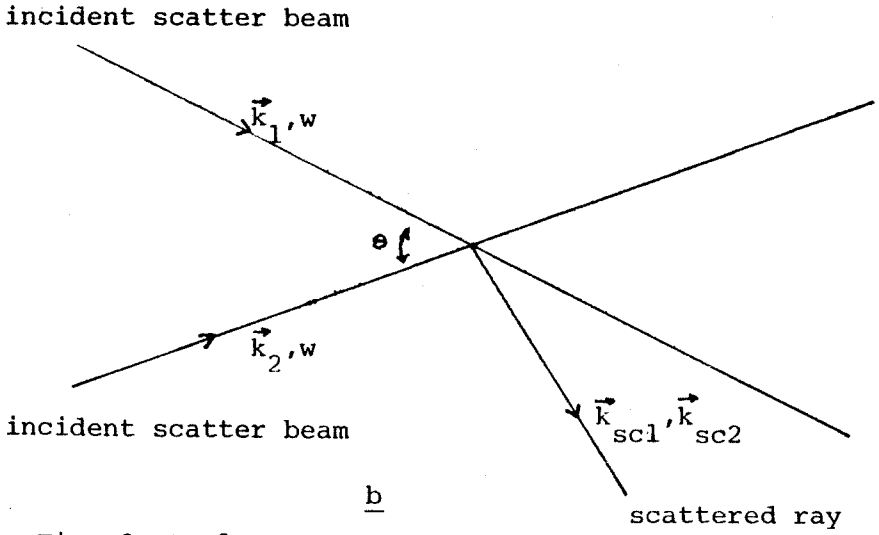

b

Fig. 3: Dual scatter system

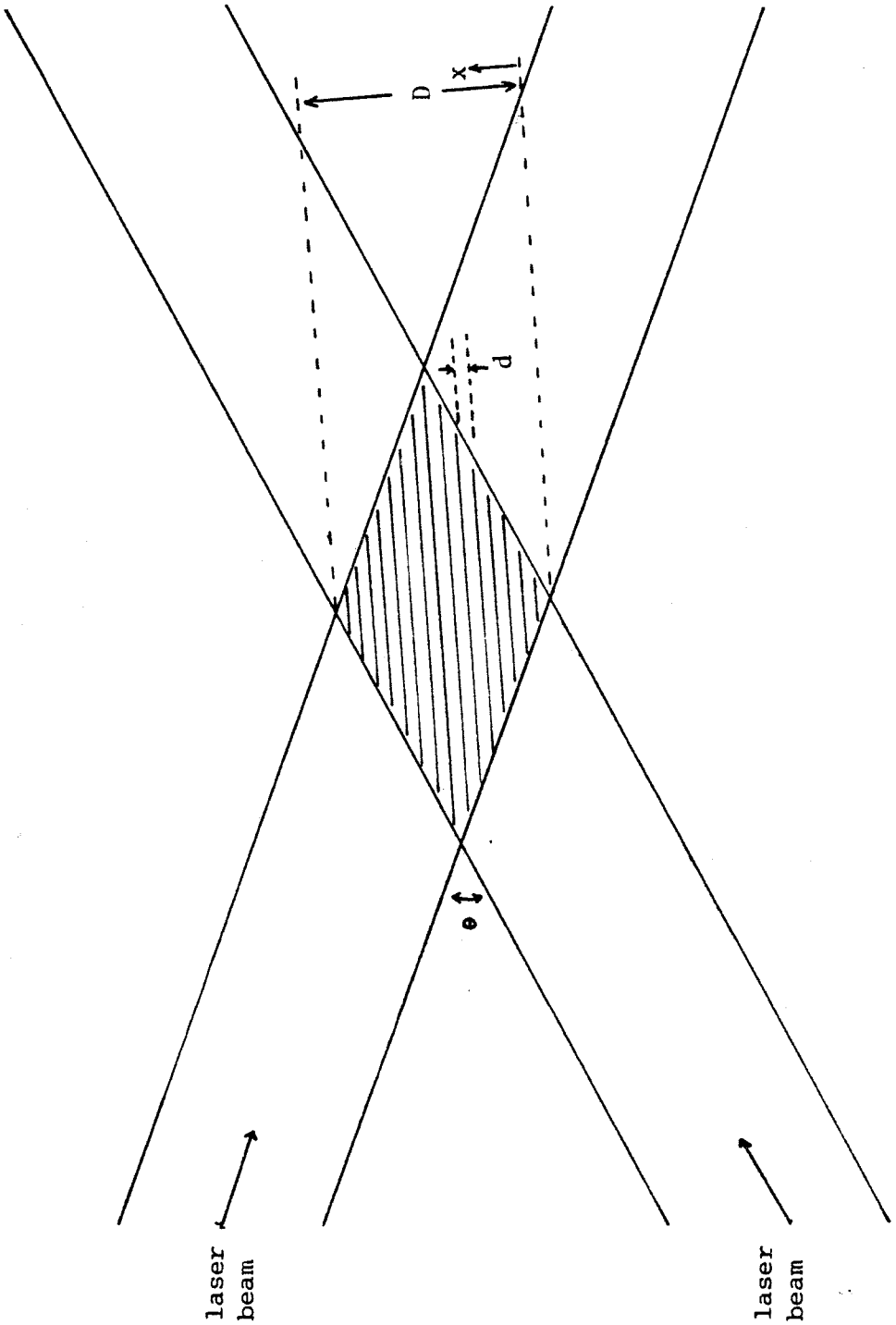

Fig. 4: Fringe pattern

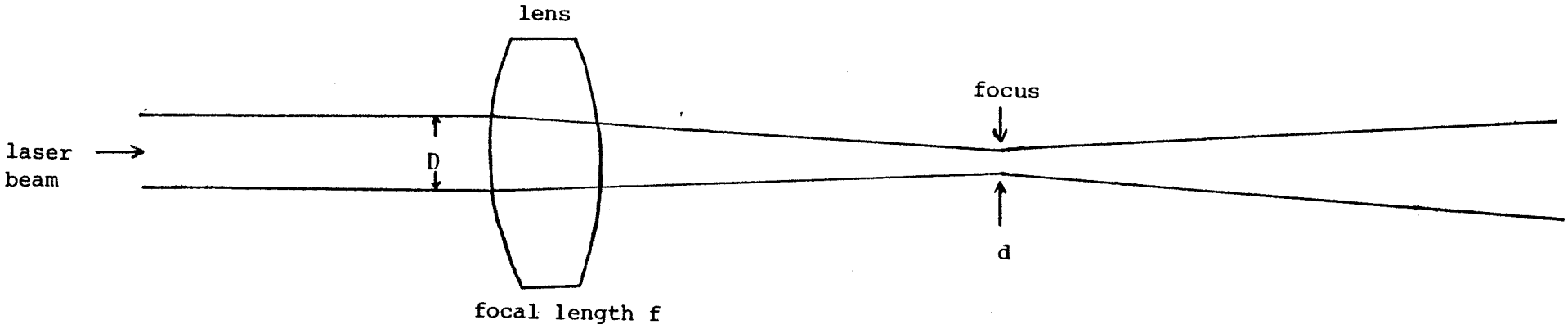

$d \propto f/D$

Fig. 5

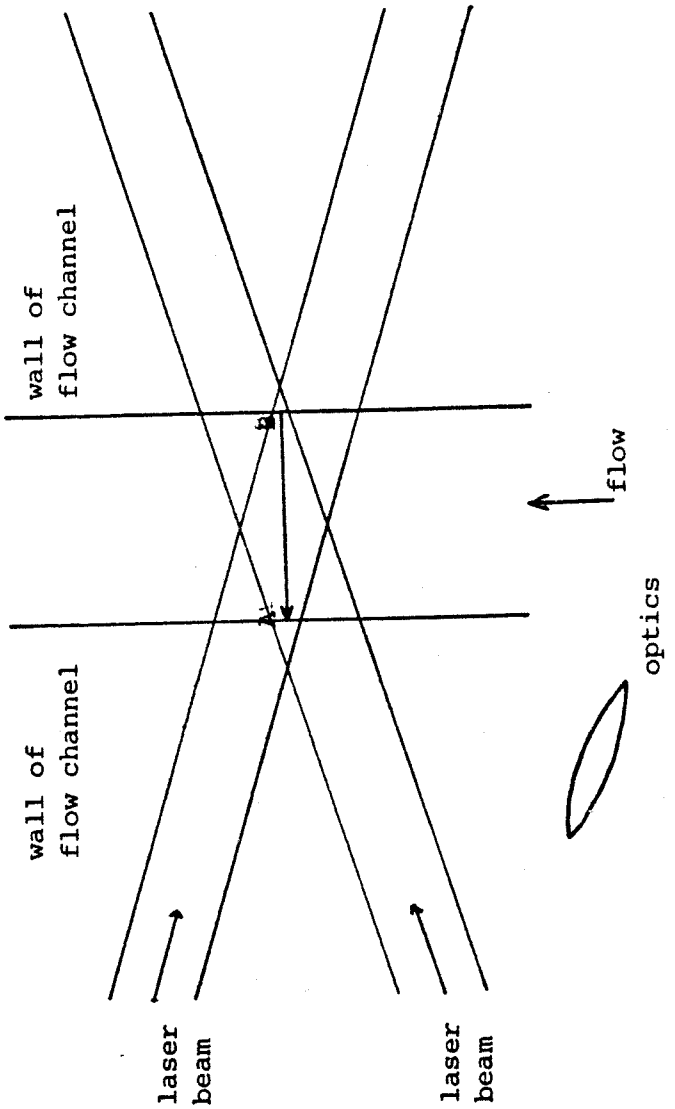

Fig. 6: Modified LDA system

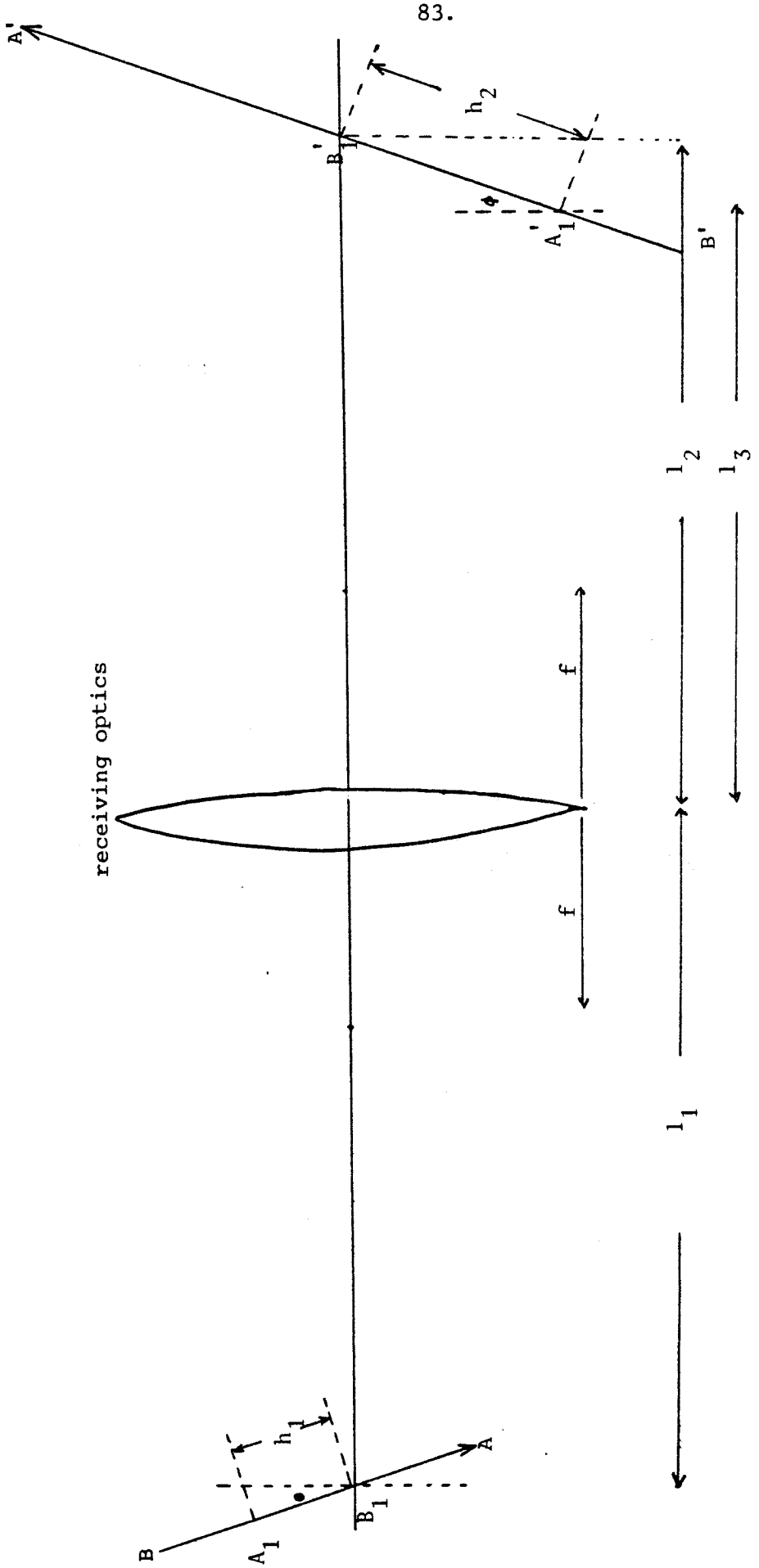

Fig. 7

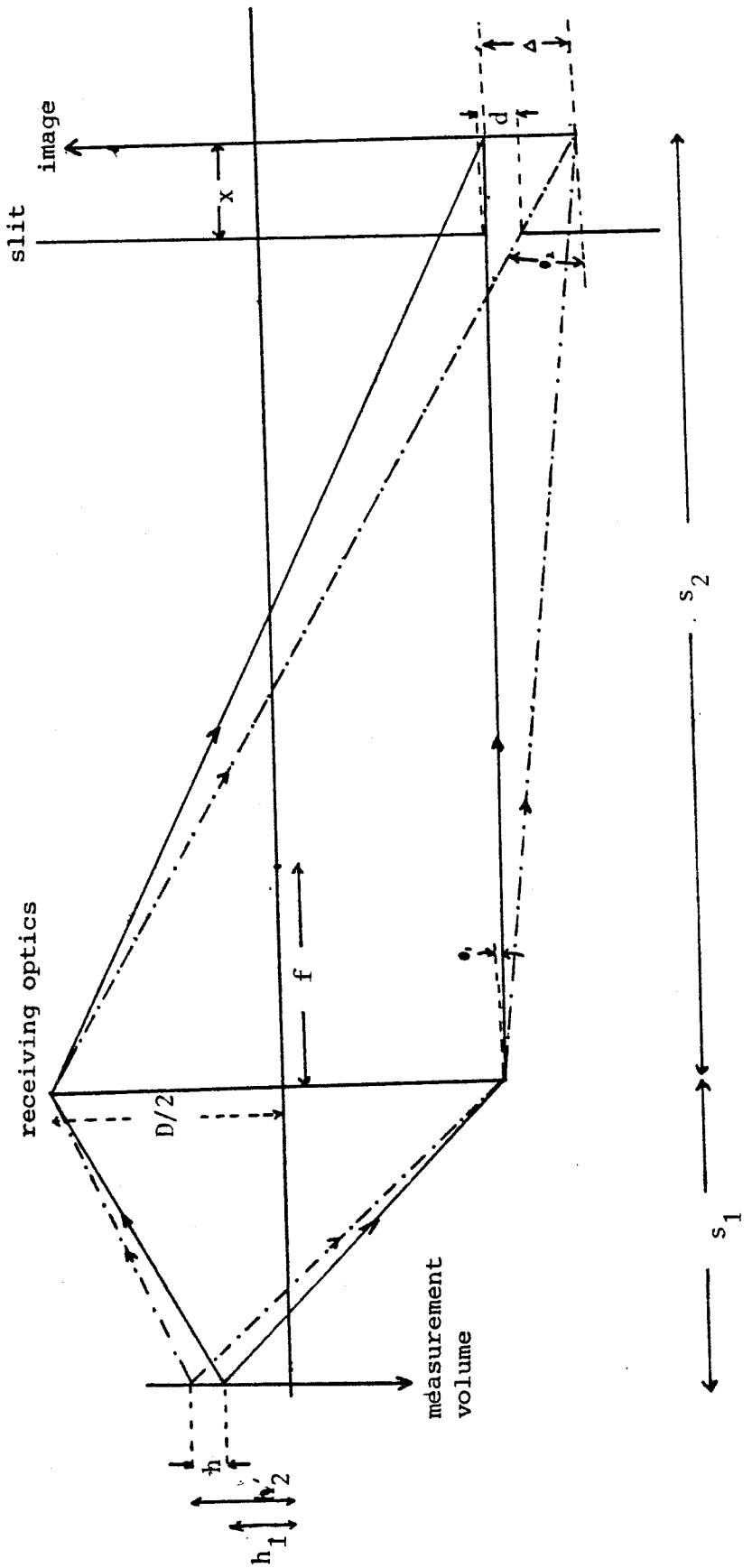
slit
image
x
d
Δ
receiving optics
D/2
f
measurement volume
h
h1
h2
s1
s2

Fig. 8

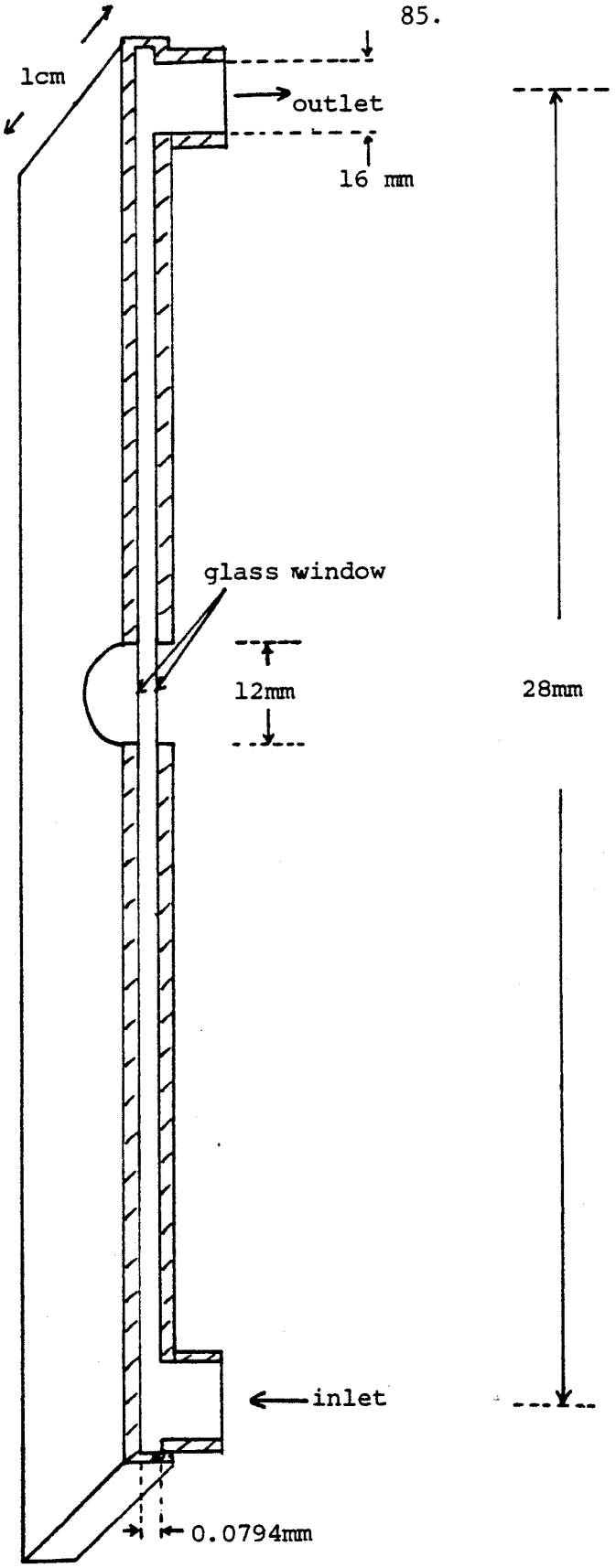

Fig. 9: Flow channel (cut through longitudinal axis -diagram not to scale)

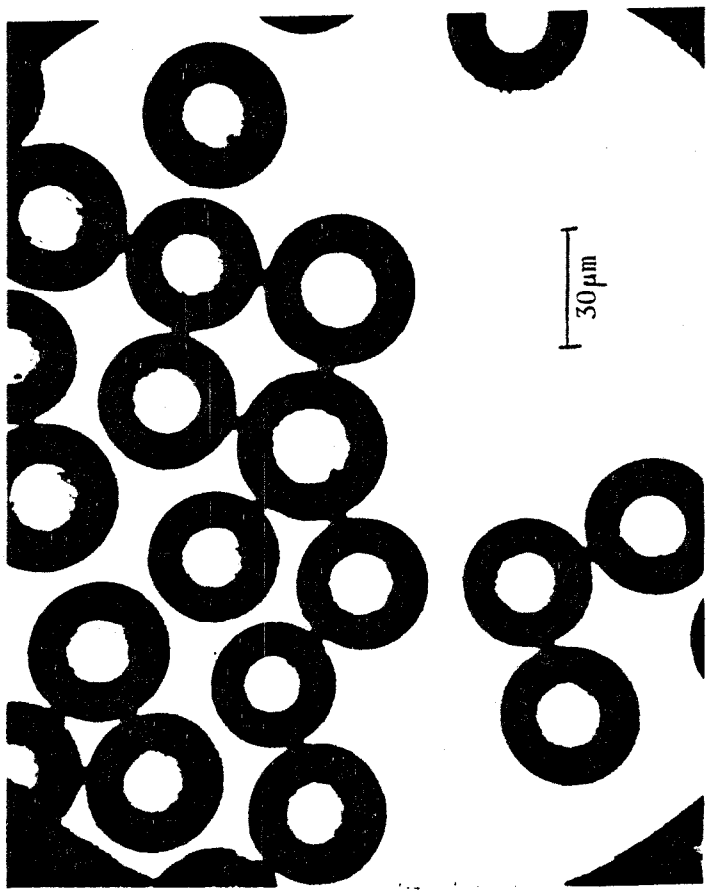

Fig. 10: Polystyrene Latex Spheres

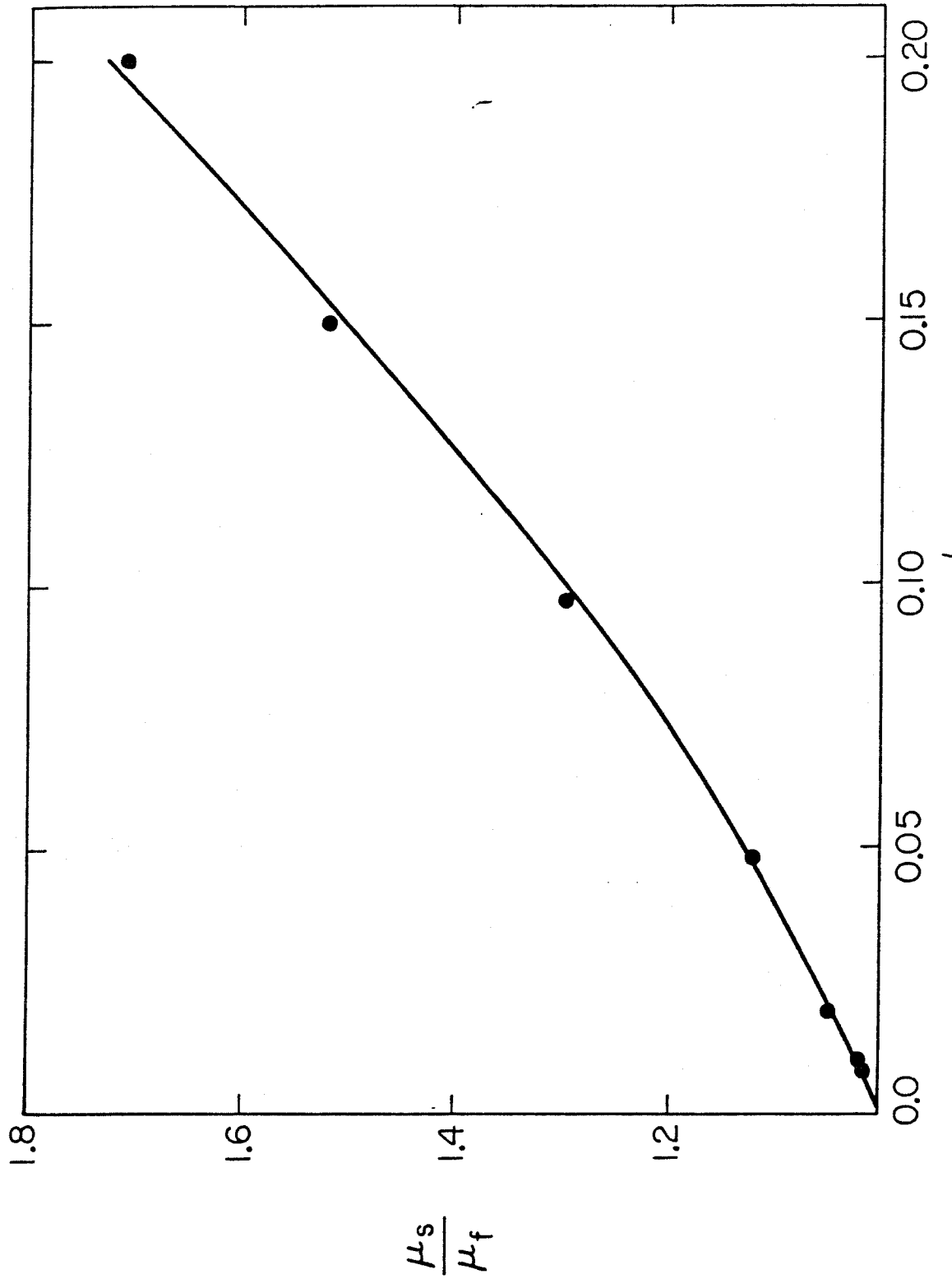

Figure 11: Relative viscosity, μ_s/μ_f, of suspensions of polystyrene latex spheres as a function of concentration.

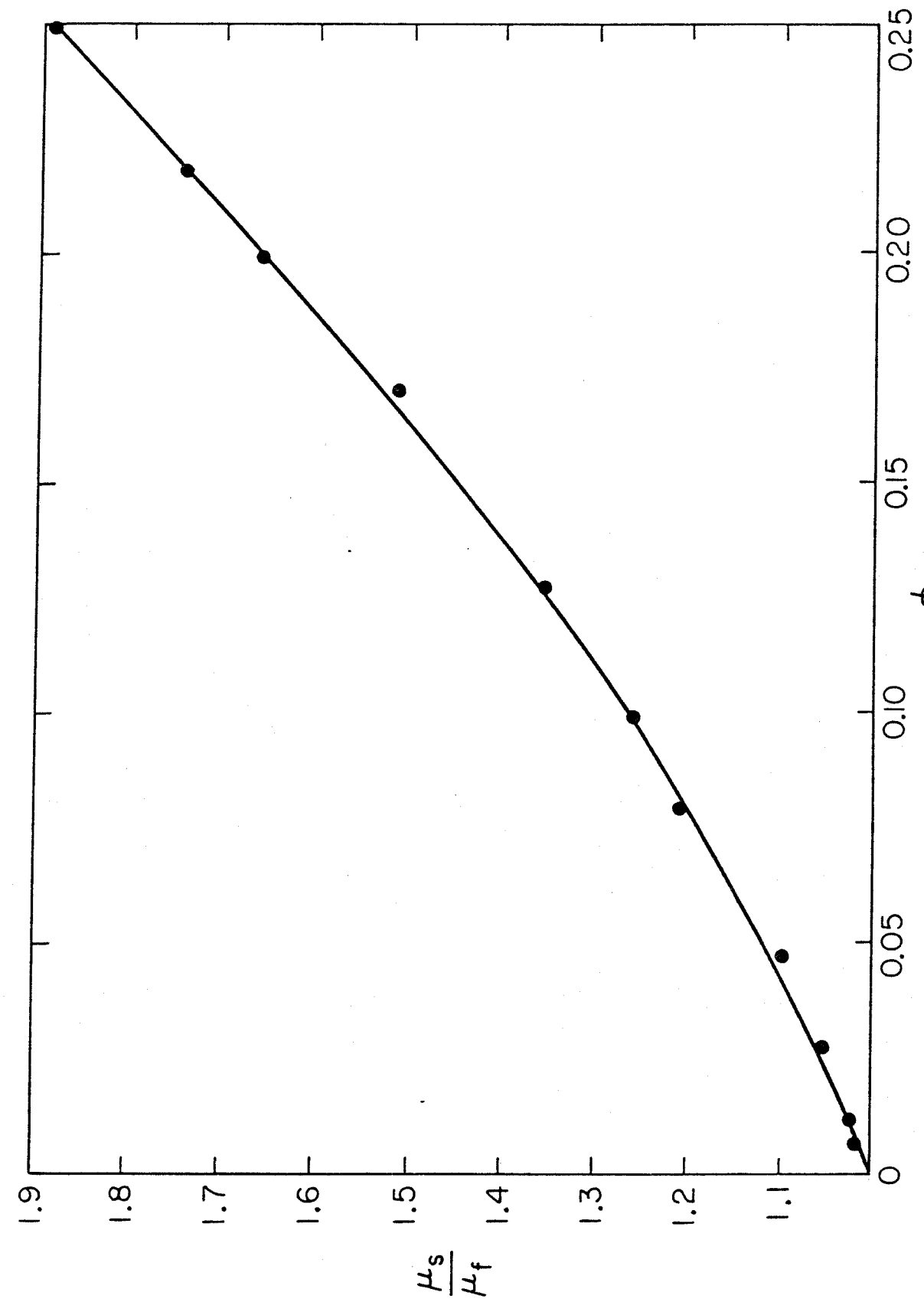

Figure 12: Relative viscosity, μ_s/μ_f, of suspensions of red blood cells as a function of concentration.

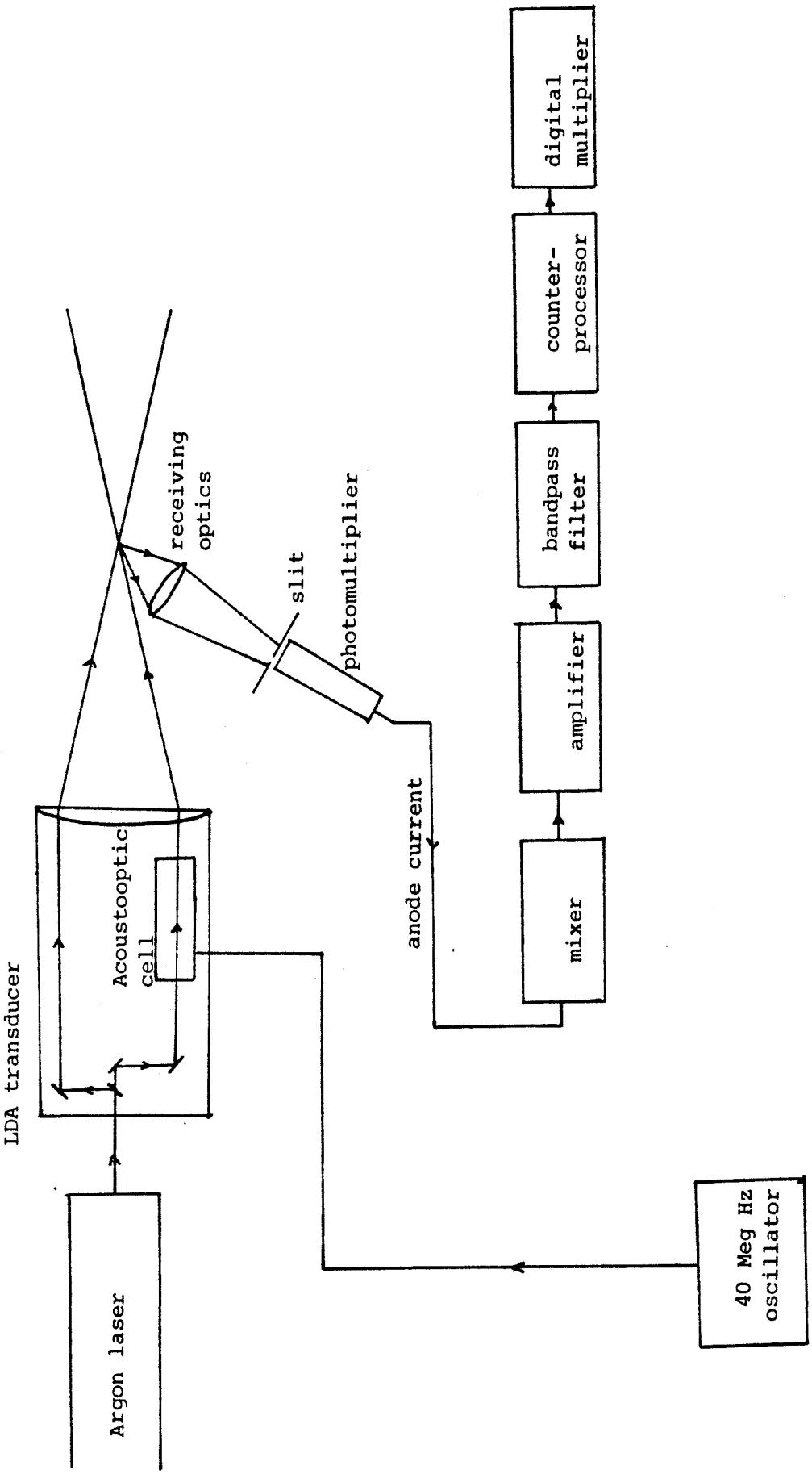

Fig. 13: LDA system

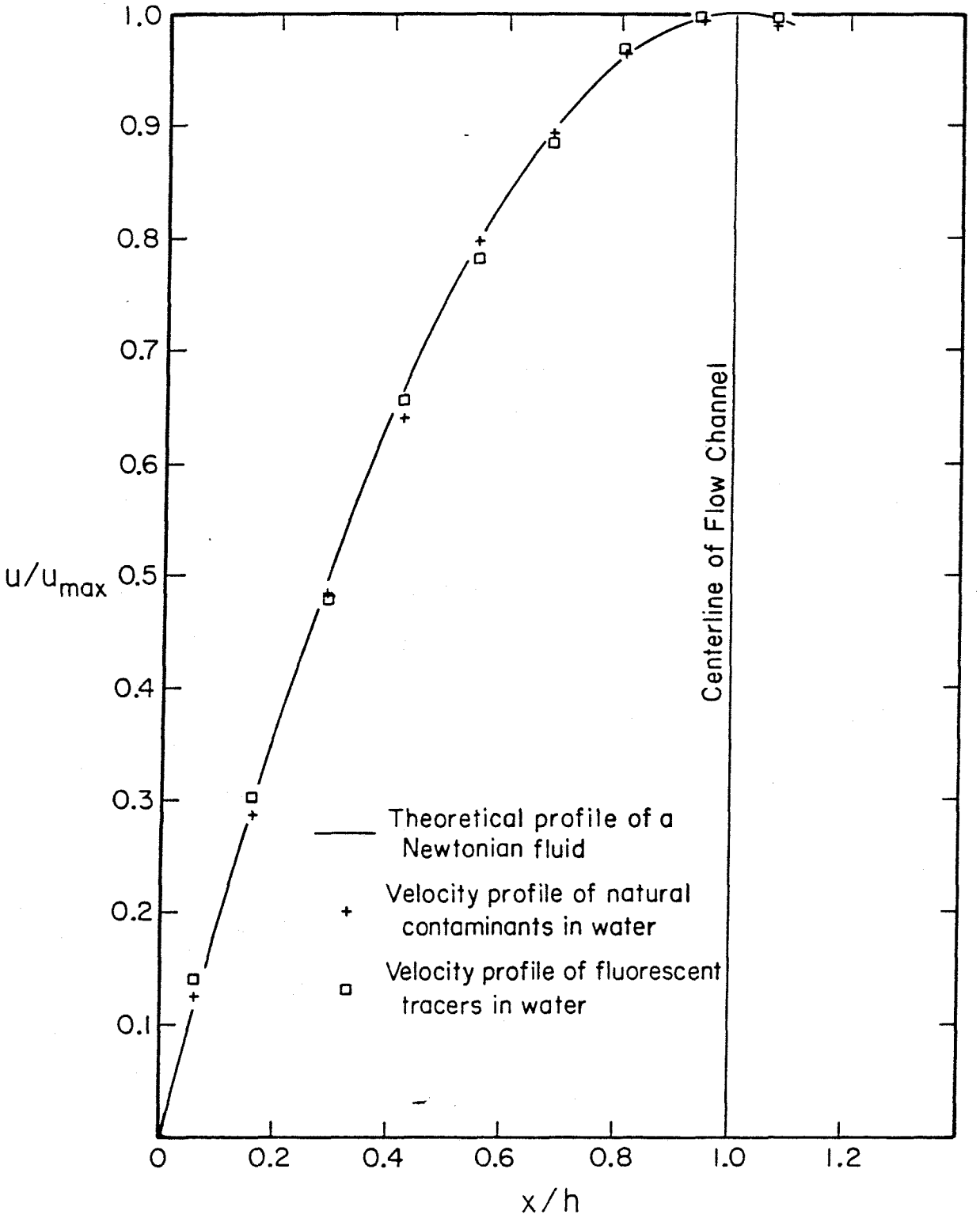

Figure 14: Velocity profiles of contaminants and fluorescent tracers in water.

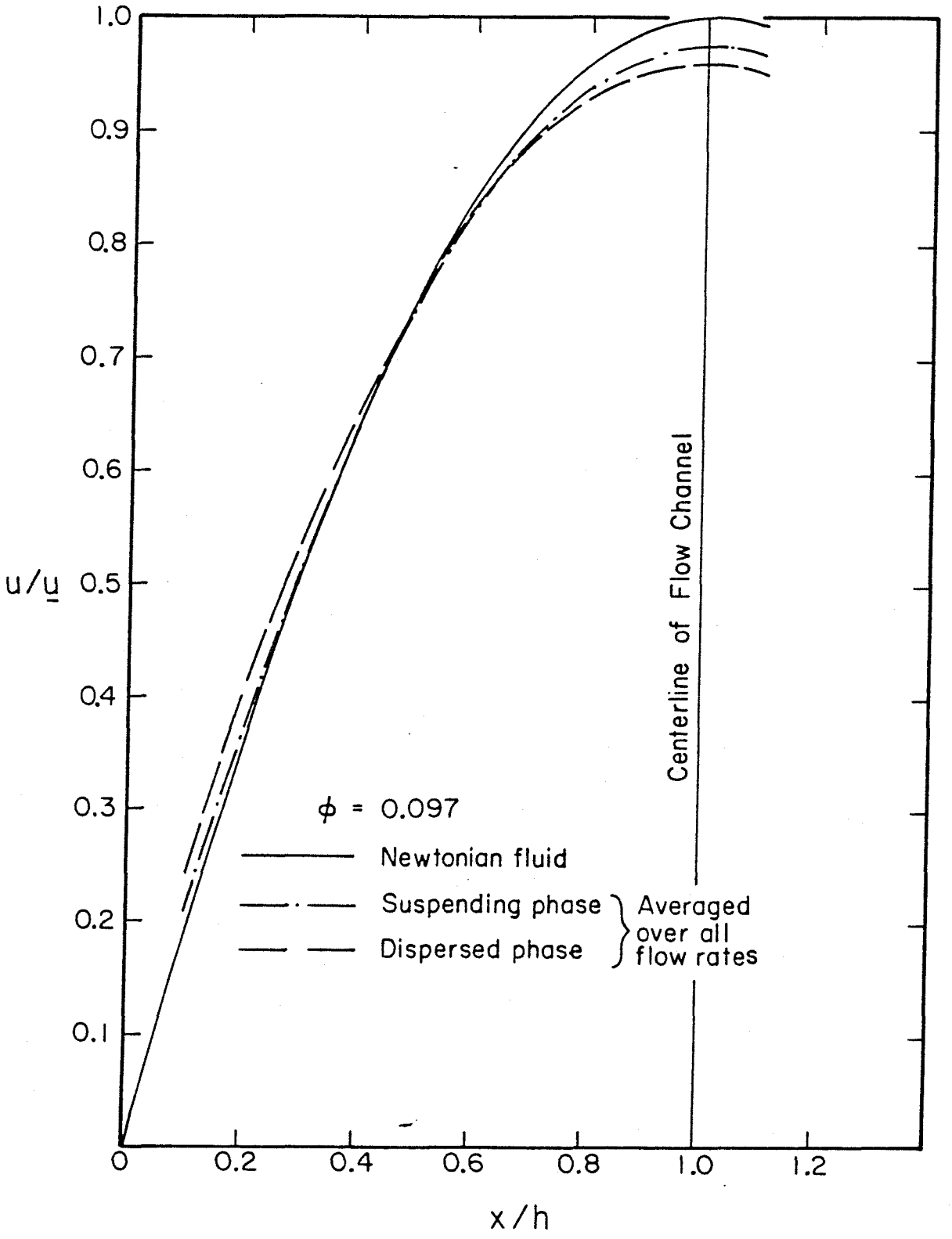

Figure 15: Normalized velocity profiles of suspension of polystyrene latex spheres.

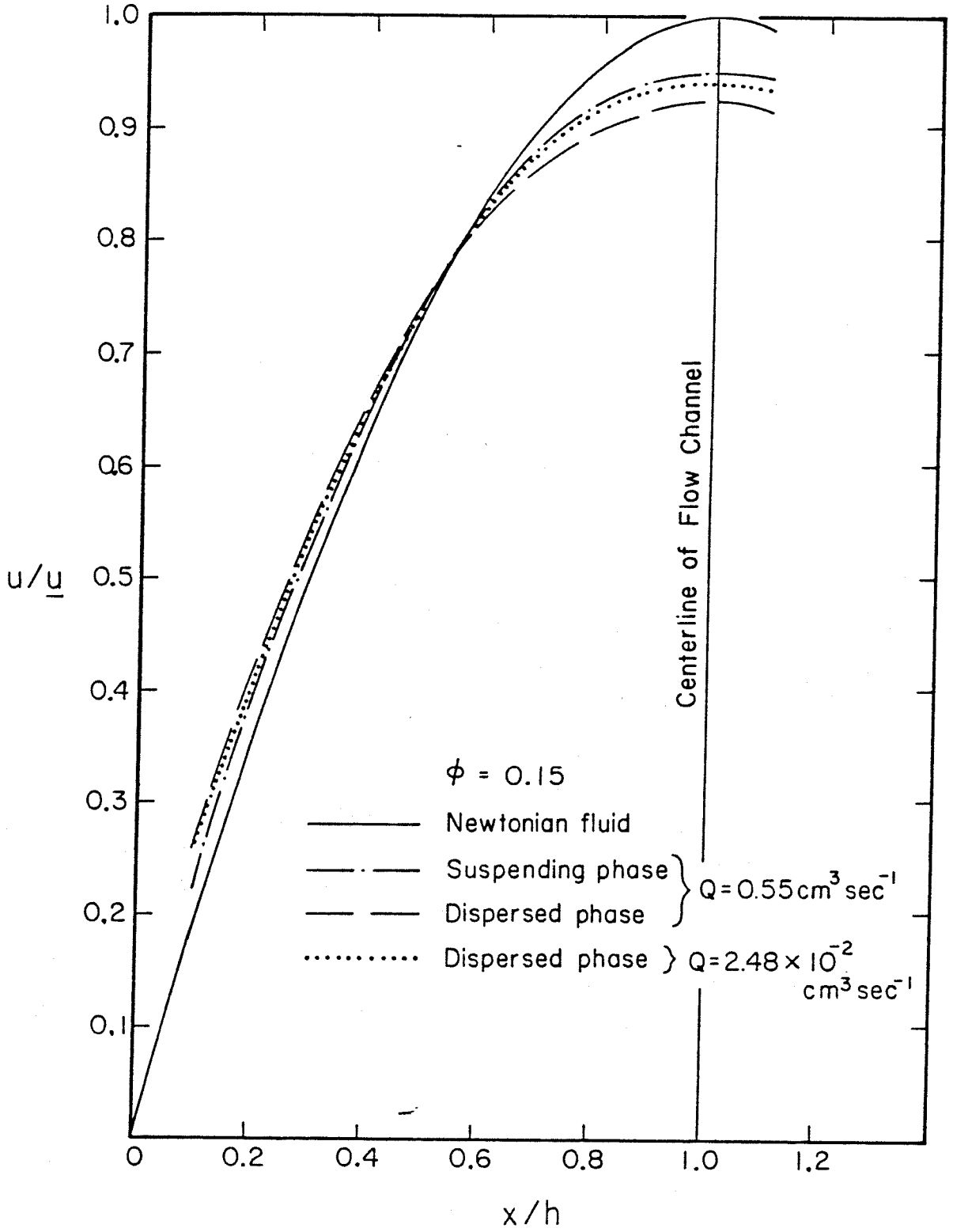

Figure 16: Normalized velocity profiles of suspension of polystyrene latex spheres.

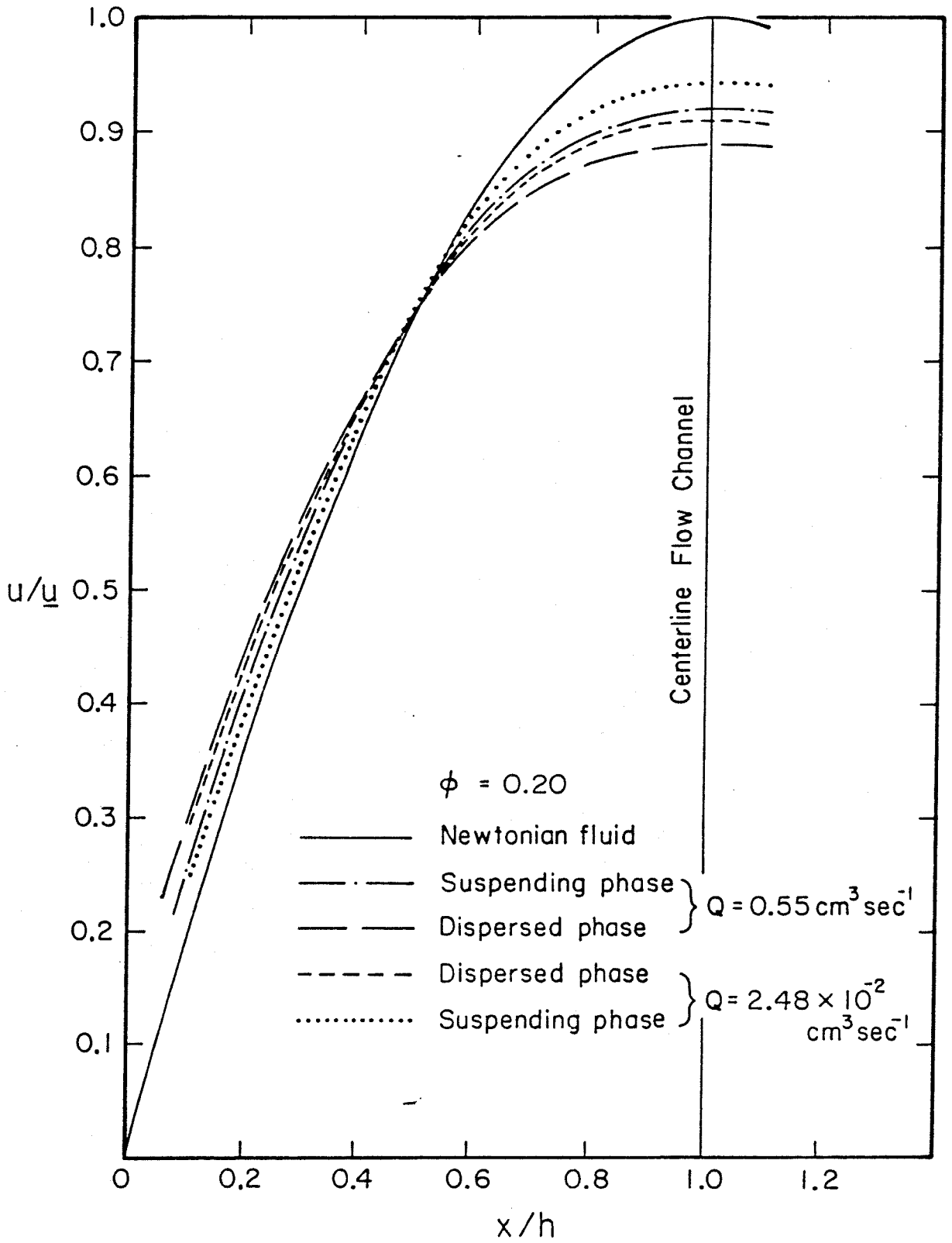

Figure 17: Normalized velocity profiles of suspension of polystyrene latex spheres.

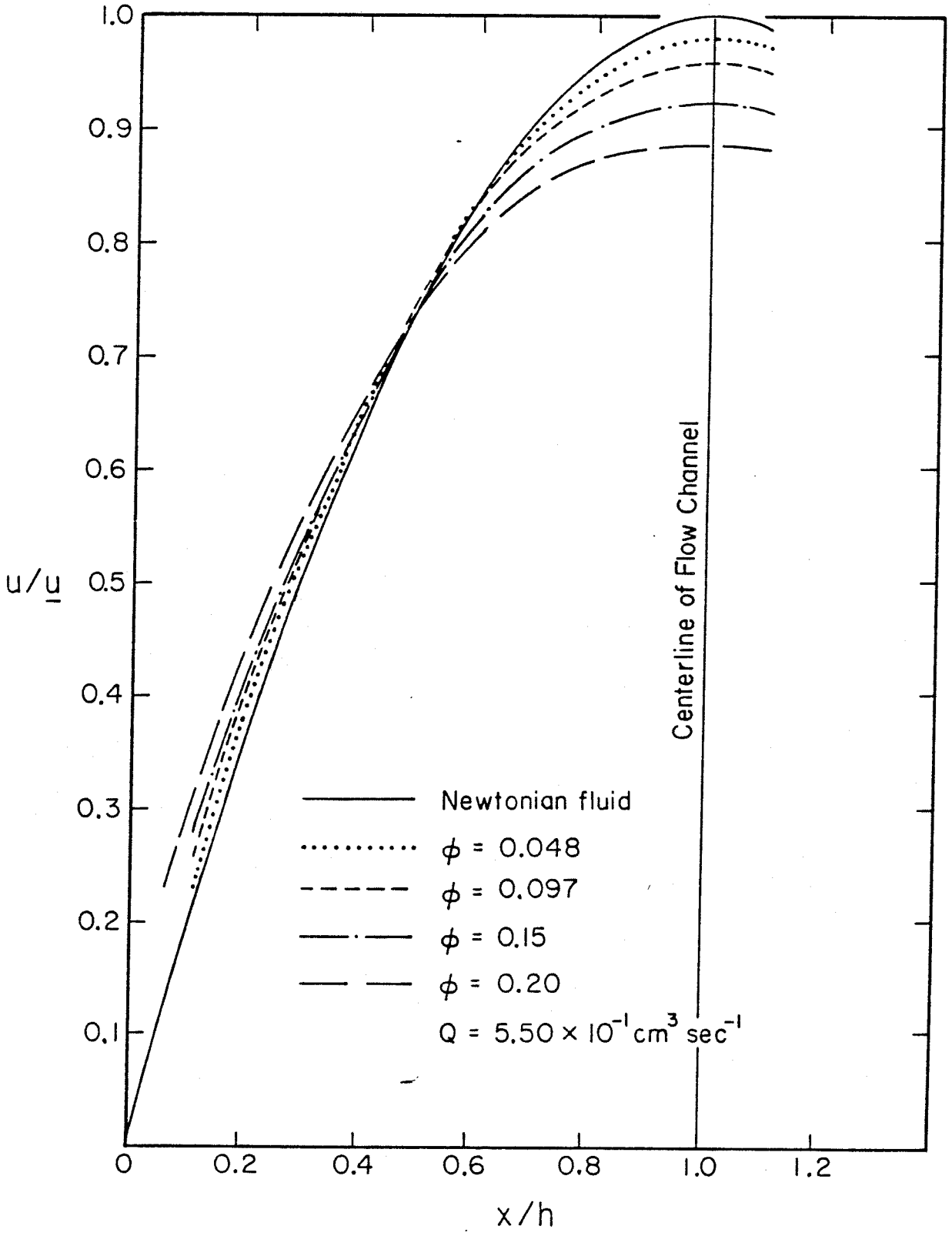

Figure 18: Normalized velocity profiles of the dispersed phases of suspensions of polystyrene latex spheres.

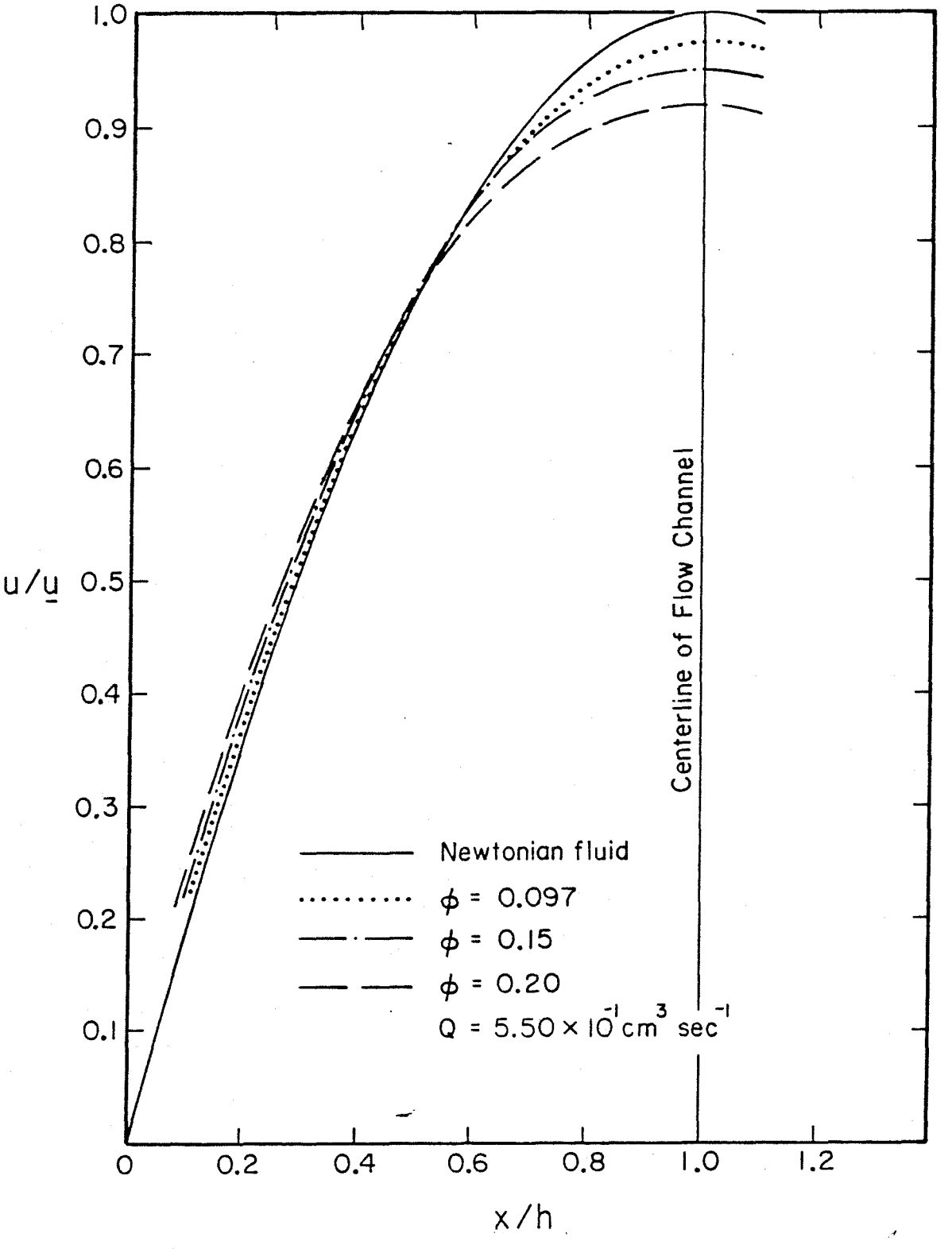

Figure 19: Normalized velocity profiles of the suspending phases of suspensions of polystyrene latex spheres.

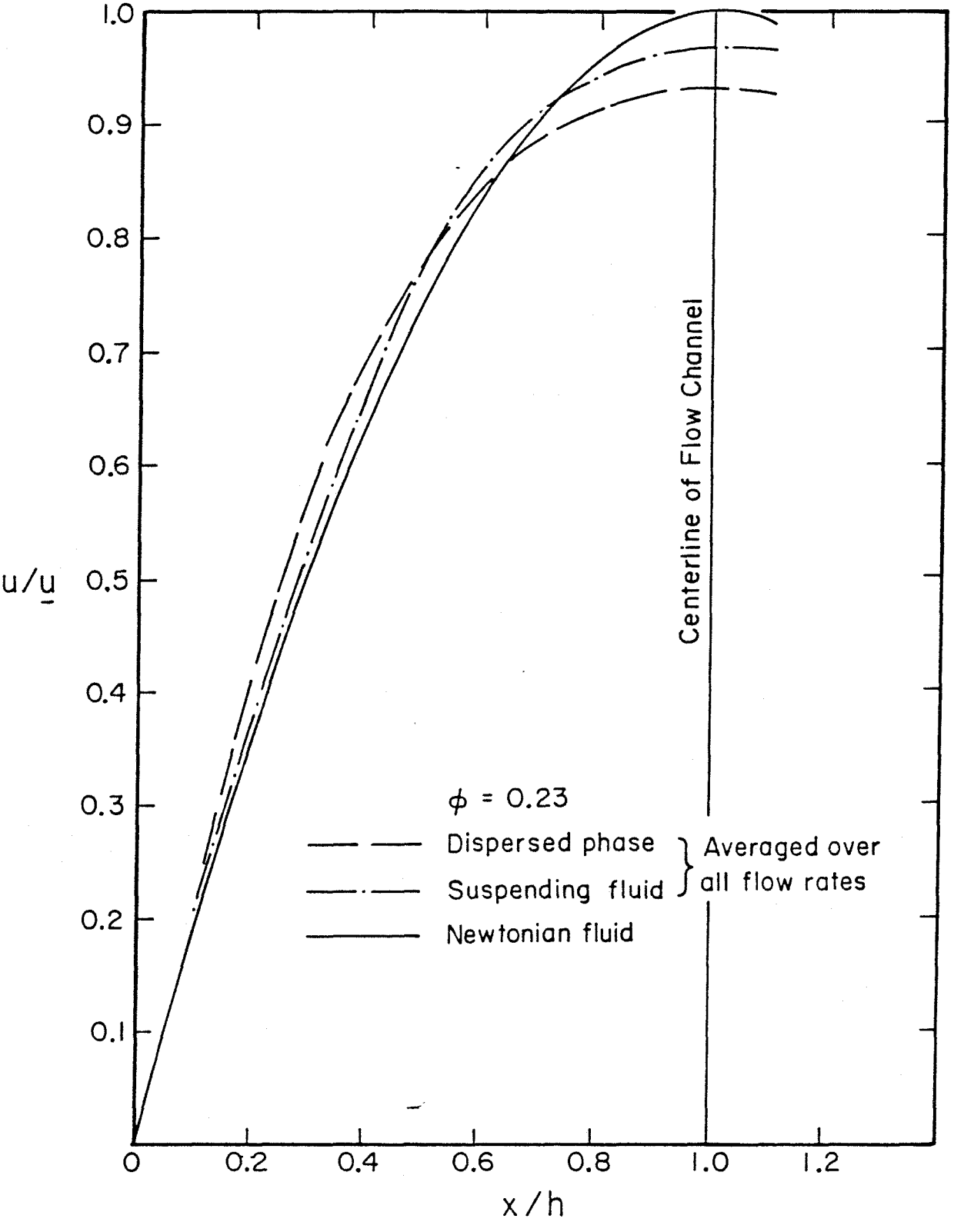

Figure 20: Normalized velocity profiles of ghost cell suspensions.

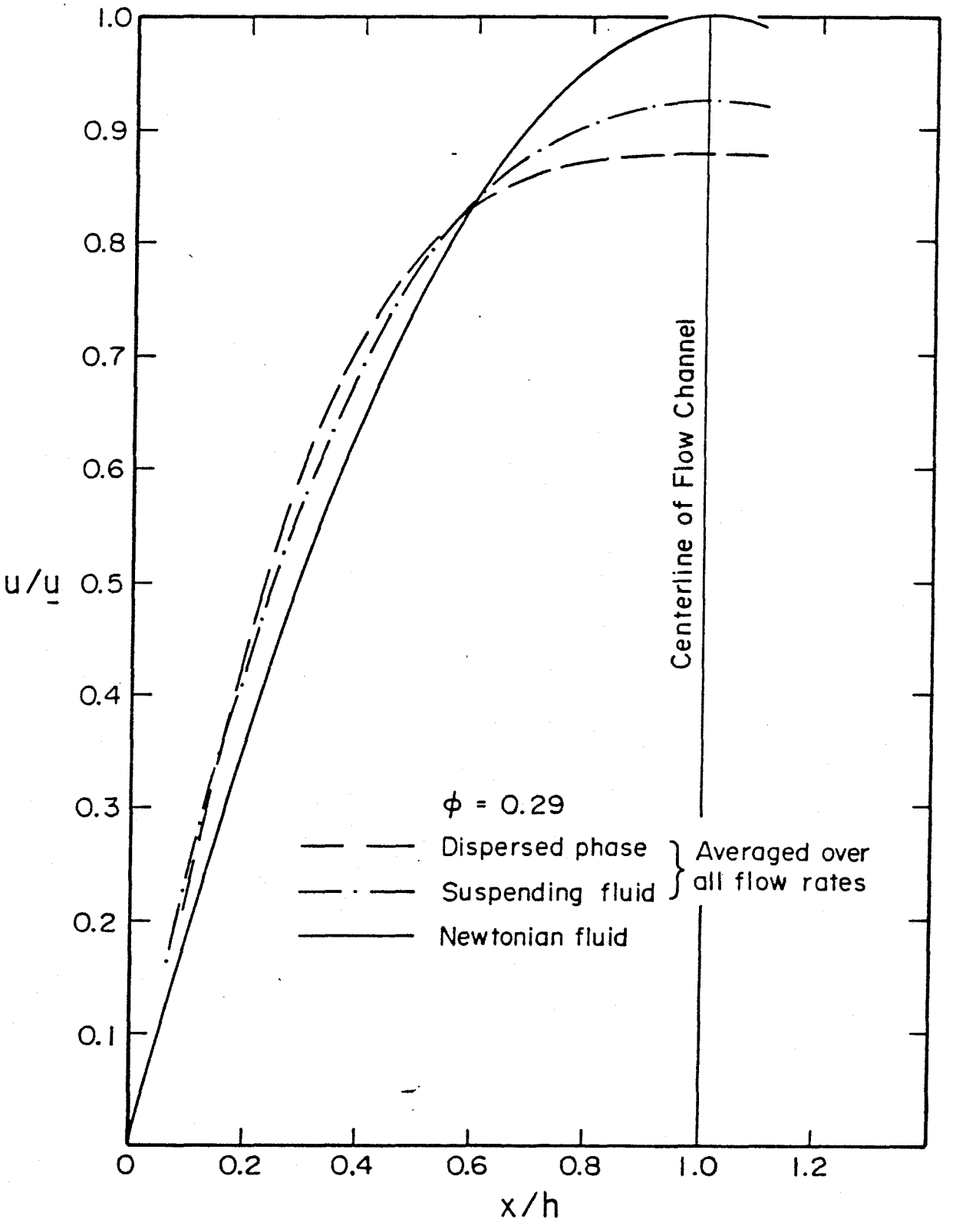

Figure 21: Normalized velocity profiles of ghost cell suspensions.

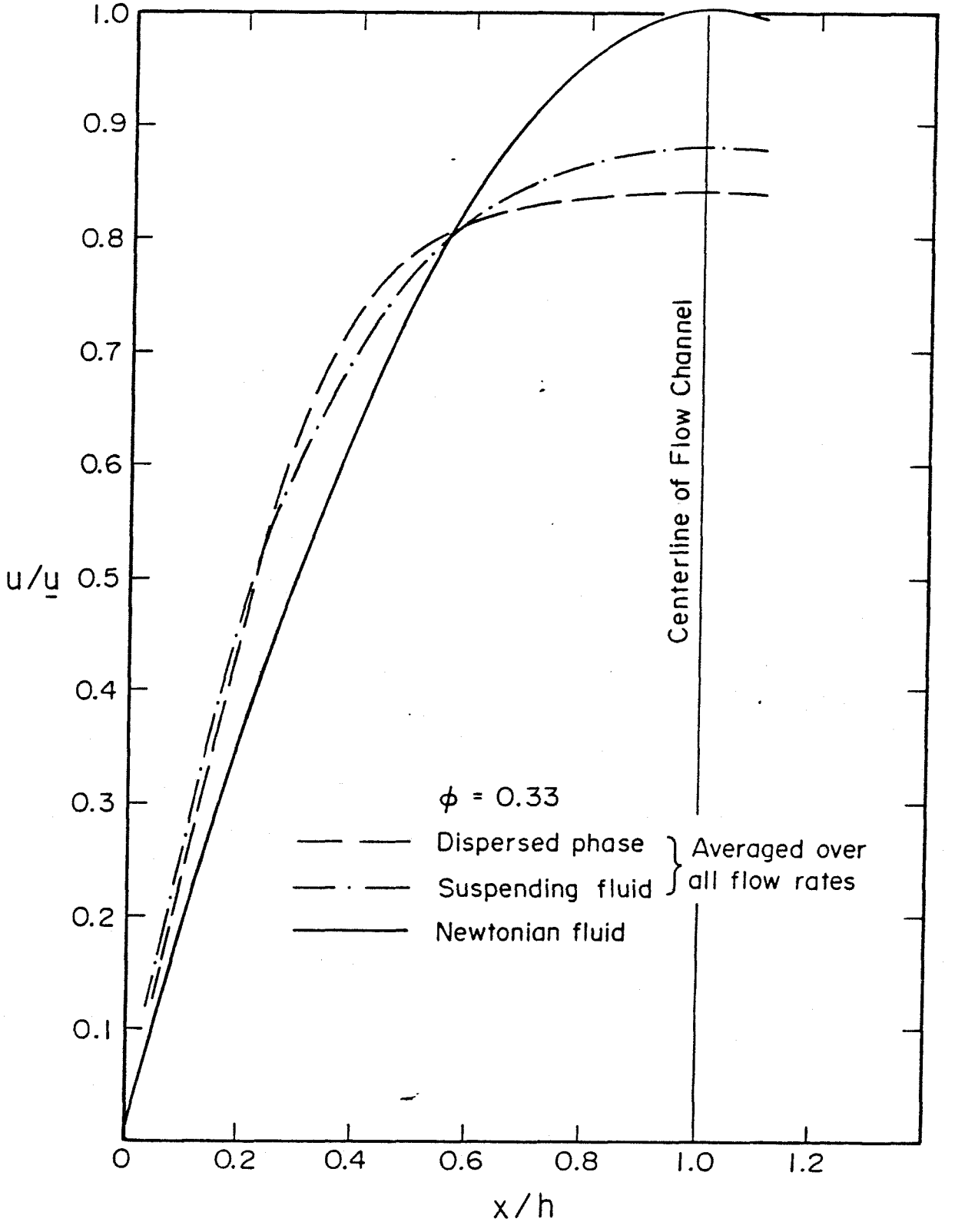

Figure 22: Normalized velocity profiles of ghost cell suspensions.

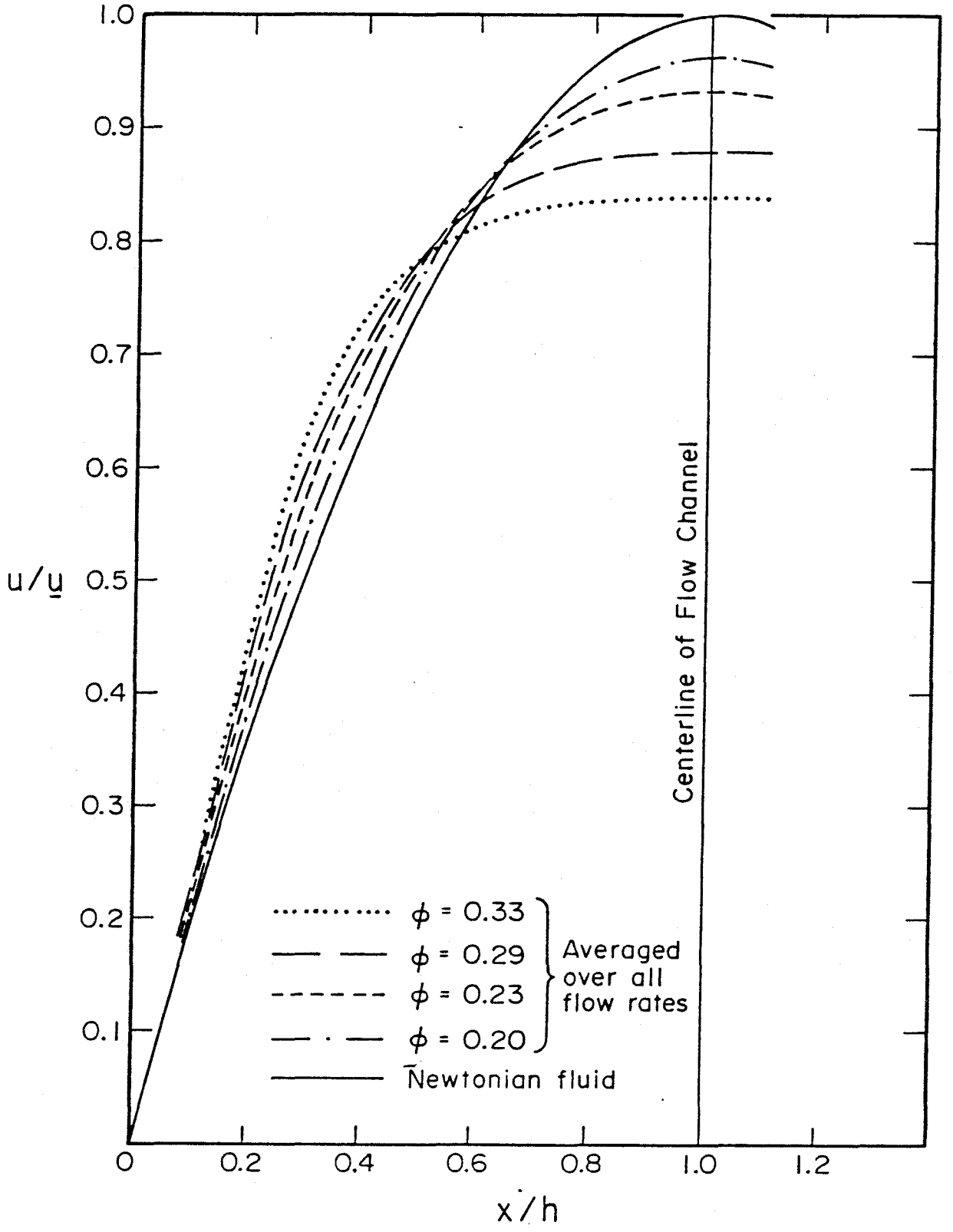

Figure 23: Normalized velocity of the dispersed phases of ghost cell suspensions.

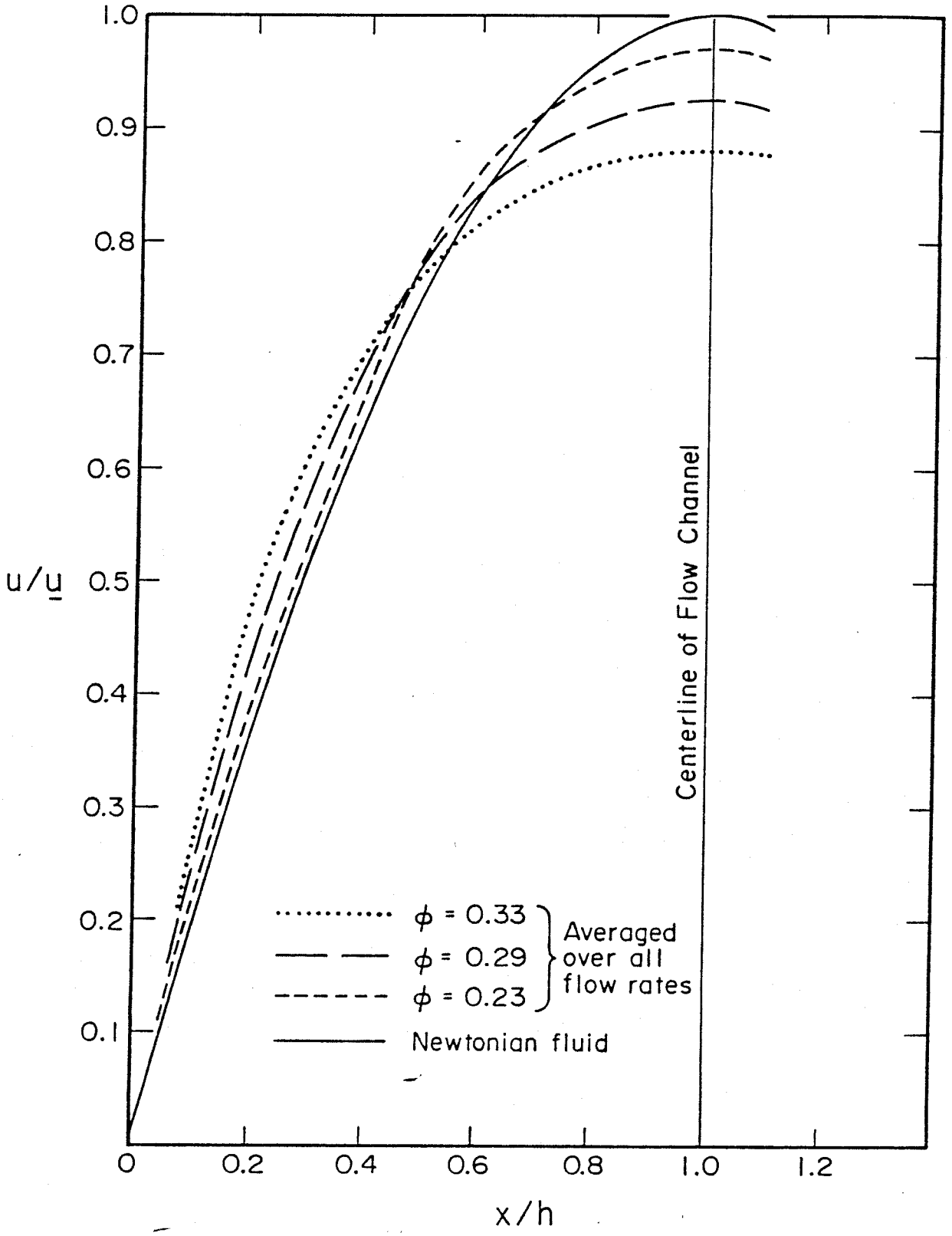

Figure 24: Normalized velocity of the suspending phases of ghost cell suspensions.

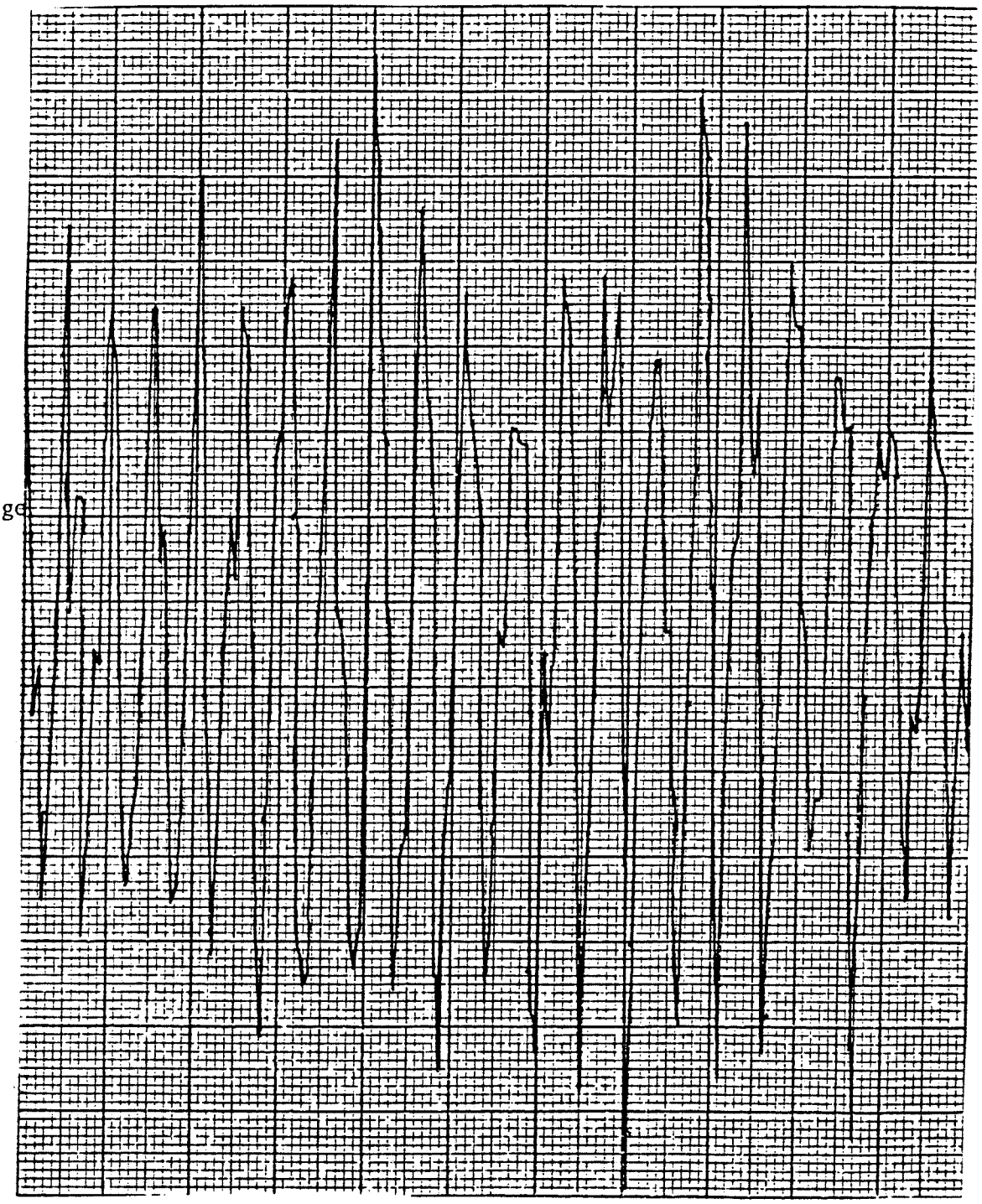

Fig. II-1

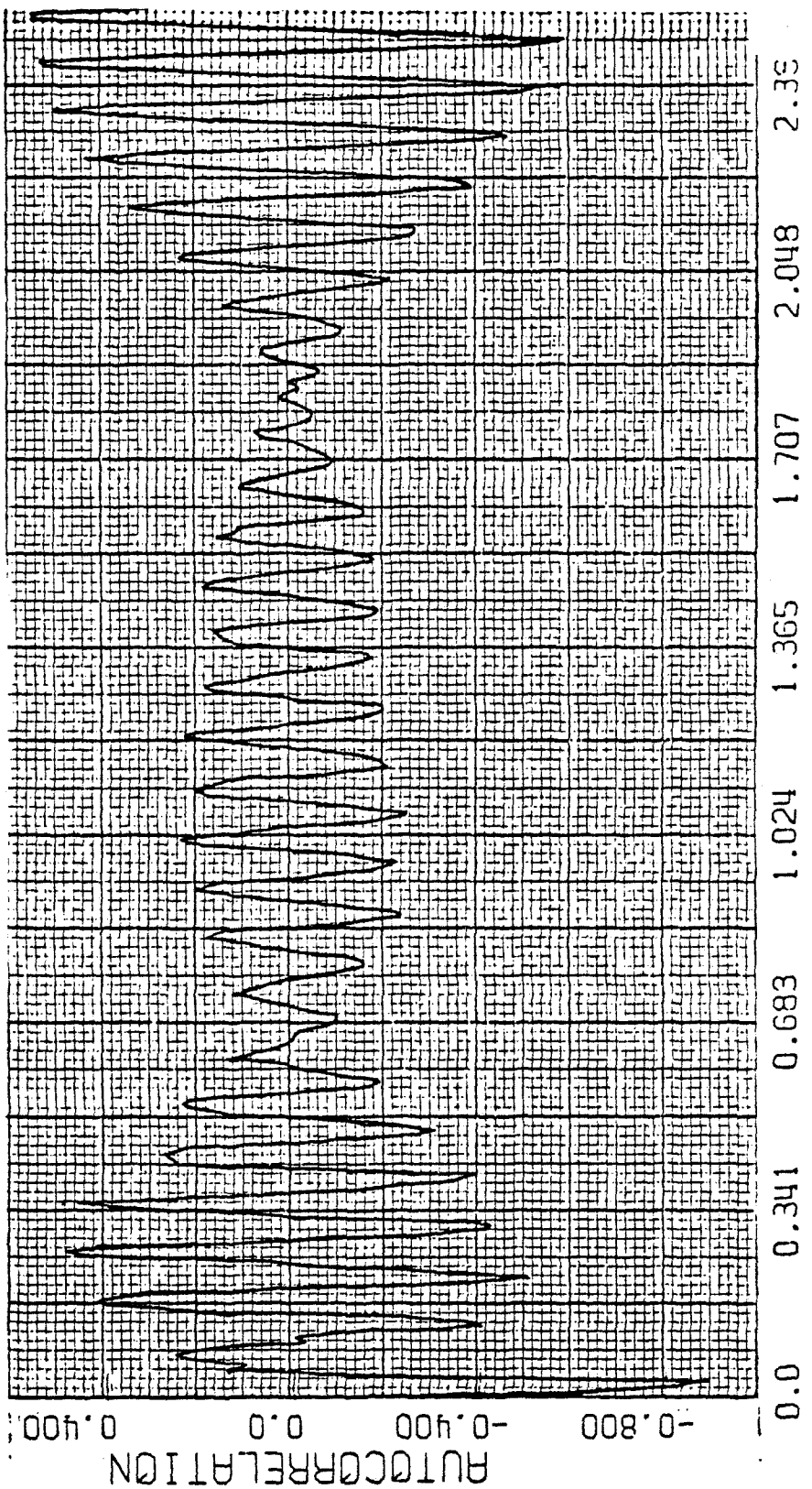
AUTOCORRELATION
0.400
0.0
-0.400
-0.800
0.0
0.341
0.683
1.024
1.365
1.707
2.048
2.39
Lag Time

Fig. II-2

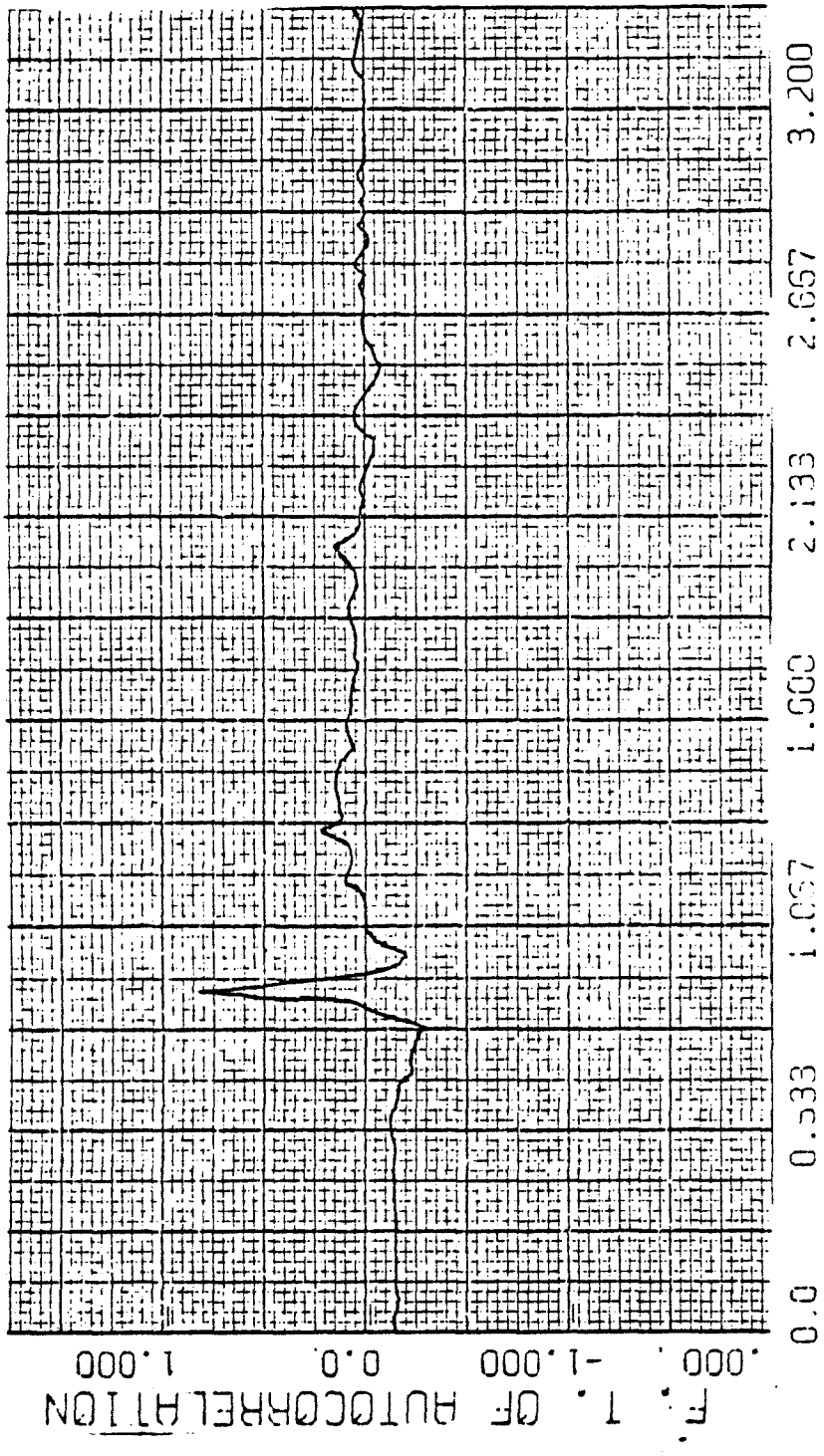

Frequency ($x10^{-4}$Hz)

Fig. II-3

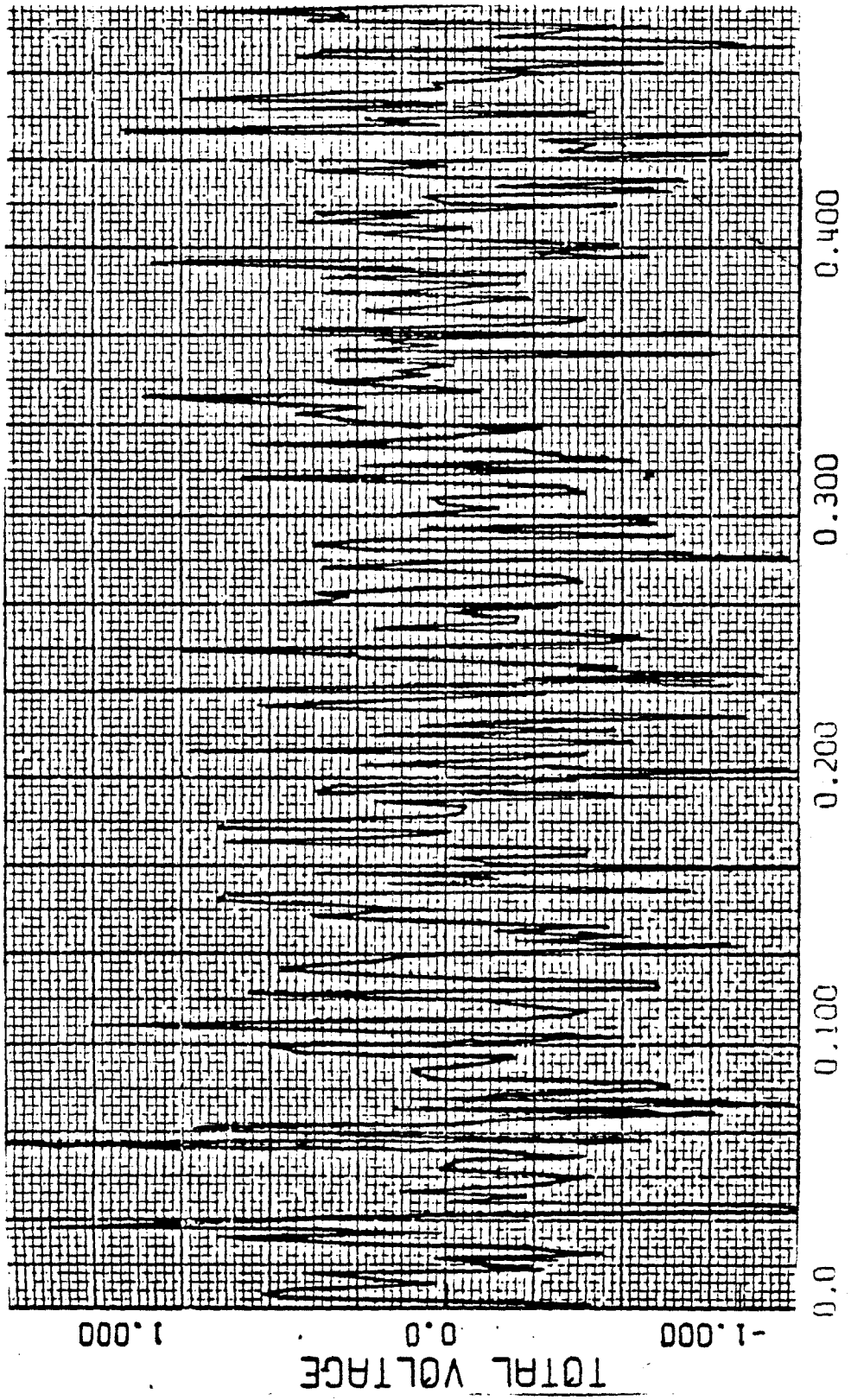

Fig. II-4

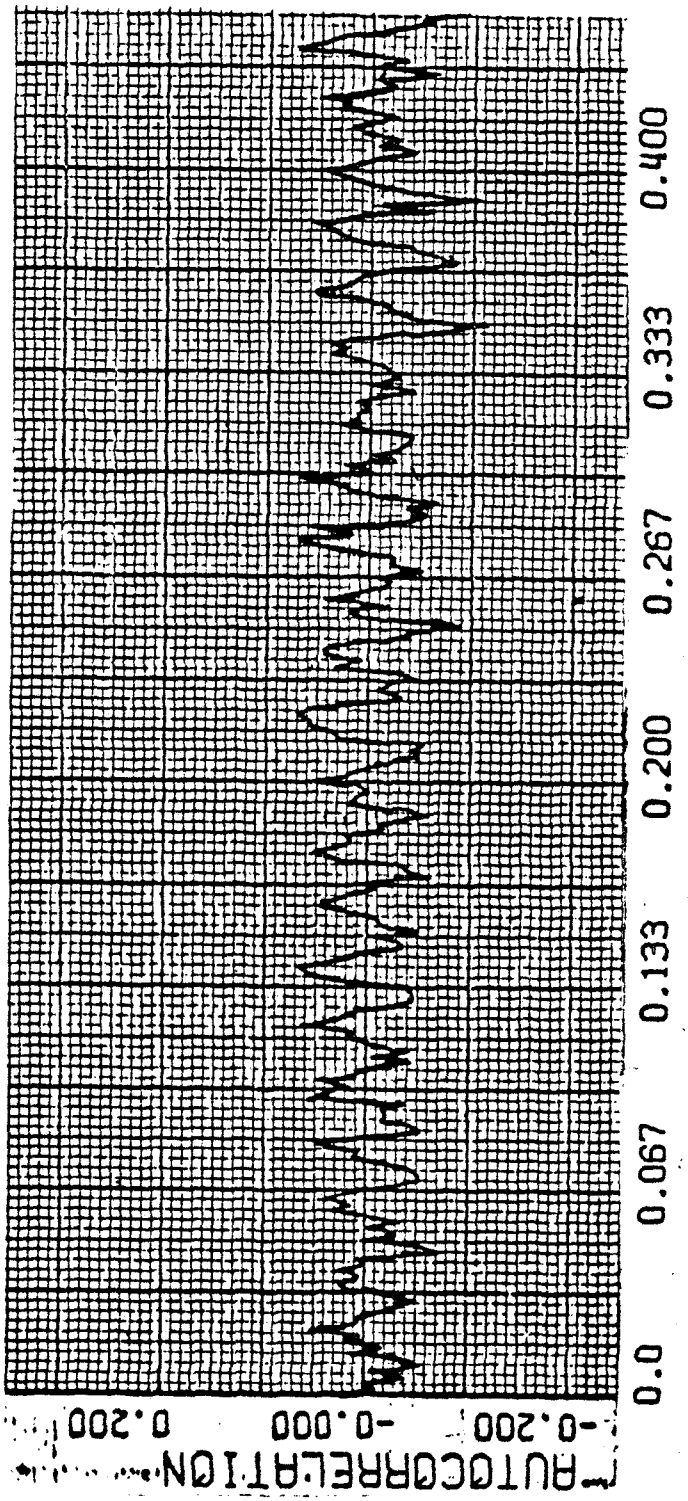
AUTOCORRELATION
-0.200
-0.000
0.200
0.0
0.067
0.133
0.200
0.267
0.333
0.400
Lag Time

Fig. II-5

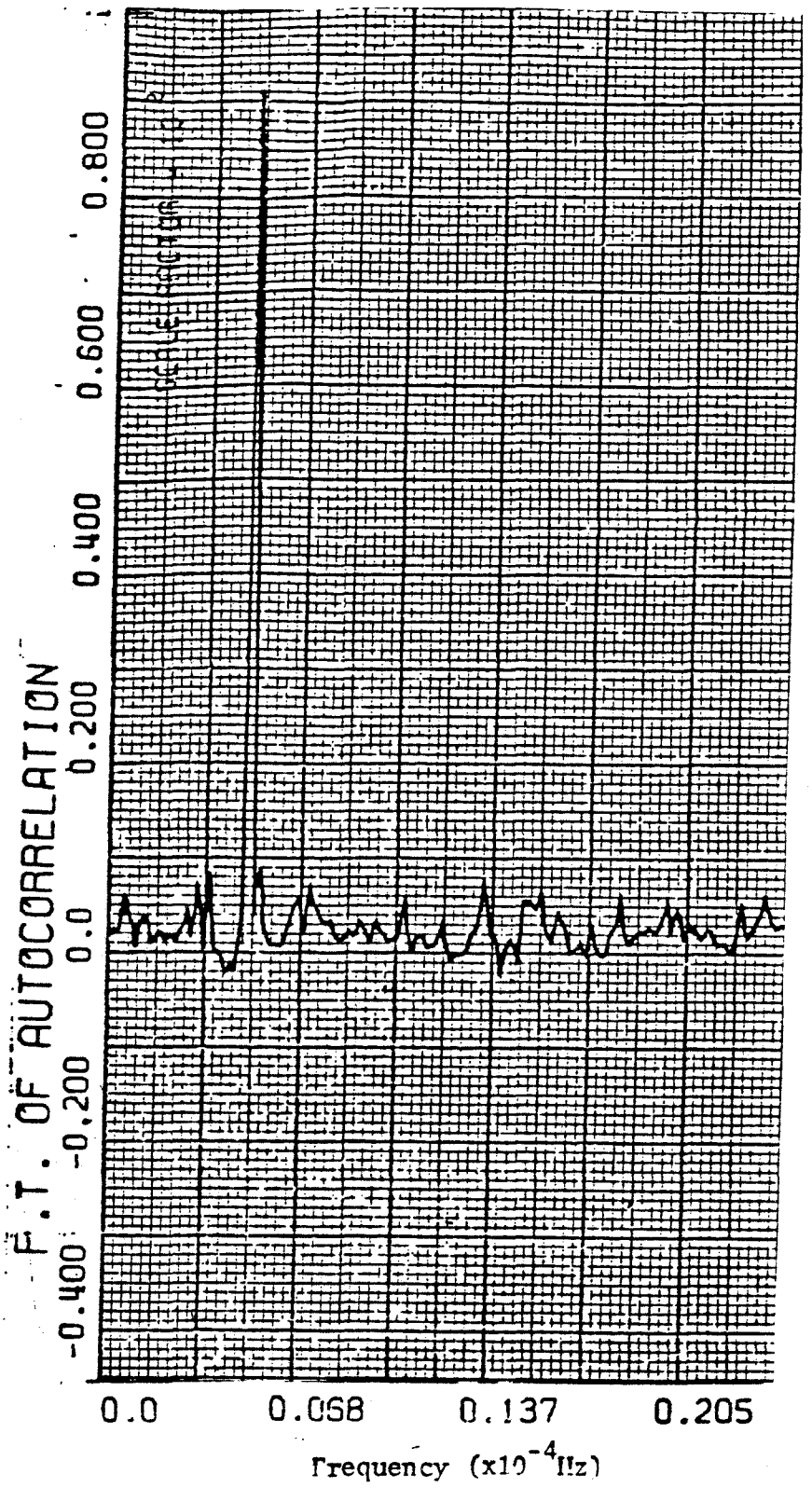
F.T. OF AUTOCORRELATION
-0.400
-0.200
0.0
0.200
0.400
0.600
0.800
0.0
0.068
0.137
0.205
Frequency (x10^{-4}Hz)

Fig. II-6

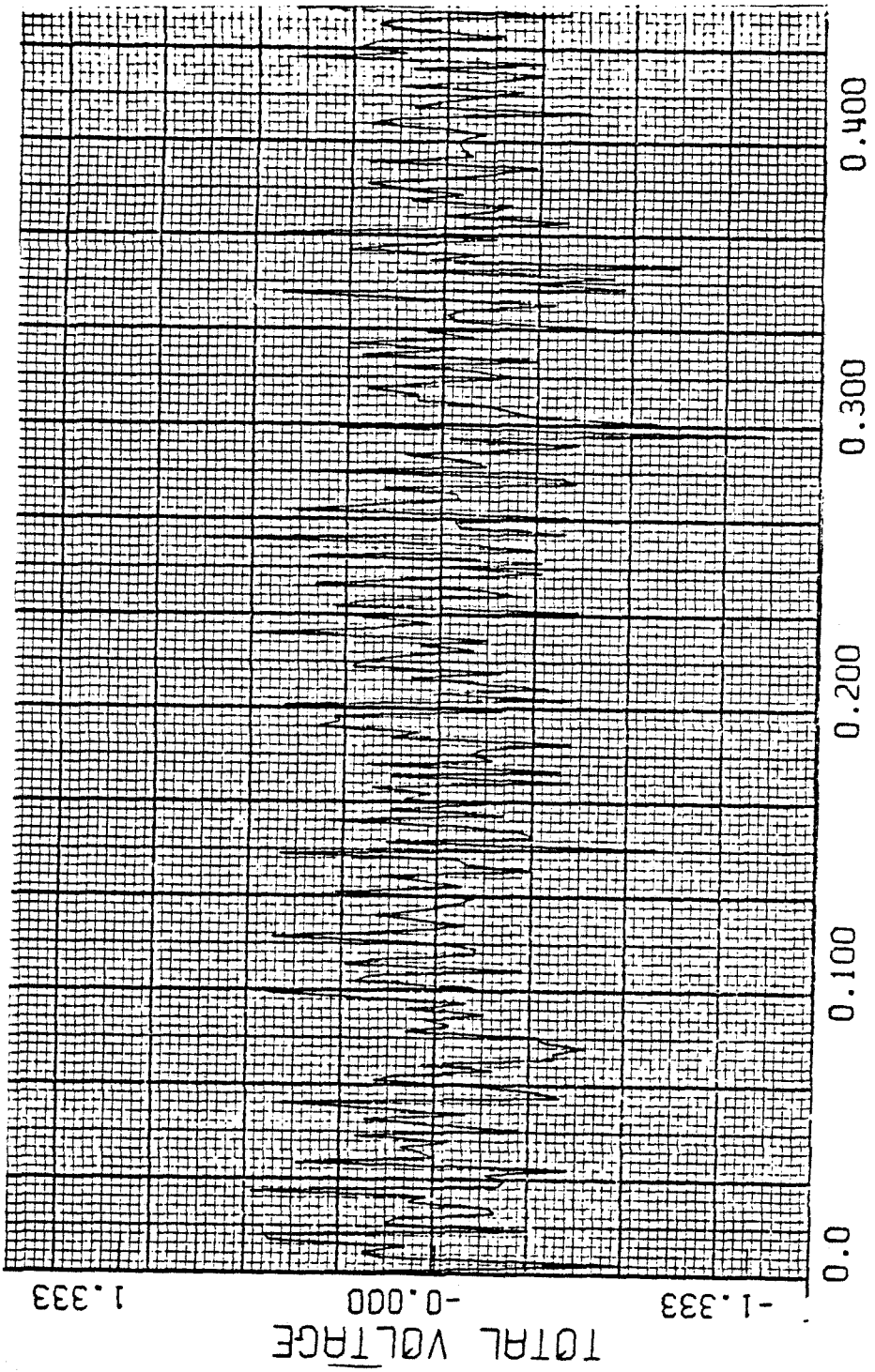

Fig. II-7

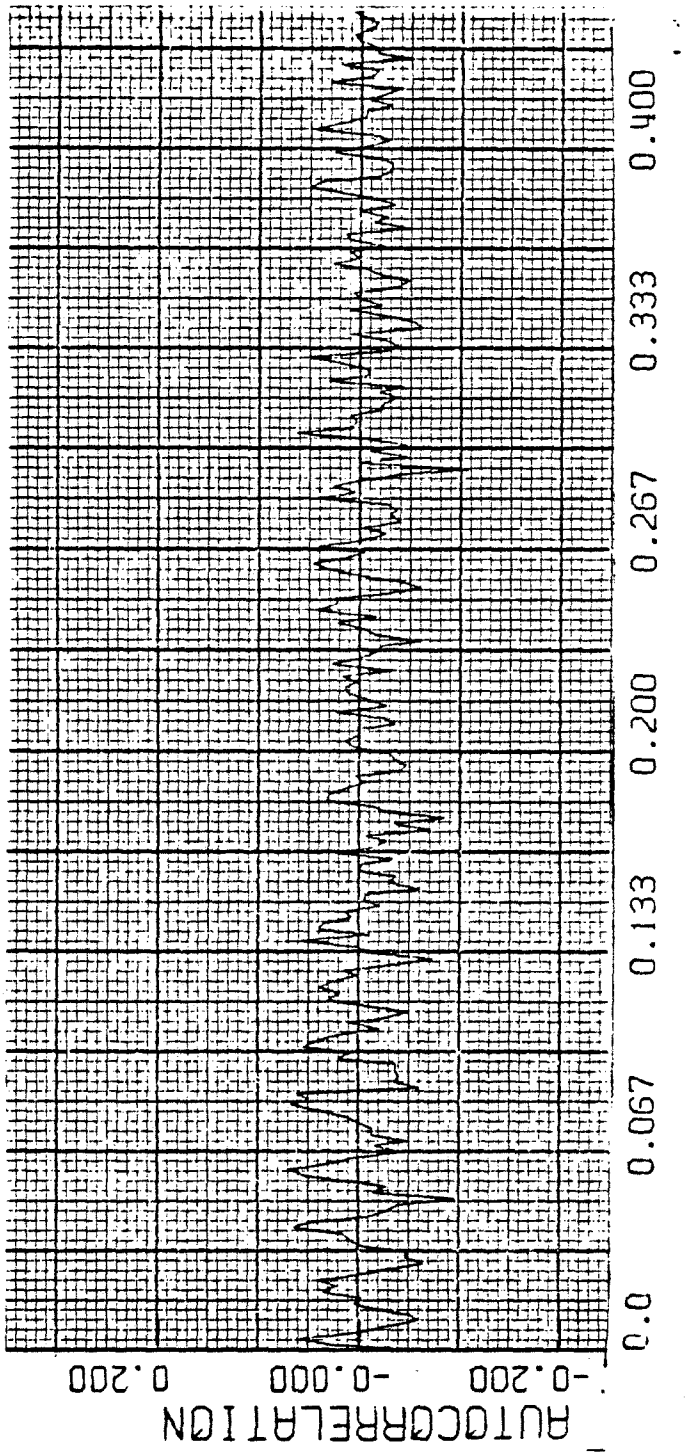
AUTOCORRELATION
-0.200
-0.000
0.200
0.0
0.067
0.133
0.200
0.267
0.333
0.400
Lag Time

Fig. II-8

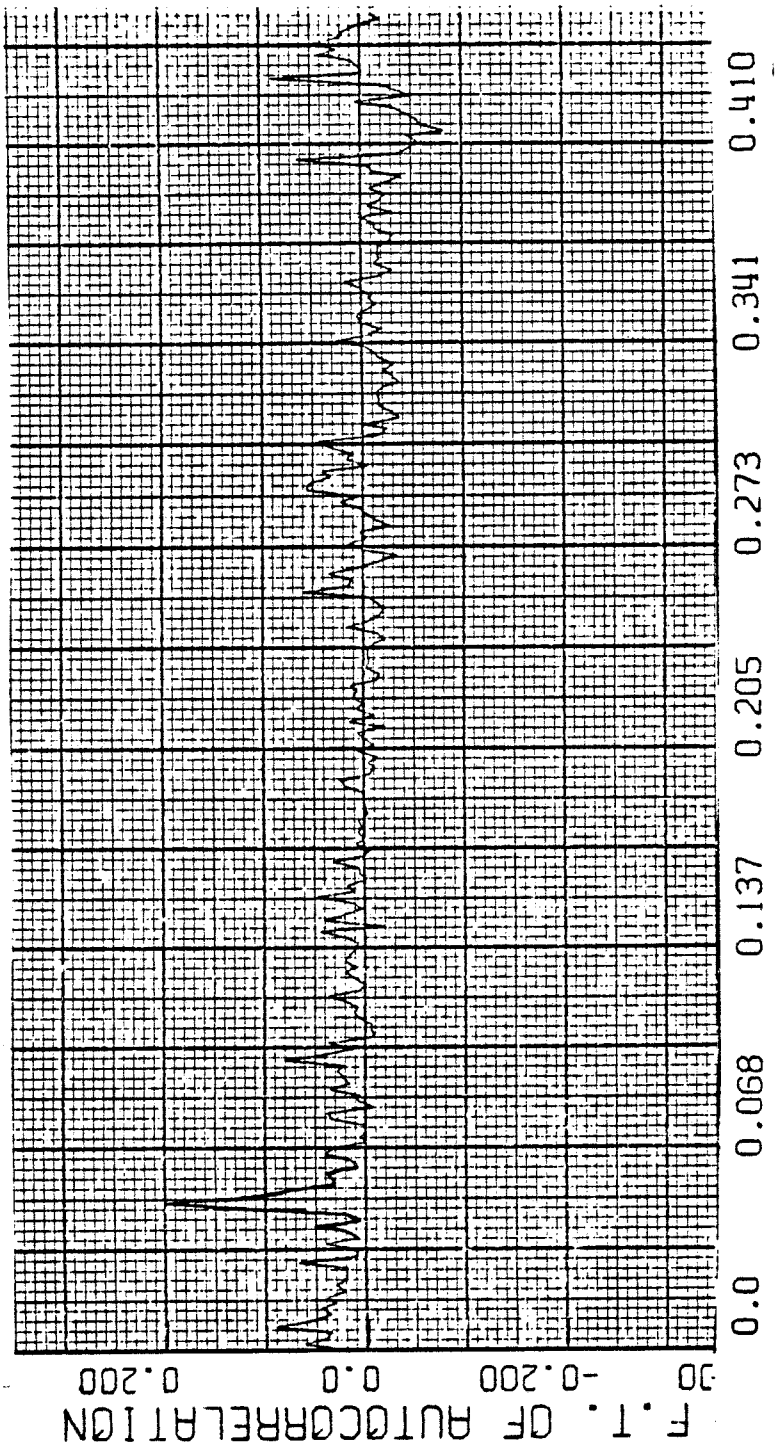
F.T. OF AUTOCORRELATION
0.200
0.0
-0.200
0.0
0.068
0.137
0.205
0.273
0.341
0.410
Frequency (x10^{-4} Hz)

Fig. II-9

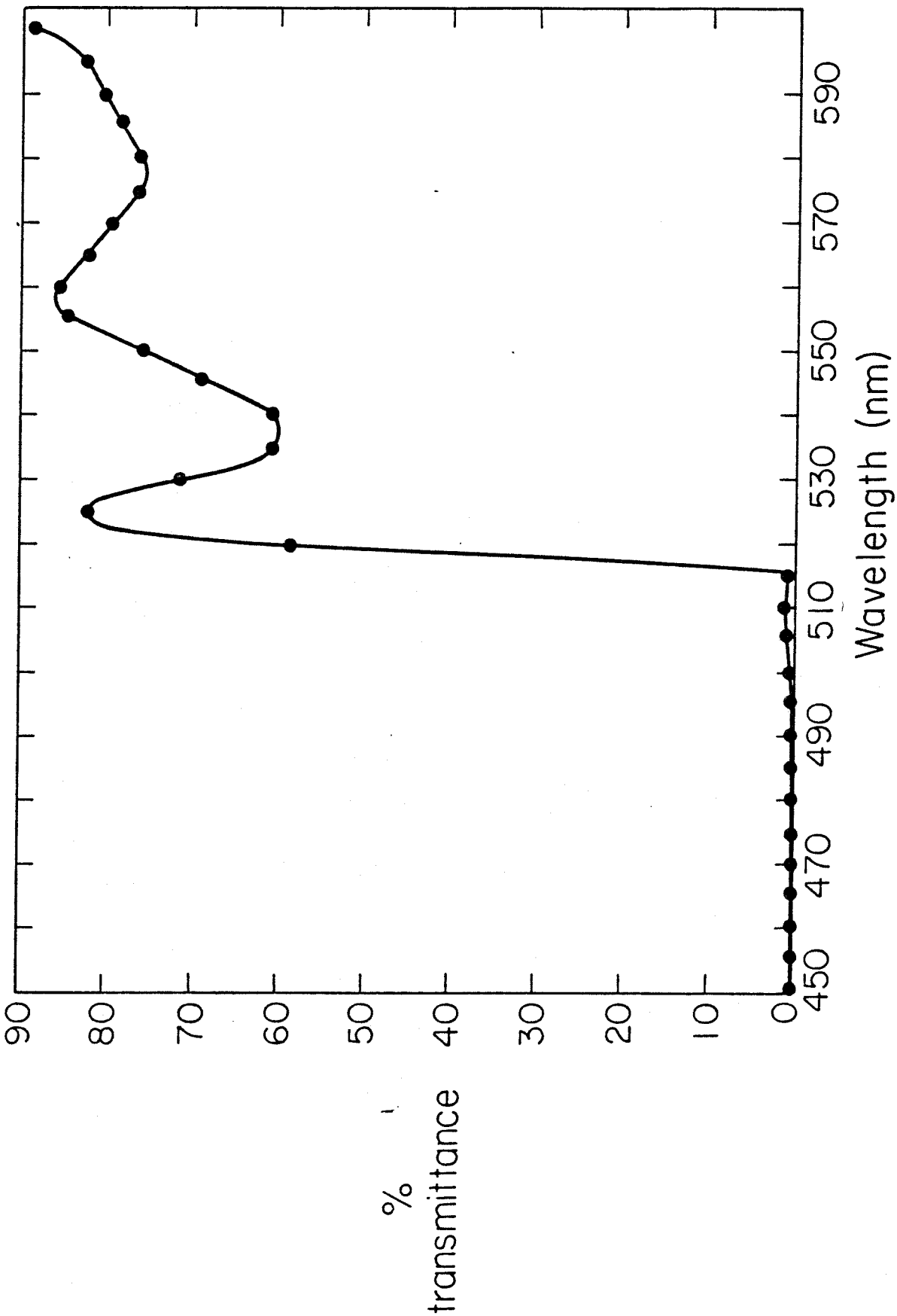
% transmittance
90
80
70
60
50
40
30
20
10
0
450
470
490
510
530
550
570
590
Wavelength (nm)

Figure III-1

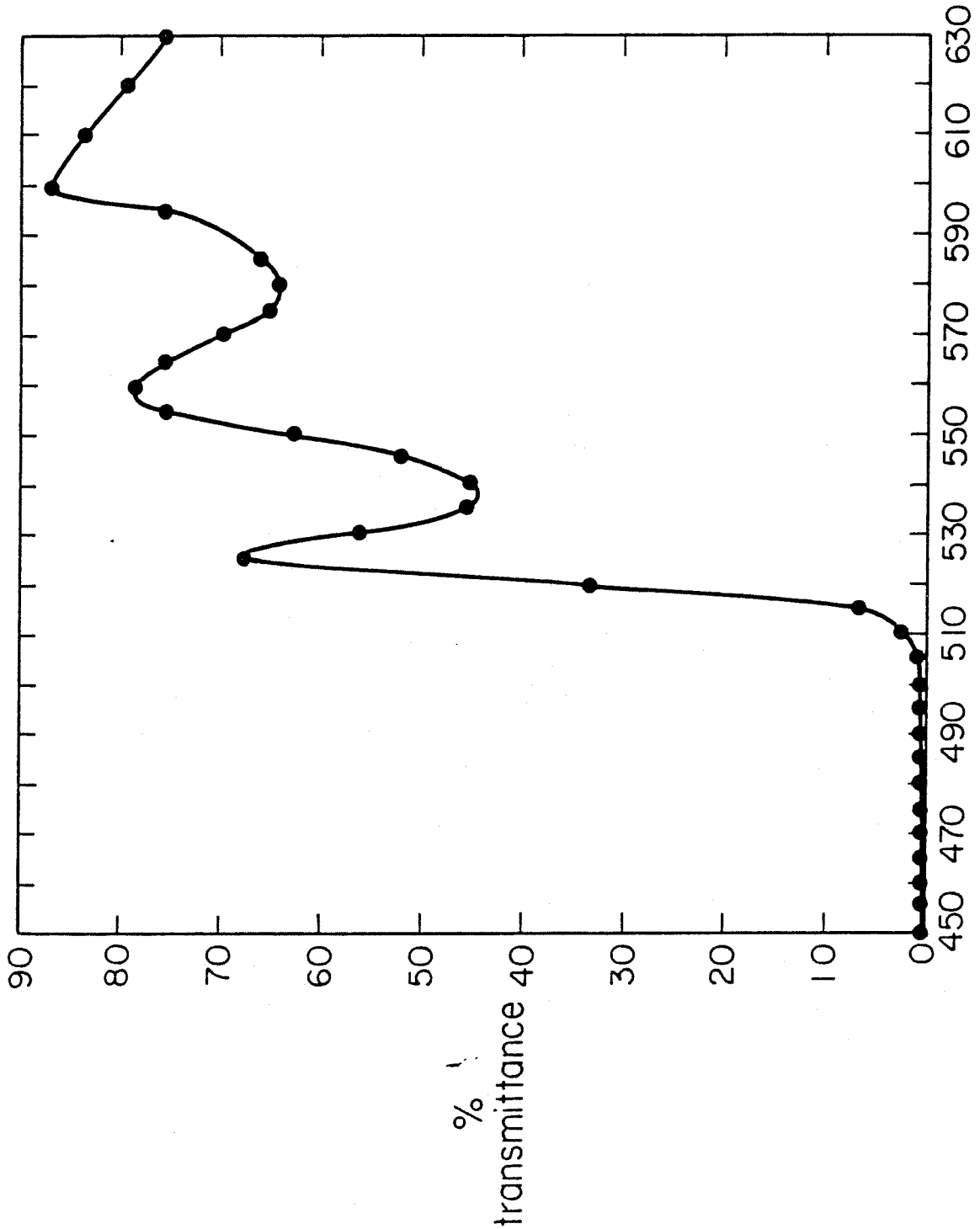
90
80
70
60
50
40
30
20
10
0
% transmittance
450
470
490
510
530
550
570
590
610
630
Wavelength (nm)

Figure III-2

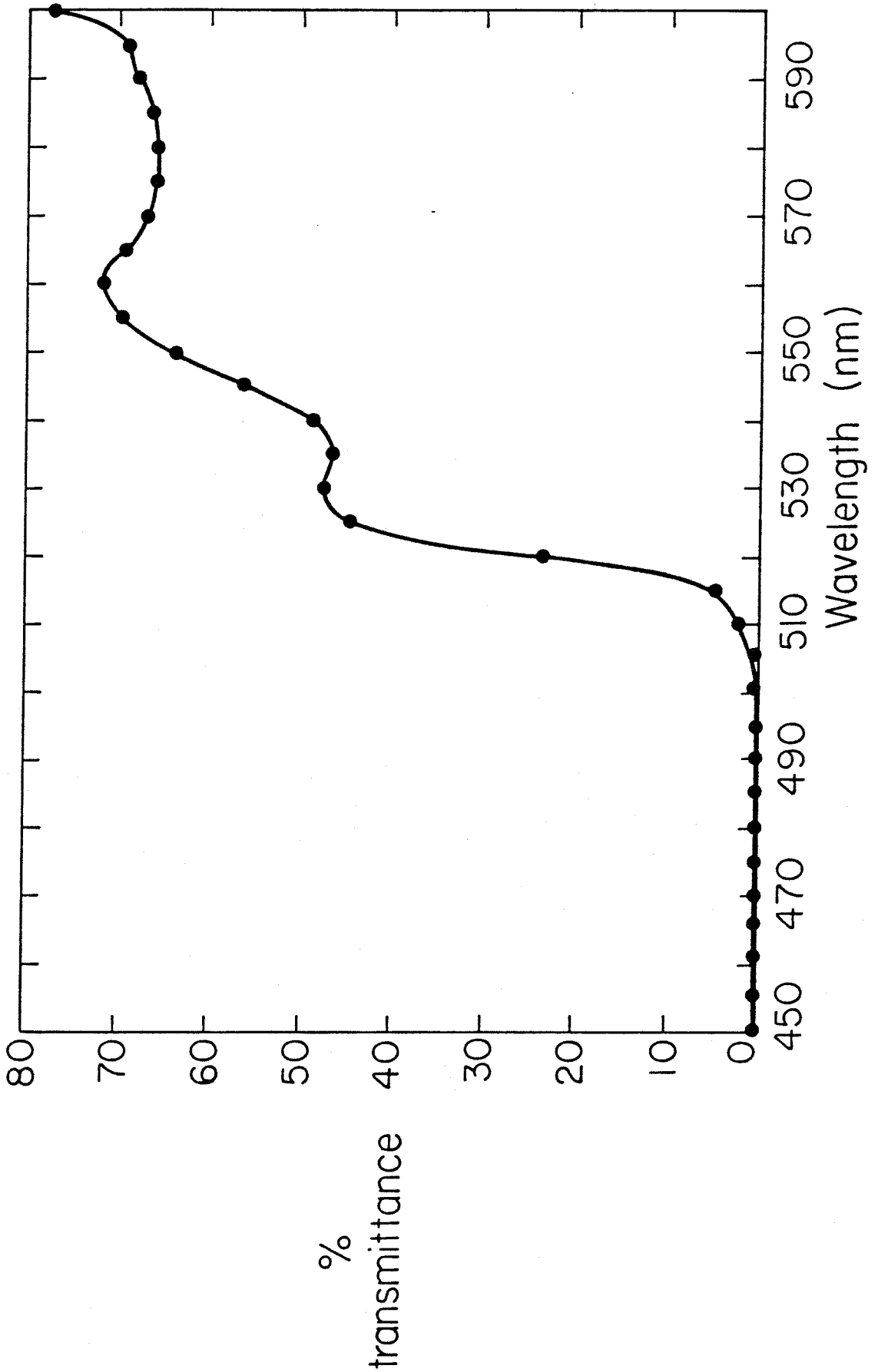
% transmittance
80
70
60
50
40
30
20
10
0
450
470
490
510
530
550
570
590
Wavelength (nm)

Figure III-3

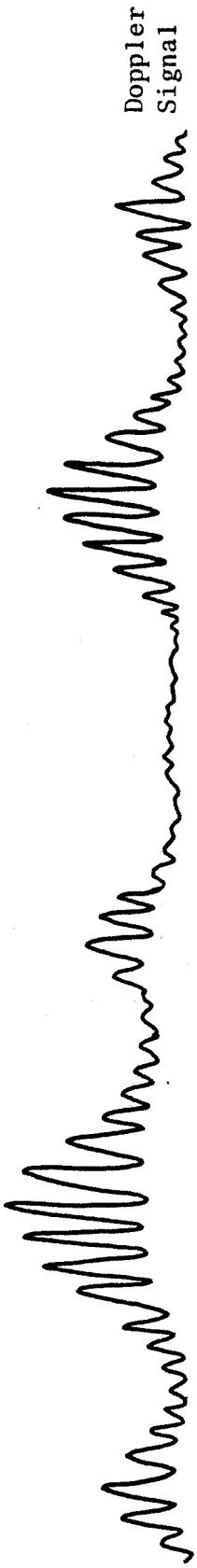

Fig. IV-1: Bursts of Doppler Signal

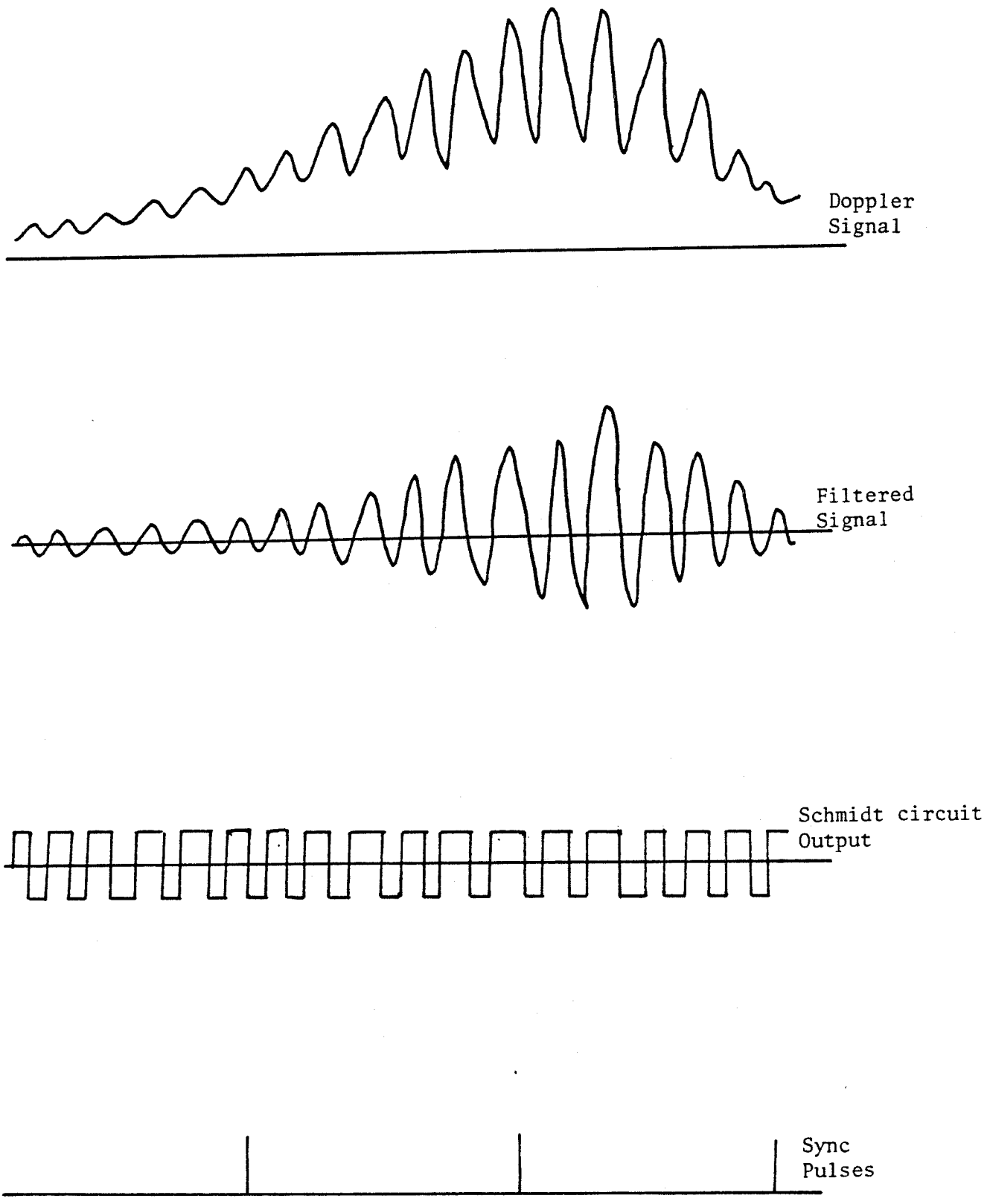

Fig. IV-2: Operating Principle of Frequency Counters

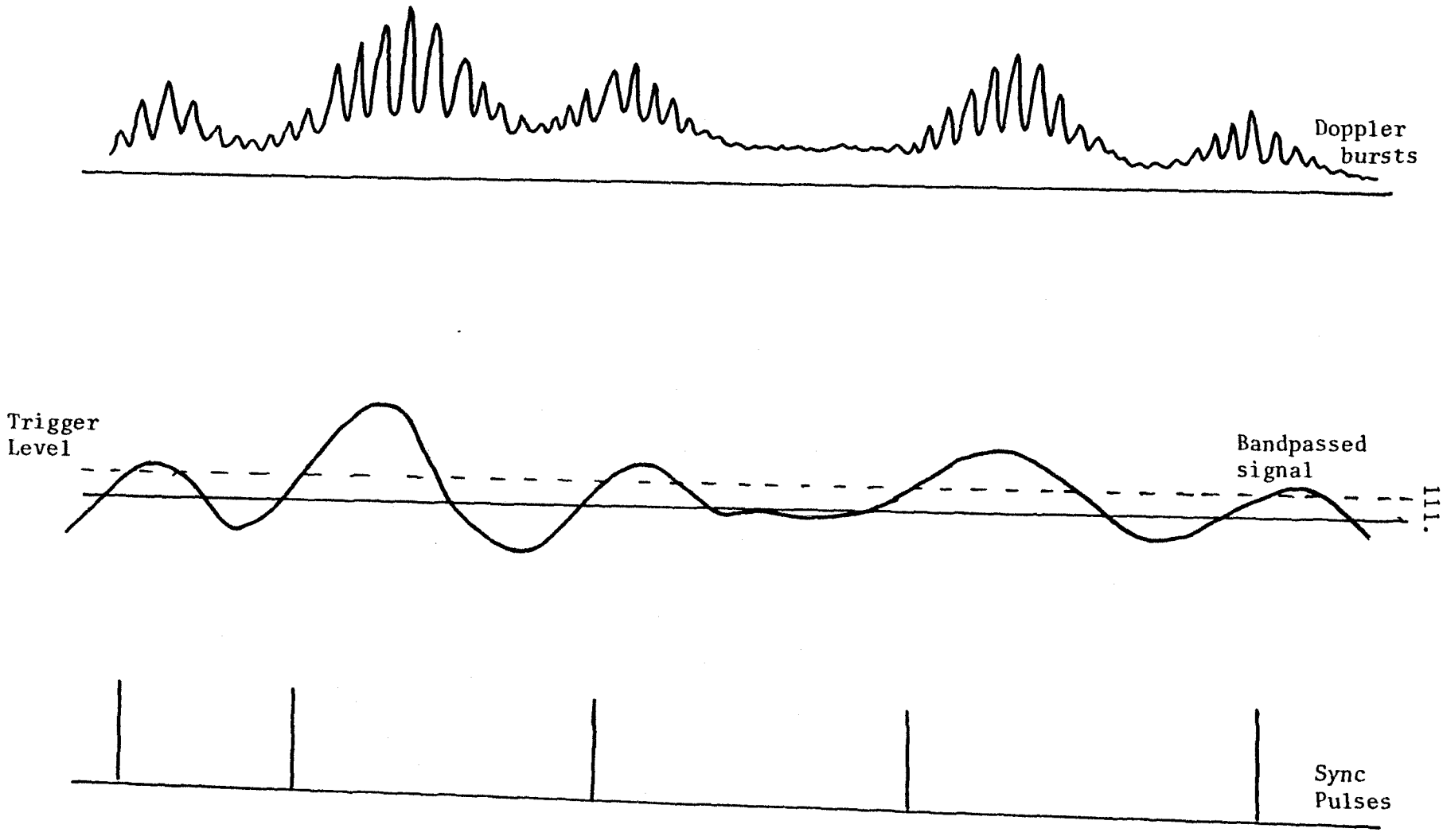

Fig. IV-3: Scheme for Burst Counting

Part II: Experimental Study of the Effective Thermal Conductivity in a Shear Flow of a Suspension of Rigid Spherical Particles.

I. Introduction

A large number of theoretical and experimental studies have been undertaken to investigate the rheological properties of suspensions. The constitutive behavior of suspensions for transport of heat or molecular species in the presence of a nonuniform bulk flow has, on the other hand, been largely neglected even though it is of great importance in many engineering applications. The present paper presents the results of an experimental study of the effect of a simple shear flow upon heat transfer in a suspension of rigid, spherical particles.

The pioneering work on the effective thermal properties of a suspension was published over 100 years ago by Maxwell (1873), who obtained a prediction for the effective thermal conductivity for a dilute stationary dispersion of solid spheres. Following this analysis, fairly extensive theoretical studies were also made for stationary suspensions of both high and low concentrations and with both spherical and nonspherical particles (Jeffrey, 1973; Rocha and Acrivos, 1973; Jeffrey, 1974). Since the macroscopic conductive heat flux is simply the ensemble average of the microscale conduction flux, the effective conductivity of a stationary suspension is found in all cases to differ from that of the suspended fluid only when the conductivities of the two phases are different. When the suspension undergoes a nonuniform bulk flow, however, a local disturbance flow is induced in the vicinity of each particle, thus creating a local convective flux of heat or molecular species. This additional local convective flux, dependent on the type and strength of the bulk flow, is found to contribute to the effective bulk conductivity or diffusivity of the suspension (Leal, 1973).

However, because of the structural complexities of suspensions, only a few detailed theoretical predictions exist for their transport characteristics when they are undergoing a non-uniform bulk flow, and these analyses are generally limited to dilute suspensions, simple shear flow and linear bulk temperature fields. The first rigorous analysis was due to Leal (1973) who considered the case of a sheared dilute suspension of spherical drops in the limit of low particle Peclet number $Pe = \frac{\bar{a}^2 G \rho C_p}{k}$. McMillen and Leal later considered a dilute suspension of: (1) slightly deformed drops (1975), and (2) a dilute suspension of rigid prolate spheroid particles with rotational Brownian motion (1976), both for low particle Peclet numbers and simple shear flow . Nir and Acrivos (1976) also studied the problem of spherical rigid particles in a linear shear flow with no Brownian motion but in the limit of large local Peclet number. The solution for this case is, however, extremely difficult and not yet fully complete.

Except for some preliminary experiments conducted by McMillen (1976) on the measurement of the effective thermal conductivity of a sheared suspension of rigid spherical particles, there has been no experimental confirmation of any of the predictive theories mentioned above. As we will see later, this is due in part to the stringent requirements and high sensitivity necessary to conduct such an experiment. In the study performed by McMillen (1976), a rotating Couette device was designed for the purpose of considering heat transfer across a simple shear flow. However, McMillen's original equipment lacked sufficient sensitivity and accuracy and his results were inconclusive. The present work is a continuation of that of McMillen, again for a suspension of rigid spherical particles. However, by incorporating various modifications to improve the method of experimentation,

we are able to obtain more conclusive results. We consider conditions of small concentration and small local Peclet number in order to compare with the available theoretical predictions. In addition, we extend the study to higher concentrations and intermediate Peclet numbers which have not been considered in the existing theories. This provides some knowledge of the transport behavior of suspensions in a range of direct technological interest, as well as a possible basis for further analysis outside of the somewhat restrictive conditions which are assumed in the presently available theories.

II. Theoretical Background

Prior to describing the experiments, it is useful to briefly review the theoretical analyses which were mentioned in the previous section for a suspension of rigid spheres. These theories consist of asymptotic limiting results for very large and very small values of the local particle Peclet number, respectively.

The small Peclet number case was considered by Leal (1973), who calculated the effective transverse conductivity for a dilute suspension of equal-sized spherical drops. The effective conductivity, k_s, evaluated for a rigid spherical particle was predicted to be

$$k_s = k_1 \left\{ 1 + \phi \frac{3(k_2 - k_1)}{k_2 + 2k_1} + \left[1.176 \frac{(k_2 - k_1)^2}{(k_2 + 2k_1)^2} + 3.0 - 0.14 \frac{(k_2 - k_1)}{k_2 - 2k_1} \right] \cdot Pe_1^{3/2} \phi + O(Pe_1^2) \right\} . \qquad (1)$$

Here,

$$Pe_1 = \frac{a^2 \rho C_p G}{k_1}$$

is the local Peclet number, while k_2 and k_1 are the thermal conductivities of the particle and suspending fluid, respectively. It can be seen that the effective conductivity of the suspension is predicted to always increase when the bulk shear rate is increased. The flow-induced enhancement of the transport rate is $O(Pe_1^{3/2})$.

Nir and Acrivos (1976) analyzed the opposite limit of large Peclet number, again for rigid spherical particles in a linear shear flow. Because of the existence of closed stream surfaces near the particle, the calculation of the microscale temperature distribution around each particle is extremely complicated in this case and was not solved completely. By using certain assumptions about the integrability of the solution, however, Nir and Acrivos were able to provide an estimate of the flow-induced contribution to the effective conductivity,

$$\frac{k_s}{k_1} = O(1) + A_1 \phi Pe_1^{1/11} \qquad (2)$$

Here, A_1 is a constant to be determined (in principal) from the temperature distribution around each particle. The primary conclusion to be drawn from Eq. (2) is that Pe_1 must be <u>exceedingly</u> large before the asymptotically dominant $O(Pe_1^{1/11})$ term becomes significant. Thus, it may be expected that k_s/k_1 will be $O(1)$ and nearly constant for all but the largest, $\geq 10^{11}$, values of the local Peclet number.

The expressions (1) and (2) are, of course, equally applicable for

heat or mass transfer with the molecular diffusivity, D, replacing $\frac{k}{\rho C_p}$ and the Peclet number also defined in terms of D. However, the design of an experiment in heat transfer for a simple shearing flow is an easier task than the design of an experiment in material transport and we have pursued the heat transfer approach in this work. An experiment in heat transfer will generally allow values of Pe_1 in the range, $P_1 \leq O(1)$. For small Pe_1 and small ϕ, Leal's expression (1) should be applicable and one goal of the experiments was to test this fact. In addition, we considered larger values of Pe_1 and ϕ, where no theory presently exists.

Several limitations of Leal's theory should be mentioned since these influenced the design of the experiments. First, the particles were assumed to be identical in size and exactly spherical (deviations from sphericity were shown by McMillen and Leal (1975) to lead to an equation for k_s of fundamentally different form from Eq. (1)). Second, the particles were assumed to be small compared to the overall dimensions of the gap so that the suspension can be viewed macroscopically as a homogeneous continuum. Provided this condition is satisfied, the particle size only influences the degree of enhancement of the heat transfer rate by its effect on the local Peclet number. For larger particles, the interaction between particle and wall becomes important and the effect of shear on the rate of heat transfer will be specific to the details of the particular apparatus. The present investigation was thus restricted to small particles, though some size variation was used as one means of changing the Peclet number. Finally, the theory assumes that the material parameters, such as the viscosity and conductivity, are all constant (i.e. independent of spatial position) and that natural convection contributions to the macroscopic rate

of heat transfer are negligible. All of these latter assumptions require small temperature differences across the sample.

III. Objectives of the Experimental Study

The primary objectives of this study are:

(i) To test the theoretical prediction by Leal (1973).

For reasons stated before, experiments were performed to measure the enhancement in heat transfer due to a simple shear in a suspension. One objective of this study is to test Leal's calculation (1973).

(ii) To observe experimentally the behavior to heat transfer at higher local Peclet number than provided for in the theory.

Although Leal's theory requires that Pe be small, it is useful to study experimentally the behavior of the effective conductivity at Pe of O(1) or higher. The results from such a study will be of direct technological interest, as well as useful for many problems in material transfer.

(iii) To observe experimentally the heat transfer through more concentrated suspensions.

To date, all of the available theoretical analyses heat or mass transfer have been carried out for dilute suspension. Suspensions with moderate to high concentrations of the dispersed phase, however, are commonplace in many engineering applications. It is, therefore, useful to study experimentally the effect of particle concentrations above the dilute limit (> 1%).

(iv) To study the effect, if any, of the size of the spherical particles.

In all of the theoretical investigations, the size of the particles in the suspension were assumed to be small compared to the overall dimensions of the sample. This allowed the suspension to be viewed macroscopically as an homogeneous continuum. The influence of the size of the particles on the enhancement in bulk conductive heat transfer depends only on its effect on the local Peclet number. Because of the complication in dealing with the particle-wall interactions which arise for particles whose size is comparable to the dimensions of the overall system, attentions are restricted to small particles. With this qualitative restriction, however, the influence of different sizes of particles are examined, at least in part, to extend the range of local Peclet numbers used in the experiment.

(v) To study the effect, if any, of different bulk heat fluxes used in the experiment.

The enhancement in the effective thermal conductivity should be independent of the bulk heat flux used in the experiment, as long as it does not induce secondary flows or introduce significant variation in material constants within the sample. Verification was attempted by using different bulk heat fluxes in our study.

IV. Experimental Apparatus and Procedure

The experimental apparatus used in this study was a Couette flow device with a rotating inner cylinder and a concentric, stationary outer cylinder. A temperature difference was generated across the gap by heating the inner cylinder while simultaneously cooling the outer cylinder. An additional heater was affixed to the ends of the inner cylinder to minimize axial loss of heat. Natural convection was minimized by using a small gap width and by operating with a small temperature difference between the two cylinders.

The main features of the flow apparatus are shown in Figure 1. The inner cylinder was machined from a hollow tube of aluminum to an outside diameter of 9.866 ± 0.0013 cm. Two high-purity Nickel-A wires of 0.05 cm diameter, insulated with a 0.0025 cm coating of H-ml enamel, was tightly wrapped around a continuous groove machined in the surface of the aluminum cylinder to serve as heaters. The wires were then covered with an epoxy resin and the "heater" section machined to the final diameter. Connections of the wires from the rotating inner cylinder to the external electronics was made through four mercury cups mounted on the shaft of the cylinder (Figure 1). The central section of the wire was used to supply the heat flux used in the experiment while the outer segments were used for guard heating to minimize end effects. By monitoring the resistance of the central wire heater, the temperature of the wire could also be measured

(here, the wire acts as a simple resistance thermometer).

A precision-bore glass tube with a wall thickness of 0.3 cm and an inside diameter of 11.887 ± 0.008 cm was used as the outer, stationary cylinder. The glass cylinder was cut and the ends ground by hand to a length of about 30.0 cm. Because the alignment of the two concentric cylinders was critical to avoid secondary flows and other complications, two carefully machined alignment rings were used in the assembly of the apparatus. Another glass cylinder with an internal diameter of approximately 20.0 cm was positioned external to the precision bore glass tube and water at a fixed temperature was circulated from a constant temperature bath into the region between the two glass cylinders. Stainless steel baffles were used to insure turbulence and a virtually constant temperature in this region.

A Minarik variable speed motor and motor control device was used to rotate the inner cylinder. Small variations in the rotating speed of the apparatus were observable over a period of several days. Fortunately, this time period was much longer than the several hours needed to obtain a data point at each fixed rotational speed. To ensure the accuracy of the experiment, the rotational speed was measured at the beginning and end of each experimental run.

The required electrical circuits for the test and guard heaters are illustrated in Figure 2. For the test heater, a precision DC power supply, Powers Designs model 605, was used. A Hewlett-Packard model 6268B power supply was used for the guard heating. The resulting voltage applied to the test and guard heaters was measured at the mercury cups. The electrical current flowing through the test heater was evaluated by measuring the

voltage drop across a 1 ohm standard resistor placed in the circuit. Two John Fluke differential voltmeters, model 887AB, were used to measure the voltage across the test heater and the standard resistor.

The conditioning water for the outer cylinder was supplied from a constant-temperature water bath and the lines between the Couette device and the water bath were well insulated to minimize the effect of fluctuation in room temperature. As a result, the stability of the temperature in the water bath was better than $\pm$ 0.01^{o}C.

To insulate the flow apparatus from fluctuations in room temperature, the entire flow apparature was enclosed in a box constructed from two-inch thick styrofoam. As a result, the air temperature inside the box was constant to within $\pm$ 0.1^{o}C.

A Union Carbide lubricant, Ucon Oil HB-280-XY-23, was utilized for the suspending fluid. This oil is a mixture of various polyethylene and polypropylene glycols. It has a viscosity of about 1.34 poise (Union Carbide, 1971) and a density of 1.05 gm cm^{-3} at 26^{o}C, the average temperature within the suspensions during most of the experiment. At the same temperature the thermal conductivity is of the order 6.8 x 10^{-4} cal cm^{-1} (^{o}C)$^{-1}$ sec^{-1} and heat capacity about 0.44 cal gm^{-1}. The coefficient of thermal expansion is about 8 x 10^{-4} (^{o}C)$^{-1}$.

With the apparatus described above, the measurement of thermal conductivity was achieved by heating the inner cylinder and simultaneously cooling the outer cylinder while measuring both the heat flux and the temperature drop across the gap. The inner cylinder was heated by applying a constant voltage, E, across the test heater. The heat flux was determined by measuring the electrical voltage E and current I across the

test heater. The temperature at the outer cylinder was fixed by circulating water at a fixed temperature, T_w, between the two glass cylinders. This arrangement resulted in a constant flux of heat across the gap of the concentric cylinder Couette device. The average effective thermal conductivity of the suspension was then determined by measuring the temperature, T_1, at the surface of the inner cylinder (and thus the total temperature drop across the gap of the Couette flow device). In the experiments, the temperature T_1 was determined from the resistence of the test heater, which was in turn determined from the electrical voltage E and current I and the temperature-resistance characteristics of the heater.

Experiments were performed with suspensions containing different concentrations of the rigid spherical particles, ranging from a volume fraction of zero to 0.25. Prior to any experiments, the suspension was carefully "conditioned". After adding the particles to the Ucon oil, the suspension was vigorously stirred by hand until it appeared to be homogeneous visually. It was then stirred continuously for an additional day with a magnetic stirrer before being transferred to the concentric flow apparatus. Finally, before any data were taken, the suspension was conditioned within the apparatus for 8 - 12 hours at the desired temperature and at a slow rotational speed. The temperature of the conditioning water was typically 25.0^{o}C, and was virtually unaffected by fluctuations in the room temperature. A slight and reproducible increase in the water temperature was observed with increasing rotational speed of the inner cylinder, testifying to the effectiveness of the insulation of the system.

The desired heat flux across the gap between the two concentric cylinders was obtained by applying a predetermined voltage across the test

heater. For all the experiments a heat flux identical to that from the test heater was used for the guard heater. Two different heat fluxes were used for different sets of experiments which resulted in temperature differences of about $2^{o}C$ and $6^{o}C$, respectively, across the gap between the two concentric cylinders.

Three different sizes of rigid spheres were used in the study. These were polystyrene latex spheres supplied by Diamond Shamrock Chemical Company. The particles had very narrow distributions in size (Figures 3a, 3b). The mean diameters of the particles were: 34.6 microns with a standard deviation of 2.8 μm, 53.4 μm with a standard deviation of 3.8 μm, and 122 μm with a standard deviation of 4.7 μm. Because the particles were made from the same material and therefore had the same physical properties, the difference in size thus effectively served to extend the range of Peclet number for a given set of shear rates.

V. Derivation of Governing Equation

The description of the temperature and velocity distributions in the apparatus used in this study is, in general, very complex. The equations describing the velocity and temperature distributions are coupled since there are variations in the density and viscosity due to the non-uniform temperature distribution. Deviation from simple shearing flow as a result of the curvature of the apparatus, the establishment of natural convection, the action of viscous dissipation, and the existence of temperature induced variations in viscosity will all generally affect the temperature distribution. Furthermore, it is well known that the suspension is Newtonian only as long as the concentration of the dispersed phase is low and

the particle Reynolds number, describing the disturbances flow near the particles,is small (Jeffrey and Acrivos, 1976). In addition, for a suspension undergoing non-uniform bulk flow, there can be flow-induced non-uniformity in the particle concentration across the gap; for example, particle-free (skimming) layers near the apparatus boundaries. Finally, for sufficiently large values of the angular velocity of the inner cylinder, the flow may become unstable,leading to a Taylor vortex structure in which the dominant mechanism for heat transfer across the gap is convection rather than conduction (Taylor, 1923). Obviously, any of these effects would considerably complicate the interpretation of experimental data, and, in some cases, make the determination of an effective thermal conductivity impossible. Thus, both the experimental apparatus and the operating conditions for the experiments have been carefully designed to minimize these various complications.

Detailed considerations of all of the effects listed above can be found in Appendices A - D. The results of these studies as they pertain to the present experiments are summarized here. First, let us consider the effect of natural convection produced by the temperature differential across the gap of the Couette device. For an order of magnitude estimate, we can use the analysis of Batchelor (Batchelor, 1954) which pertains strictly to natural convection between two vertical plane boundaries. In order that the effects of natural convection be neglected, we require: first, that any changes in the temperature profile in the test region (i.e. in the central part of our device) be negligible; second, that the additional shear-rate produced by the natural convection flow be small compared to that imposed by the rotation of the inner cylinder;

and third, that the heat flux across the gap due to natural convection be small relative to that by "conduction". All of these conditions can be satisfied by making the temperature differential small enough across the gap. In the experiments reported here, the maximum ΔT was $6^{o}C$, and thus the maximum Rayleigh number was approximately 2.3×10^{3}. Our analysis using Batchelor's solutions shows that the temperature is unaffected over all but the final 2 - 3 cm at the top and bottom of the gap — i.e. well away from the test region. Further, the maximum shear rate due to natural convection is approximately 0.28 sec^{-1} at the walls and this is less than 10% of the imposed shear rate which has a minimum value of 2.6 sec^{-1} and ranged up to approximately 40 sec^{-1} at the highest rotation rates. Finally, the maximum heat flux due to natural convection was 1.5×10^{-4} cal cm^{-2} sec^{-1}, compared to the bulk heat flux due to conduction which ranged from 2.8×10^{-3} cal cm^{-2} sec^{-1} to 8.7×10^{-3} cal cm^{-2} sec^{-1}.

The effect of viscous dissipation was also considered and deemed negligible since the Brinkman number, a measure of the relative importance of viscous dissipation to heat conduction, was typically less than 10^{-4} for the experimental conditions employed.

The instability of the shear flow at large angular velocity of the inner cylinder can, of course, be eliminated by operating the Couette device at angular velocities below that for the onset of instability. Taylor (1923) considered the stability of the flow to infinitesimal disturbances and concluded that the flow is stable as long as the characteristic Taylor number, P, satisfies the condition

$$P \geq 0.0525.$$

For the Ucon oil used in the experiments, this condition corresponds to a

maximum rotational speed of about 10 rad sec^{-1} prior to the onset of instability. This estimation was confirmed by measuring the thermal conductivity of the Ucon oil (Figures 4 and 5). These results will be discussed in more detail in the next section. It was observed that the thermal conductivity increased rapidly, for a ΔT of $6^{o}C$, above rotational speeds of approximately 8.5 rad sec^{-1} and, for a ΔT of $2^{o}C$, above rotational speeds of approximately 9 rad sec^{-1}. In the experiments, the rotational speed was limited to approximately 8 rad sec^{-1} in order to avoid the possibility of instability.

The rheological properties of suspensions are influenced by the concentration, shape and size distribution of the particles, the presence of electrical changes, Brownian motion, and the type of flow being experienced. As a result, suspensions in general are non-Newtonian. For this reason, the viscosity of the suspensions used was measured in a Stormer Viscometer, a rotating cup device capable of creating rotational shear flows similar to those fo the Couette flow device used in this study. For shear rates up to approximately 40 sec^{-1}, with a corresponding Reynolds number of not more than 10^{-3}, the effective viscosity was virtually independent of the shear rate and the particle size for the three sizes considered at any of the concentrations used. These results were in agreement with the experimental observations of Krieger (1972). The presence of inhomogeneities in the particle concentrations across the gap can result from lateral migration due to the presence of weak inertial effects, cf. Ho and Leal (1974), or Segre and Silberberg (1962). Since the typical experiments were run for several hours in order to allow the system to attain thermal equilibrium, it is important to verify that significant migration would not occur in

that time period. Ho and Leal (1974) have shown that the lateral velocity for a single sphere due to inertia is proportional to $O(Re \cdot \kappa^2)$ where Re is the particle Reynolds number, $Re \equiv Ga^2/\nu$, and κ is the ratio of the particle radius to the gap size. In our experiments, the maximum Re was $O(10^{-3})$ while the largest value of κ was $O(10^{-2})$. Thus, in a typical period of three hours, a particle could migrate no more than 10^{-3} cm, which is only 0.1% of the gap width, and a significant degree of non-uniformity could not be established in our experiments via the migration mechanism. The other source of non-uniform particle concentrations is the simple geometric exclusion effect, which leads to a particle depleted region within one radius of the walls. In our experiments, the maximum particle size was only approximately .01 of the gap width, as already noted, and a simple analysis (Appendix D) shows that this effect could not significantly affect the measured flow contribution to the effective conductivity.

Finally, the viscosity of the suspending fluid is strongly dependent on the temperature. For temperature differences across the gap of the Couette device of the order of $6^{o}C$, as existed in some of our experiments, the viscosity of the suspending fluid will vary in the gap by as much as 32%, and this will be reflected in a similar variation in viscosity for the suspension. The effective thermal conductivity of the suspension will also vary across the gap, both because the thermal conductivity of the suspending fluid depends on temperature and because viscosity variations and profile curvature will cause the velocity gradient (and thus the local Peclet number) to vary across the gap (cf. Equation (1) where the dependence of k_s on Pe is demonstrated for a dilute suspension). The thermal conductivity

of the Ucon oil which we used is relatively insensitive to temperature variations of $2 - 6^{o}C$ which existed in our experiments. This simplifies the problem somewhat, but the temperature variation in the viscosity, and the resulting nonuniformity of the effective conductivity due to variation of the local Peclet number across the gap are not so obviously neglected. Surprisingly, however, a detailed analysis, given here in Appendix A, shows that the result obtained for the effective conductivity by neglecting these effects altogether is almost identical to the "exact" result which is obtained when they are included.

For the evaluation of the average effective thermal conductivity in the gap of the Couette device, it is therefore sufficient to use the results of the simpler analysis in which the density and the thermal conductivity are all assumed to be constant. This approach is advantageous for presentation here, because it is very simple and the main elements of the theory and experiments are not obscured by algebraic complexity which add little to understanding.

Thus, adopting a cylindrical coordinate system with the axis of the cylinders of the Couette device as the z-axis, the equation of motion in the θ-direction is

$$\frac{d}{dr}\left[\frac{1}{r}\frac{d}{dr}(rV_{\theta})\right] = 0 \qquad (3)$$

The inner cylinder of the Couette device rotates at an angular speed of ω_1 and the outer cylinder is stationary. The boundary conditions are therefore:

$$V_{\theta}(R_1) = \omega_1 R_1 , \quad V_{\theta}(R_2) = 0 , \qquad (4)$$

where R_1 and R_2 are the radii of the inner and outer cylinders, respectively. The solution to this simple boundary value problem is:

$$V_\theta(r) = \frac{\omega_1}{K^2 - 1}\left(\frac{K^2 R_1^2}{r} - r\right) \tag{5}$$

where $K = R_2/R_1$.

The thermal energy equation for the suspension is

$$\bar{k}_s\left[\frac{1}{r}\frac{d}{dr}\left(r\frac{dT}{dr}\right)\right] = 0 \tag{6}$$

where $\bar{k}_s$ is the average effective thermal conductivity of the suspension. For the outer glass cylinder wall, the thermal energy equation is

$$k_g\left[\frac{1}{r}\frac{d}{dr}\left(r\frac{dT_g}{dr}\right)\right] = 0 \tag{7}$$

where k_g is the thermal conductivity of the glass cylinder and T_g is the temperature distribution within the cylinder. The Couette device is subjected to a constant heat flux at the surface of the inner cylinder and held at a constant temperature at the outer surface of the outer cylinder. Thus, the boundary conditions are:

$$\begin{aligned} &\bar{k}_s \frac{dT}{dr}\bigg|_{r=R_1} = -q = \text{constant} \\ &\bar{k}_s \frac{dT}{dr} = k_g \frac{dT_g}{dr}\bigg|_{r=R_2} = -\frac{q}{K} \\ &T(R_2) = T_g(R_2)\ , \quad T_g(R_2 + \delta R) = T_w = \text{constant} \end{aligned} \tag{8}$$

where T_w is the fixed temperature of the conditioning water at the outer surface of the glass cylinder and R is the thickness of the wall of the

glass cylinder. T can be obtained readily by solving Equations (6) and (7) simultaneously:

$$T = \frac{qR_1}{\overline{k_s}} \ln \frac{R_2}{r} + \frac{qR_1}{k_g} \ln \frac{R_2 + \delta R}{R_2} + T_w \tag{9}$$

The average thermal conductivity $\overline{k_s}$ can therefore be obtained from Equation (9) by measuring the temperature $T(R_1)$ at the surface of the inner cylinder. The result for $\overline{k_s}$ is

$$\overline{k_s} = \frac{qR_1 \ln K}{T(R_1) - T_w - \frac{qR_1}{k_g} \ln \frac{(R_2 + \delta R)}{R_2}} \tag{10}$$

In the experiments, the heat flux, q, was generated by applying an electrical voltage E and current I through the test heater. The heat flux, q, per unit area of the test heater is then given by:

$$q = \frac{EI}{2\pi R_1 L f}$$

where L is the length of the test heater and f is the conversion factor:

$$1 \text{ cal sec}^{-1} = f \text{ watts} = 4.184 \text{ watts}$$

The temperature at the surface of the test heater, $T(R_1)$, was determined by measuring the electrical resistance of the heater, using the empirically determined relationship between the resistance and temperature of the wire

$$T(R_1) = 12.46 \frac{E}{I} - 195.4 \tag{12}$$

Substituting Equations (11) and (12) together with the known geometric parameters of the system into Equation (10) yields:

$$\overline{k_s} = \frac{7.01 \times 10^{-4}\ EI}{12.46\ \frac{E}{I} - 195.4 - T_w - 3.731 \times 10^{-2}\ EI} \tag{13}$$

Here, $\overline{k_s}$ is the average effective thermal conductivity in cal sec^{-1} $cm^{-2}(^oC)^{-1}$, E is the electrical voltage in volts, I is the electrical current in amperes and T_w is the temperature of the conditioning water in ^oC.

Our primary objective in this study is to determine the functional dependence of the effective thermal conductivity $\overline{k_s}$ on the Peclet number Pe relevant to the particle,

$$Pe = \frac{\rho C_p}{k} G\bar{a}^2$$

where ρ is the density of the fluid, C_p is the heat capacity, $\bar{a}$ is the radius of the particle and G the local shear rate experienced by the suspended particles. Because of the slight curvature effects from the flow device, the shear rate is not constant in the apparatus but, as found from equation (5), a weak function of radial position:

$$G(r) = \frac{-\omega_1}{(K^2 - 1)}\left[1 + \frac{K^2 R_1^2}{r^2}\right] \tag{14}$$

To evaluate the average Peclet number relevant to the suspension as a whole, we thus use the radially-averaged shear rate

$$\bar{G} = \left[\int_{R_1}^{KR_1} G(r)dr\right] \Big/ \left[\int_{R_1}^{KR_1} dr\right] = \frac{-\omega_1}{K - 1} = -4.94\ \Omega_1(sec^{-1}) \tag{15}$$

to define the radially-averaged Peclet number, $\overline{Pe}$.

It may be noted that the average shear rate $\bar{G}$ is identical to the shear rate in a Newtonian fluid between two infinite parallel plates

which are separated by a distance $(R_2 - R_1)$, with one plate moving at a speed of $\omega_1 R_1$ and the second plate stationary.

VI. Error Analysis

The degree of accuracy in the measurement of thermal conductivity can be established by considering Equation (13) used in the analysis of the data. If only first-order terms are retained, the error $\delta\bar{k}_s$ in the measured thermal conductivity caused by errors δE, δI and δT_w in the measurements of the voltage current, and conditioning water temperature is related by following equation

$$|\delta\bar{k}_s| = \left|\frac{\partial\bar{k}_s}{\partial E}\,\delta E\right| + \left|\frac{\partial\bar{k}_s}{\partial I}\,\delta I\right| + \left|\frac{\partial\bar{k}_s}{\partial T_w}\,\delta T_w\right| \qquad (16)$$

The partial differentials in Equation (16) may be obtained from Equation (13). When they are evaluated at the typical experimental conditions of $E \approx 5.64$ volts, $I \approx 0.315$ ampere and $T_w \approx 25.00^oC$, corresponding to $\Delta T \approx 2^oC$, Equation (16) then becomes

$$|\delta\bar{k}_s| = (6.73 \times 10^{-3}|\delta E| + 1.24 \times 10^{-1}|\delta I| + 1.78 \times 10^{-4}|\delta T_w|)\text{cal sec}^{-1}\text{ cm}^{-1}\,{}^oC^{-1} \qquad (17)$$

The electronics and measuring systems used in this study (see section III) have typical associated errors

$$|\delta E| < 0.0001 \text{ volt}, \quad |\delta I| < 0.00001 \text{ amp} \quad \text{and} \quad |\delta T_w| < 0.01^oC\ .$$

If a conservative value of $\bar{k}_s \sim 6.8 \times 10^{-4}$ cal sec^{-1} cm^{-1} $^oC^{-1}$ is used

(this is approximately equal to the measured thermal conductivity of Ucon Oil), we obtain the error estimates for $\bar{k}_s$ in Table 1.

Table 1

Error	$\frac{\lvert\delta\bar{k}_s\rvert}{\bar{k}_s} \times 100\ (\%)$
$\lvert\delta E\rvert < 0.001$	< 0.099
$\lvert\delta I\rvert < 0.00001$	< 0.18
$\lvert\delta T_w\rvert < 0.01$	< 0.26

Thus, the expected percentage error in k is:

$$\frac{\lvert\delta\bar{k}_s\rvert}{k_s} < 0.54\% \tag{18}$$

For $\Delta T \simeq 6^{o}C$, the expected percentage error in k, for errors of the same magnitude, is slightly less than 0.54%.

The uncertainty in the measured T_w gives rise to the largest share of the error in $\bar{k}_s$. This seemingly negligible error in $\bar{k}_s$ is actually comparable to the predicted enhancement in conductivity (Equation 1) due to a simple shear when both the local Peclet number and the volume concentration of the dispersed phase are small. It is for this reason that it was necessary to use such high precision instrumentation in the experiment, and this is also the reason why McMillen's early work (1976) was inconclusive.

VII. Experimental Results

A. Calibration of the Electrical Resistance of the Test Heater at Different Temperatures

As shown earlier, the accuracy of the temperature measured in the experiment was exceedingly critical. In order to use the test heater as a resistance thermometer, a good calibration had to be first obtained.

The calibration was performed by circulating water of constant temperature through the annular gap between the concentric cylinders. A constant voltage of 0.1600 volt was applied across the test heater. A resistor of 1 K ohm was connected in series to the test heater to minimize the heat flux generated by the current. The current through the test heater was measured by measuring the voltage across an 1 ohm standard resistor (Figure 4).

The temperature of the water circulated was varied from $20^{o}C$ to $27^{o}C$. Figure 10 gives the resulting plot of resistance of the heater versus temperature. The plot is seen to be virtually linear. A least-squares analysis of the data gave the following expression:

$$T_o = 12.462 \frac{E}{I} - 195.44$$

where T_o is the temperature in ^{o}C, E the applied voltage in volts, and I the current through the heater in amperes.

B. The Thermal Conductivity of Ucon Oil HB-280-XY-23

The thermal conductivity of the Ucon Oil HB-280-XY-23, used as the suspending fluid in this study, is known as a function of temperature (Union Carbide, 1971). If the rotational Couette device operated in an ideal manner for the purposes of measuring thermal conductivity, the value of k_1 determined for the oil alone, should be independent of the rotational speed and equal to the known value. However, thermal dissipation and other secondary effects are unavoidable in such a flow device. Actual measurements of the thermal conductivity of the Ucon Oil at different rotational speeds of the flow apparatus can thus serve to determine the degree to which such secondary effects are present.

Figures 5 and 6 are plots of the measured thermal conductivity of the Ucon Oil alone, i.e. k_1, at different rotational speeds ω_1 of the inner cylinder. The temperature differences, ΔT, across the annular gap between the cylinders were approximately 2^oC and 6^oC. With a ΔT of 2^oC and low rotational speeds, a small increase in the measured thermal conductivity of the Ucon Oil was observed with increasing rotational speed. This rate of increase in the thermal conductivity k_1 accelerated with increasing rotational speed. The increase in k_1 was most likely due to the effect of small thermal dissipation effects. At rotational speeds above 9 radians sec^{-1}, k_1 increased much more rapidly with rotational speed, possibly signifying the onset of instability of the flow.† Very similar

†The critical Taylor number for an isothermal system with Ucon Oil would occur at an angular velocity of approximately 10 radians/sec. However, the apparent critical values from our apparatus appear to decrease slightly as the temperature difference across the gap is increased.

behavior was again observed for a ΔT of approximately $6^{o}C$. In this case the increase in k_1 was substantial at rotational speeds above 8.5 radians sec^{-1}. For all subsequent experiments, the rotational speed was limited to 9 radians sec^{-1} for $\Delta T \sim 2^{o}C$ and to 8 radians sec^{-1} for $\Delta T \sim 6^{o}C$.

The slight increase in the measured thermal conductivity with increasing rotational speed cannot be neglected in the analysis of suspension data. The fractional increase in thermal conductivity due to the action of shear on the particles is expected to be of $O(\phi Pe^{3/2})$ and thus very small for small ϕ and Pe. Indeed, the small increase in thermal conductivity shown in Figures 5 and 6 was only slightly smaller than the predicted increase in thermal conductivity due to the shear flow in very dilute suspensions. The method used in data analysis for the suspension to account for the apparent shear dependence of the conductivity of the Ucon Oil will be discussed later in this section.

It may also be noted that the measured thermal conductivity was slightly different for the two temperature differences used. At $\Delta T \sim 2^{o}C$ and no rotation, the measured thermal conductivity was 6.784×10^{-4} cal sec^{-1} cm^{-1} $^{o}C^{-1}$, while the corresponding value at $\Delta T \sim 6^{o}C$ was 6.437×10^{-4} cal sec^{-1} cm^{-1} $^{o}C^{-1}$. The slight difference in the two values may be due to the higher average temperature in the Ucon Oil when ΔT was larger. The thermal conductivity of the Ucon Oil does decrease with increasing temperature (Union Carbide, 1971), but the data available (Union Carbide, 1971) are not sufficiently accurate to obtain any quantitative verification of this hypothesis for these small changes in temperature.

C. The Thermal Conductivity of the Polystyrene Latex Spheres

For suspensions of rigid spherical particles, the increase in thermal conductivity at low local Peclet number is predicted by Leal (1975) to be a weak function of the thermal conductivity of the particles. This point can be demonstrated readily from equation (1). In particular, it can be seen from equation (1) that the fractional increase in thermal conductivity in a simple shear flow is

$$\frac{\Delta k_s}{k_1} = \left[1.176 \frac{(k_2 - k_1)^2}{(k_2 + 2k_1)^2} + 3.0 - 0.14 \frac{(k_2 - k_1)}{k_2 + 2k_1} \right] \Phi \, Pe_1^{3/2} \qquad (19)$$

where Δk is the increase in thermal conductivity due to shear.

Limiting values for this expression are:

$$\frac{\Delta k_s}{k_1} = 3.364 \, \Phi \, Pe_1^{3/2} \quad \text{when} \quad \frac{k_2}{k_1} \to 0 \qquad (20)$$

$$\frac{\Delta k_s}{k_1} = 3.0 \, \Phi \, Pe_1^{3/2} \quad \text{when} \quad \frac{k_2}{k_1} = 1 \qquad (21)$$

and

$$\frac{\Delta k_s}{k_1} = 4.036 \, \Phi \, Pe_1^{3/2}, \quad \text{when} \quad \frac{k_2}{k_1} \to \infty \qquad (22)$$

It is thus evident that it is not critical to have an exact value for k_2 as long as the ratio $\frac{k_2}{k_1}$ is of O(1). This requirement will be satisfied with the highly conductive Ucon Oil for any reasonable estimate of k_2. On the other hand, if the value of k_2 were known, equation (1) would provide an exact theoretical prediction for either a sheared or stationary suspension of neutrally buoyant spheres.

A number of techniques exist for determination of the thermal properties of solids and liquids. It is, however, difficult to measure the thermal properties of an aggregate of small solid particles. Thus, instead of measuring the thermal conductivity of the particles directly, the thermal conductivity was deduced indirectly using measured values of the thermal conductivity of stationary suspensions of polystyrene latex spheres at different concentrations, and Maxwell's theoretical predictions for the same case

$$\frac{k_{so}}{k_1} = 1 + 3\,\frac{k_2 - k_1}{k_2 + 2k_1}\,\phi + O(\phi^2) \qquad (23)$$

where k_{so} is the thermal conductivity of a stationary suspension with volume fraction ϕ.

Figures 7 and 8 are plots of the measured values of the thermal conductivity vs. concentrations for the suspensions. At $\Delta T \sim 6^{o}C$ only the particles with $\bar{a}$ = 26.7 microns were used. At $\Delta T \sim 2^{o}C$, all three different size particles were used. Within experimental accuracy, the k_{so} of suspensions prepared from particles of different sizes, as shown in Figure 7, were essentially the same. Both of the plots 7 and 8 are virtually linear to a volume fraction of 0.25. When $\Delta T \sim 6^{o}C$, a best fit of the data was given by

$$k_{so} \approx (6.437 \times 10^{-4})(1 + 0.188\phi) \text{ cal sec}^{-1} \text{ cm}^{-1} {}^{o}C^{-1} \qquad (24)$$

Hence, applying equation (23), k_2 was estimated as

$$k_2 = 7.728 \times 10^{-4} \text{ cal sec}^{-1} \text{ cm}^{-1} {}^{o}C^{-1} \qquad (25)$$

When $\Delta T \sim 2^{o}C$, on the other hand, the thermal conductivity k_{so} was given by

$$k_{so} \approx (6.78 \times 10^{-4})(1 + 0.156\phi) \text{ cal sec}^{-1} \text{ cm}^{-1} {}^{o}\text{C}^{-1} \quad (26)$$

By applying equation (23) again,

$$k_2 = 7.900 \times 10^{-4} \text{ cal sec}^{-1} \text{ cm}^{-1} {}^{o}\text{C}^{-1} \quad (27)$$

The dependence on temperature of k_2 is thus seen to be weaker than that of the Ucon Oil.

Jeffrey (1974) obtained theoretical second-order corrections to Maxwell's prediction:

$$\frac{k_{so}}{k_1} = 1 + 3\gamma\phi + \phi^2\left[3\gamma^2 + \frac{3}{4}\gamma^3 + \frac{9}{16}\gamma^3\frac{\alpha + 2}{2\alpha + 3} + \frac{3\gamma^4}{2^6} + \ldots\right] \quad (28)$$

where $\alpha = \dfrac{k_2}{k_1}$ and $\gamma = \dfrac{\alpha - 1}{\alpha + 2}$.

If k_2, given in Equation (25), is used for this second-order correction, the following relation results

$$\frac{k_{so}}{k_1} = 1 + 0.188\phi + 0.012\phi^2 + \ldots \quad (29)$$

Similarly, for the k_2 given in Equation (27)

$$\frac{k_{so}}{k_1} = 1 + 0.156\phi + 0.0082\phi^2 + \ldots \quad (30)$$

The second-order corrections are therefore predicted to be negligible for the concentrations used, as indicated by the plots in figures 7 and 8.

D. The Effective Conductivity of Sheared Suspensions as a Function of Local Peclet Number

(i) Data Analysis

In the measurement of the thermal conductivity of suspensions at various Peclet numbers, the thermal conductivity, $\bar{k}_s$, was first determined directly from Equation (13). This thermal conductivity included the effects of the shear, the difference in the thermal conductivities between the two phases and any residual secondary effects that have not been eliminated by the precautions outlined in section IV. In order to isolate the effect of the shearing flow, contributions from other effects must be subtracted. Equation (1) shows that the effects of the shear and of the differences in thermal conductivities for a stationary suspension are additive. In order to at least partially account for any small residual effects from secondary causes, these were assumed to be additive to the other effects as well, and to have the same dependence on the angular velocity of the inner cylinder as for a suspending fluid alone, cf. Figures 5 and 6. The contribution to the effective thermal conductivity due to the presence of the shearing flow, Δk, was therefore calculated from the following expression:

$$\Delta k(\omega_1) = k_s - k_{so}(1 + m\,\omega_1^n) \tag{31}$$

Here, Δk is expressed as a function of ω_1, the rotational speed of the inner cylinder. The constants m and n were obtained from the plots in Figures 5 and 6.

Substituting the values of k_1 and k_2 obtained earlier into Leal's (1973) theoretical prediction for Δk, we find

$$\Delta k = 3.00\ k_1 \phi Pe_1^{3/2} \qquad (32)$$

for a dilute suspension.

As a test of the above expression, the relative augmentation in conductivity, $R = \frac{\Delta k}{k_1 \phi}$, was calculated for each data point and plotted against the local Peclet number Pe. Figures 9 - 15 give the resulting plots at different volume fractions, ϕ, along with the theoretical prediction, Equation (32).

The effect of any possible heat loss to the inside of the inner cylinder was not considered in Section VI. Since the temperature of the inner cylinder was virtually constant throughout each set of experiment, any heat loss to the inside of the inner cylinder should have been independent of Peclet number. By presenting the experimental results in terms of R instead of the measured thermal conductivity, the effect of possible heat to the inside of the inner cylinder was effectively cancelled.

(ii) Results and Discussion

The experimental data plotted in Figures 9 - 15 were obtained over a range of Peclet numbers varying from about 0.01 to 1.3, by varying the rotational speed and the size of the dispersed particles. Data for suspensions with the same volume fraction of the dispersed phase were plotted together.

Within experimental accuracy, there was not appreciable difference in the enhancement of conduction due to different sizes of the particles over the range of volume fraction from 0.01 to 0.25 used in the study. For the smallest particles with an average radius of 17.3 microns, the ratio between the annular gap width of the apparatus and the diameter of the particles was about 300. At this very large ratio the suspension could readily be viewed as homogeneous macroscopically. For the largest particles, the same ratio was about 82. The lack of any discernable dependence of Δk on the particle size indicates that suspensions with these rather large particles could still be viewed as homogenous within the apparatus.

As mentioned earlier, the data were plotted in terms of the relative augmentation in thermal conductivity, R, as a function of radially averaged

Peclet number Pe. The theoretical prediction for R is given by:

$$R = R_1 = 3.0\ Pe_1^{3/2}$$

To test this expression, each set of data was assumed to be correlated by the general expression

$$R = CPe^{d} ,$$

and the constants C and D were then calculated by a least squares regression analysis for each set of data. Tables II - IV list the results of the calculation. For Pe_1 up to 0.27, the exponent d varied from 1.21 to 1.91. However, the majority of values for different volume fractions were very close to the theoretical value of 1.5. On the other hand, it was found that the constants, C, departed substantially from the theoretical value of 3.0, even for small Pe and ϕ. It must be noted, however, that the constant C is very sensitive to the exponent d at small Pe. For example, in Table II, the measured C = 29.9 at ϕ = 0.01 was almost ten times the theoretical value. The exponent d in this case was 1.91. However, if the empirical value of R (either measured or calculated from the measured C and d) and the theoretically predicted value from $R = 3.0\ Pe_1^{3/2}$ are compared at Peclet numbers relevant to this case, we obtain

$$\text{At } Pe_1 = 0.01 , \quad \frac{R}{R_1} = \frac{29.9(0.01)^{1.91}}{3.0(0.01)^{1.5}} = 1.51,$$

while at

$$Pe_1 = 0.1 , \quad \frac{R}{R_1} = \frac{29.9(0.1)^{1.91}}{3.0(0.1)^{1.5}} = 3.88 .$$

Thus, the empirical correlation for R gives a much closer approximation to the theoretical expression than it might first appear.

When both the volume fraction and local Peclet number were small, the measured R was always larger than the theoretically predicted value. The difference between the measured R and R_1 first increased with increasing volume fraction ϕ. When $\phi = 0.05$, the measured R was about five times the value for R_1 at the same Peclet number. When ϕ was increased further, however, the difference between the theoretical and experimental values began to decrease. In fact, the measured R at higher volume fractions agreed very well with the theoretical prediction over most of the range of Pe.

The deviation of the experimental data from the "predicted" value was also dependent on the Peclet number. It first increased with increasing Pe, and then gradually decreased when Pe_1 approached O(1), for all volume fractions. The decrease in this deviation when $Pe_1 \sim O(1)$ was more evident at the higher volume fractions. When $Pe_1 \sim O(1)$, the power dependence on Peclet numbers also became much smaller, as shown in Table V. At the higher values used for Pe_1 and ϕ, the measured R eventually became smaller than the corresponding value for R_1.

The fact that the difference between the measured and predicted relative augmentation in conductivity, R, increased with increasing volume fraction ϕ from 0.01 to 0.05 indicates that these low concentrations still did not approach the dilute limit necessary for the application of the theory. Some of the difference between the measured and predicted R's may also have been due to non-negligible physicochemical interactions between the particles and the resulting formation of doublets and higher-order aggregates. These rheological interactions first resulted in augmentation in thermal conduction with increasing volume fraction. When the volume fraction was

increased further, the augmentation in thermal conduction due to interactions between particles gradually decreased.

A somewhat similar conclusion also applies for the dependence on Peclet number. The fact that the difference between the measured and predicted R's increased with increasing Pe_1 when $Pe_1 \sim O(10^{-1})$ again seems to indicate that the Peclet number used in this study was not sufficiently small to verify the theory. Conversely, the available theory did not account for all possible interaction effects contributing to enhancement in conduction at Peclet numbers ranging up to approximately 1. The dependence on Pe_1 gradually became weaker at higher Pe_1. This agrees, at least partially, with the prediction by Nir and Acrivos (1976) that for large Pe_1 the variation in enhancement with Pe_1 is extremely weak. However, the largest Pe_1 used in this study was only of O(1), and we obviously could not test Nir and Acrivos' prediction of a $O(Pe_1^{1/11})$ enhancement to conduction at large Pe_1.

At all volume fractions and Peclet numbers used in this study, the observed enhancement in thermal conduction was of the same order of magnitude as predicted by Leal's analysis for small ϕ and Pe_1 (1973). This result was unexpected at high Pe_1 and high volume concentrations of particles. However, it appears that the theory could be used for order of magnitude estimations of thermal conductivity of sheared suspensions over the whole range of conditions that are considered in this study, in spite of the fact that it obviously does not give a complete physical description of the transport behavior.

Better qualitative agreement between experimental observation and theoretical prediction might be achieved with more dilute suspensions and

smaller Peclet numbers than those used in this study. However, the experimental accuracy required to detect the extremely small changes under these conditions precludes such a study in our apparatus.

The measured enhancement in thermal conductivity differed slightly at the two temperature differences, ΔT, used. At $\Delta T \sim 2^{o}C$, however, the thermal conductivities measured were on the average not more than 3% larger than the corresponding thermal conductivities measured at $\Delta T \sim 6^{o}C$.

(iii) Summary of modifications which produced the improved accuracy of the experimental system.

The data obtained in this study were reproducible and with greatly reduced scatter compared to McMillen's (1976) study. Because both studies used essentially the same apparatus, it would be instructive to summarize the modifications that achieved the degree of accuracy in the present study. These modifications can be divided into two classes: (1) Modifications of the experimental system, and (2) Corrections used in the analysis of the experimental data, made possible by the improved sensitivity of the experimental system. The major changes made to the experimental system were:

(a) The use of highly accurate and stable power supplies and voltmeters for the generation and measurement of the heat flux. To further improve their stability they were run on regulated power sources. The power supply and voltmeters used were about the most accurate available commercially, and they were absolutely necessary to detect the smallest changes observed in this study.

(b) The use of a highly sensitive regulator to maintain the temperature of the conditioning water. Coupled with the insulation of the entire circulation system, it reduced the fluctuation of the water temperature to less than $0.01^{o}C$, as opposed to the nominal value of $> 0.03^{o}C$ experienced by McMillen (1976).

(c) The use of an improved calibration of the temperature-resistance characteristics of the test heater to determine its temperature. The correlation between temperature T_o and the resistance R_H $(=E/I)$ obtained from the calibration performed in this study was given by:

$$T_o = 12.462 \frac{E}{I} - 195.44 \ , \tag{33}$$

while McMillen (1976) obtained the correlation:

$$T_o = 14.24 \frac{E}{I} - 227.68 \ . \tag{34}$$

For the typical values of E = 5.64 volts and I = 0.315 amp, the temperature of the heater as calculated from Equation (34) would be $0.4^{o}C$ smaller than that calculated from Equation (33). An error of $0.4^{o}C$ would increase the measured thermal conductivity by about 10%.

(d) The isolation of vibration that might have affected the stability of the flow. The main source of vibration in McMillen's study was generated by pumps connected to the same table where the flow apparatus was located. Since the flow was generated by rotation of the inner cylinder, the resultant flow was inherently unstable. The vibration from the pumps could have affected the stability of the

flow in McMillen's study. By isolating the pumps from the table, the vibrations were eliminated.

(e) Thermal insulation of the flow apparatus from fluctuations in room temperature. By enclosing the entire apparatus in a styrofoam box, this insulation helped to maintain the temperature inside the box to within $0.1^{o}C$.

As a result of the improved sensitivity and stability of the system, we were able to measure the thermal conductivity of the dispersed phase and the effect of secondary flow. These measurements made possible the following corrections in the analysis of data:

(a) To properly correct for the effect of the difference in thermal conductivity of the two phases. McMillen (1976) assumed in his study that $k_2 \approx \frac{k_1}{2}$. Because of the considerable scatter in his experimental data, he had to correct for the difference in the thermal conductivities by using Maxwell's prediction and the assumed value for k_2. In this study, k_2 was found to be about 1.2 k_1 instead. Depending on the volume fraction of the suspension, this difference in the value of k_2 would have increased the thermal conductivity of the suspension by about (80 ϕ) %.

(b) Effects of secondary flow were observed and contributions to conduction were subtracted from the results.

VIII. Conclusion

The observed enhancement in the thermal conductivity in a sheared suspension in this study was always of the same order of magnitude as predicted by Leal's theory (1973). Though Leal's theory was limited to dilute suspensions, it agreed amazingly well with observed enhancements in conductivity even for moderately concentrated suspensions. However, judging from the variations in the deviation between the experimental observations and theoretical prediction, it was evident, as expected, that the theory does not completely describe the transport behavior for the whole range of Peclet numbers and volume concentrations of the suspensions used in this study. Surprisingly, the experimental observations indicated that volume fractions of $O(10^{-2})$ and Peclet numbers of $O(10^{-1})$ are not sufficiently small to approach the asymptotic theory for $Pe \to 0$, $\phi \to 0$.

Observations on the heat transport behavior at Peclet numbers of O(1) and higher concentrations may also be relevant to many problems in enhanced molecular diffusion. The lack of any theoretical analysis in these regimes makes the results obtained in this study particularly useful. It should be noted, however, that the empirical correlations obtained from this study are extremely sensitive to the Peclet number and should not be used for Peclet numbers much different from those for which the correlations were derived.

APPENDIX A: The Effects of the Variations in Viscosity and Thermal Conductivity and the Curvature of the Couette Device on the Velocity and Temperature Distributions.

In the derivation of the governing equations for the experimental system in the body of this paper, the viscosity as well as the thermal conductivity of the suspension in the gap of the rotating Couette device was assumed to be constant. For temperature differences across the gap of the Couette device of the order $6^{o}C$, as existed in some of the experiments, the viscosity of the suspending fluid will vary in the gap by nearly 32%, and this will presumably be reflected by a similar variation in the effective viscosity for the suspension. The effective thermal conductivity of the suspension will also vary across the gap because of the dependence of the thermal conductivity on the temperature of the suspending fluid and because of variations in viscosity which will cause the velocity gradient (and thus the local Peclet number) to vary across the gap (cf. Equation (1) where the dependence of k_s on Pe is demonstrated for a dilute suspension). Further variation in the velocity gradient will be caused by the profile curvature, due to the finite gap size in the Couette device. The effect of temperature induced variations in viscosity and of variations in thermal conductivity across the gap of the Couette device are investigated in this appendix.

Consider first the motion of a suspension of rigid spherical particles modeled here as a Newtonian fluid with constant density but a temperature-dependent viscosity in the gap of a concentric cylinder Couette flow device. For most fluids the thermal conductivity has a much weaker dependence on temperature and this effect will be ignored here. Over the

range of temperature used, the viscosity can be adequately represented by the expression

$$\mu_s = \mu_o \exp\left[-\beta\frac{(T - T_o)}{T_o}\right] \tag{A1}$$

where μ_o is the viscosity at T_o, and β is an empirical constant (Nahme, 1940). By taking a cylindrical coordinate system with the axis of the cylinders as the z-axis, the equation of motion in the θ-direction can be written as

$$\frac{d}{dr}(r^2\tau_{r\theta}) = -\frac{d}{dr}\left[r^3\mu_s\frac{d}{dr}\left(\frac{V_\theta}{r}\right)\right] = 0 \tag{A2}$$

With the outer cylinder of the Couette device stationary and the inner cylinder rotating at an angular speed of ω_1, the boundary conditions are

$$V_\theta(R_1) = \omega_1 R_1 , \quad V_\theta(R_2) = 0 \tag{A3}$$

Including the viscous dissipation term, the energy equation in the suspension can be written as

$$\frac{1}{r}\frac{d}{dr}\left(r\,k_s\frac{dT}{dr}\right) + \mu_s\left[r\frac{d}{dr}\left(\frac{V_\theta}{r}\right)\right]^2 = 0 \tag{A4}$$

where k_s is the effective thermal conductivity of the suspension. For the glass wall of the outer cylinder, the energy equation is

$$kg\,\frac{1}{r}\frac{d}{dr}\left(r\frac{dTg}{dr}\right) = 0 \tag{A5}$$

Tg here denotes the temperature field in the glass cylinder and k_g is its thermal conductivity. The Couette flow device is subjected to the conditions of constant heat flux at the inner cylinder surface and constant

temperature, equal to that of the conditioning water, at the outer surface of the outer cylinder. The boundary conditions are therefore:

$$k_s \frac{dT}{dr}\bigg|_{r=R_1} = -q = \text{constant} \tag{A6a}$$

$$k_s \frac{dT}{dr} = kg \frac{dTg}{dr}\bigg|_{r=R_2} = -\frac{q}{K} \tag{A6b}$$

$$T(R_2) = Tg(R_2) \tag{A6c}$$

$$T(R_2 + \delta R) = T_w = \text{constant} \tag{A6d}$$

δR is the thickness of the glass cylinder. T_w is the temperature of the conditioning water, and K is the ratio $\frac{R_2}{R_1}$.

By using the dimensionless variables:

$$\rho = \frac{r}{R_1}, \qquad V = \frac{V_\theta}{\omega_1 R_1} \quad \text{and} \quad \theta = \beta \frac{(T - T_o)}{T_o},$$

the velocity field can be expressed as

$$V = \rho \left[1 - \frac{\int_1^\rho \frac{e^\theta}{t^3}\, dt}{\int_1^K \frac{e\theta}{t^3}\, dt} \right] \tag{A7}$$

For a suspension undergoing shear flow, the thermal conductivity can be written as

$$k_s = k_{so} + \Delta k \tag{A8}$$

where k_{so} is the thermal conductivity of the suspension at rest and Δk is the contribution to the conductivity due to the presence of the shear flow.

Δk is a function of the shear rate and therefore a function of radial position. Equation (A4) then becomes

$$\frac{1}{\rho}\frac{d}{d\rho}\left[\left(1+\frac{\Delta k}{k_{so}}\right)\rho\frac{d\theta}{d\rho}\right]+\beta\frac{\mu_o\omega_1^2R_1^2}{k_{so}T_o}\exp(-\theta)\left[\rho\frac{d}{d\rho}\left(\frac{V}{\rho}\right)\right]^2=0 \qquad (A9)$$

The parameter $\beta\frac{\mu_o\omega_1^2R_1^2}{k_{so}T_o}$, known as the Brinkman number, was typically less than 10^{-4} in the experiments, thus allowing the effect of viscous dissipation to be ignored. Equation (A9) can therefore be approximated by

$$\frac{1}{\rho}\frac{d}{d\rho}\left[\left(1+\frac{\Delta k}{k_{so}}\right)\rho\frac{d\theta}{d\rho}\right]=0 \qquad (A10)$$

or

$$\left(1+\frac{\Delta k}{k_{so}}\right)\rho\frac{d\theta}{d\rho}=C_1=\text{constant} \qquad (A11)$$

The constant C_1 can be obtained from the boundary condition (A6a)

$$C_1=-\frac{q\beta R_1}{T_o k_{so}} \qquad (A12)$$

By solving Equation (A5) together with the boundary conditions (A6b) and A6d), the temperature distribution in the glass can be shown to be

$$T(R_2)=\frac{qR_1}{kg}\ln\frac{(R_2+\delta R)}{R_2}+Tw=\text{constant} \qquad (A13)$$

For the sake of convenience, we put

$$T(R_2)=T_o \qquad (A14)$$

and the boundary condition for Equation (A11) becomes

$$\theta=0 \quad \text{at} \quad \rho=K \qquad (A15)$$

Previous analysis by Leal (1973) indicated that, for dilute suspensions undergoing simple shear,

$$\Delta k = c k_1 \phi Pe_1^d \tag{A16}$$

where c, d are constants and Pe_1 is the Peclet number given by

$$Pe = \frac{\bar{a}^2 \rho Cp G}{k_1} \tag{A17}$$

G is the velocity gradient

$$G = \left| \frac{dV_\theta}{dr} \right| = \omega_1 \left| \frac{dV}{d\rho} \right| \tag{A18}$$

If the curvature effects and variation of the viscosity due to the temperature gradient are ignored, the shear rate G is a constant and given by

$$G = \bar{G} = \frac{R_1 \omega_1}{R_2 - R_1} = \frac{\omega_1}{K - 1} \tag{A19}$$

K in Equation (A11) is therefore a constant, $\overline{\Delta k}$, and the equation can be solved readily

$$\left(1 + \frac{\overline{\Delta k}}{k_{so}}\right) \theta = \frac{q \beta R_1}{T_o k_{so}} \ln \frac{K}{\rho} \tag{A20}$$

Equation (A20) is, of course, identical to Equation (9) derived earlier. However, the velocity gradient, as calculated from Equation (A7) is a function of radial position:

$$G = \omega_1 \left|\frac{dV}{d\rho}\right|$$

$$= \omega_1 \left| 1 - \frac{1}{\int_1^K \frac{\exp\theta}{t^s}\, dt} \int_1 \frac{\exp\theta}{t^3}\, dt + \frac{\exp\theta}{\rho^2} \right| \qquad \text{(A21)}$$

$$= \omega_1 \, f\,(\theta(\rho),\rho)$$

where

$$f(\theta(\rho),\rho) = \left|\frac{dV}{d\rho}\right| .$$

Equation (A11) then becomes

$$\left[1 + \frac{ck_f}{k_{so}} \phi \left(\frac{a^2 C_p \rho \omega_1}{k_f}\right)^d [f(\theta(\rho),\rho)^d]\, \rho \frac{d\theta}{d\rho}\right] = c_1 \qquad \text{(A22)}$$

By defining an average Peclet number $\overline{Pe_1}$ as:

$$\overline{Pe_1} = \frac{a^2 C_p \rho}{k_1} \frac{\omega_1}{K - 1} ,$$

Equation (A22) becomes

$$[1 + h(f)^d]\, \rho \frac{d\theta}{dp} = c_1 \qquad \text{(A23)}$$

where

$$h = c \frac{k_1}{k_{so}} \phi \, \overline{Pe_1}^{\,d} \, (K - 1)^d = \frac{\Delta\bar{k}}{k_{so}} (K - 1)^d = \text{constant} \qquad \text{(A24)}$$

In the experiments, h was always smaller than 0.11. It is therefore reasonable to solve Equation (A23) via an asymptotic expansion of the form

$$\theta(\rho) = \theta_o(\rho) + h\theta_1(\rho) + O(h^2) \tag{A25}$$

The function $f(\theta(\rho),\rho)$ can also be expanded asymptotically with respect to h.

If we wrote

$$\exp\theta = \exp(\theta_o)\left(1 + O(h)\right) , \tag{A26}$$

the function $f(\theta(\rho),\rho)$ can be expressed as

$$f(\theta(\rho),\rho) = \left| 1 - \frac{1}{\int_1^k \frac{\exp\theta_o}{t^s}\,dt}\left[\int_1^\rho \frac{\exp\theta_o}{t^3}\,dt + \frac{\exp\theta_o}{\rho^2}\right] + O(h)\right| \tag{A27}$$

$$= f(\theta_o(\rho),\rho) + O(h)$$

Equation (A23) can now be expressed as

$$\left\{1 + h\left[f(\theta_o(\rho),\rho) + O(h)\right]^d\right\}\rho\,\frac{d\left[\theta_o + h\theta_1 + O(h^2)\right]}{d\rho} = c_1 \tag{A28}$$

By equating terms of equal order in h, we obtain

$$\rho\,\frac{d\theta_o}{d\rho} = c_1 \tag{A29}$$

$$\frac{d\theta_1}{d\rho} + \left[f(\theta_o(\rho),\rho)\right]^d\,\frac{d\theta_o}{d\rho} = 0 \tag{A30}$$

Higher-order terms will not be attempted as the term of interest here is the first correction due to nonzero values of h.

The boundary conditions are

$$\theta_m(K) = 0 \qquad m=0,1,... \tag{A31}$$

The solution to Equation (A29) is

$$\theta_0(\rho) = c_1 h_1 \frac{\rho}{K} \tag{A32}$$

The function $f(\theta_0,\rho)$ is therefore

$$f(\theta_0,\rho) = \frac{K^{c_1-2} - (c_1 - 1)\rho^{c_1-2}}{K^{c_1-2} - 1} \tag{A33}$$

and the Equation (A30) becomes

$$\frac{d\theta_1}{d\rho} + \frac{c_1}{\rho}\left[\frac{K^{c_1-2} - (c_1 - 1)\rho^{c_1-2}}{K^{c_1-2} - 1}\right]^d = 0 \tag{A34}$$

The value of d predicted by Leal's theory (1973) was 1.5. For reasons of generality, we will solve for the three cases of d = 1, 1.5 and 2 here.

For d = 1 and 2, θ_1 can be solved analytically:

$$\theta_1(\rho) = \frac{c_1}{K^{c_1-2} - 1}\left[K^{c_1-2} \ln\frac{K}{\rho} - \frac{c_1 - 1}{c_1 - 2}\left(K^{c_1-2} - \rho^{c_1-2}\right)\right] \quad \text{for d=1} \tag{A35}$$

and

$$\theta_1(\rho) = \frac{c_1}{\left(K^{c_1-2} - 1\right)^2}\left[K^{2(c_1-2)} \ln\frac{K}{\rho} - 2K^{c_1-2}\frac{c_1 - 1}{c_1 - 2}\left(K^{c_1-2} - \rho^{c_1-2}\right) + \frac{(c_1 - 1)^2}{2(c_1 - 2)}\left(K^{2(c_1-2)} - \rho^{2(c_1-2)}\right)\right] \quad \text{for d=2 .} \tag{A36}$$

Finally, by using Equations (A24) and (A25), we obtain the relationship between $\theta(1)$ and $\overline{\Delta k}$

$$\theta(1) = \theta_o(1) + h\theta_1(1) + O(h^2)$$
$$= \theta_o(1) + \frac{\overline{\Delta k}}{k_{so}} [(K - 1)^d \theta_o(1)] + O(h^2) \qquad \text{(A37)}$$

Equation (A37) can be used to evaluate the average increase in thermal conductivity $\overline{\Delta k}$ in terms of the measured $\theta(1)$, q and other parameters of the system:

$K = 1.2025$, $\beta = 0.925$, $k_{so} \simeq 6.8 \times 10^{-4}$ cal sec^{-1} cm^{-1} $^oC^{-1}$

$R_1 = 4.943$ cm, $T_o = 25.0^oC$

$q = \frac{EI}{2\pi R_1 Lf}$ where $L = 10$ cm, $f = 4.184$ watts sec cal^{-1} .

For the largest temperature differece in the gap of about 6^oC used in the experiments, the applied voltage E and current I were approximately:

$E = 10.01$ volts, $I = 0.5619$ amp.

Substituting Equations (A32), (A35) or (A36) and the above values into Equation (A37), yields:

$$\theta(1) = 0.2674 - 0.2694 \frac{\overline{\Delta k}}{k_{so}} + O(h^2) \qquad \text{for } d = 1 \qquad \text{(A38)}$$

$$\theta(1) = 0.2674 - 0.2769 \frac{\overline{\Delta k}}{k_{so}} + O(h^2) \qquad \text{for } d = 2 \qquad \text{(A39)}$$

When d = 1.5, Equation (A34) has to be solved numerically. For the values given above, the solution is

$$\theta(1) = 0.2674 - 0.2726 \frac{\overline{\Delta k}}{k_{so}} + O(h^2) \tag{A40}$$

When the curvature effects were neglected and the velocity gradient was assumed to be constant, the equivalent expression, as given by Equation (A20), becomes

$$\left(1 + \frac{\overline{k}}{k_{so}}\right) \theta(1) = \frac{q\beta R_1}{T_o k_{so}} \ln K \tag{A41}$$

Since $\overline{\Delta k}$ is typically much smaller than k_{so}, a comparison between Equations (A38), (A39), (A40) and (A41) can be made by approximating Equation (A41) by:

$$\theta(1) \simeq \left(\frac{q\beta R_1}{T_o k_{so}} \ln K\right)\left(1 - \frac{\overline{\Delta k}}{k_{so}}\right)$$

$$= 0.2674 \left(1 - \frac{\overline{\Delta k}}{k_{so}}\right) \tag{A42}$$

Equation (A42) is virtually identical to Equations (A38), (A39) and (A40). Thus, for the conditions of the experiments, it is adequate to use the results obtained from the analysis with the assumptions of constant viscosity and thermal conductivity. The error in the $\overline{\Delta k}$ evaluated by this method is not more than about 4%.

APPENDIX B: The Effect of Natural Convection to Heat Transfer

In the experiments, the transfer of heat between the two concentric cylinders was realized by maintaining a temperature difference between the two cylinders. It was expected that the temperature gradient would have created convective motion as a result of buoyancy forces. The free convection generated would have influenced the temperature field as well as the motion of the particles in the suspensions. An estimation of the effect of this free convection to heat transfer is presented here.

Batchelor (1954) analyzed the problem of heat transfer by free convection across a closed cavity between vertical boundaries at different temperatures. Although unable to solve the general problem analytically, Batchelor (1954) was able to estimate the effects in some limiting situations. The results obtained by Batchelor (1954) are applicable to the concentric Couette flow apparatus used in this study if the curvature effects are neglected. Furthermore, only the velocity and temperature profiles in the central, or test, region of the apparatus, which was about seven centimeters from the ends, need to be considered. Batchelor (1954) showed that in the region a distance $z \approx \frac{Ra(R_2 - R_1)}{1000}$ from the ends, the temperature distribution was simply the linear distribution resulting from the purely conductive transfer of heat. Here, Ra is the Rayleigh number defined by

$$Ra = \frac{(R_2 - R_1)^3 g\, b\, C_p \rho}{\nu k} [T(R_1) - T(R_2)] \qquad (B1)$$

where b is the coefficient of volume expansion of the suspension, g the gravitational constant, and ν the kinematic viscosity. The Rayleigh number defined above is relevant to the case of liquids and thus has a

different appearance from that used by Batchelor (1954), which was for the case of gases. For the Ucon oil, used as the suspending fluid in the experiments and for the maximum temperature drop of about $6^{o}C$, the Rayleigh numbers for the experiments were about 2.3×10^{3}. Thus, at distances further from the ends than about 2.3 cm, the purely conductive, linear temperature field was established. The suspension in the central, test region was therefore clearly in the region of linear temperature profile.

Again, using the results of Batchelor (1954), the fluid motion as a result of buoyancy effects due to the temperature distribution in this central core was the purely vertical velocity distribution

$$V_z \approx \frac{kRa}{12 \rho C_p (R_2 - R_1)} (2x^3 - 3x^2 + x) \text{ cm sec}^{-1} \qquad (B2)$$

where $x = \frac{r - R_1}{R_2 - R_1}$, the normalized distance from the wall of the inner cylinder. For the experimental conditions used, the above expression becomes:

$$V_z = 0.28(2x^3 - 3x^2 + x) \text{ cm sec}^{-1} \qquad (B3)$$

This motion was orthogonal to the temperature gradient, and would have contributed an additional component of the local vorticity (or rotation of the suspended particles). The disturbance velocity and temperature fields associated with this flow would have led to an enhancement of the radial heat flux. This enhancement was expected to be a function of the local Peclet number, Pe_{NC}, due to the natural convection. This Peclet

number was in turn proportional to the shear rate, G_{NC}, generated by the convective motion. An estimation of this shear rate would therefore provide an estimation of the enhancement to conduction due to the natural convection.

The shear rate G_{NC} can be obtained by differentiating the velocity field V_z given above:

$$G_{NC} \approx 1.7(x^2 - x + 0.167) \text{ sec}^{-1} \tag{B4}$$

G_{NC} has a maximum value of 0.28 sec^{-1} at the walls, a minimum value of -0.14 sec^{-1} at the midpoint $x = \frac{1}{2}$ and vanishes at the points $x = 0.2113$ and $x = 0.7887$. On the other hand, the average shear rate generated by the rotation of the inner cylinder was always greater than 2.59 sec^{-1}. Thus, the motion due to natural convection would have a negligible effect to the heat transfer under all experimental conditions.

Finally, the heat flux due to natural convection must be small relative to that by 'conduction'. This convective heat flux, q_{cv}, can be estimated from the Nussett number N obtained by Batchelor (1954),

$$q_{cv} = \frac{k_1(T_1 - T_o)N}{L} \tag{B5}$$

with N given by the expression

$$N \approx \frac{(2\gamma - 1)}{720} \text{ Ra} \tag{B6}$$

Here, γ is a function of Ra which approaches unity as $\text{Ra} \to \infty$. For the conditions encountered in the experiments, the maximum q_{cv} was approximately 1.5×10^{-4} cal cm^{-2} sec^{-1}, compared to the bulk heat flux due to

conduction of 8.7×10^{-3} cal cm^{-2} sec^{-1} under the same experimental conditions. The effect of q_{cv} was therefore negligible.

APPENDIX C: An Estimation of the Effect of a Skimming Layer to the Velocity and Temperature Fields.

For a suspension undergoing non-uniform bulk flow, there exists a particle-free layer, a skimming layer, near the wall of the flow channel due to geometric exclusion. Since the viscosity depends on the concentration of the dispersed phase, the presence of the skimming layer would affect the velocity field and therefore affect the velocity gradient. A change in the velocity gradient would change the local Peclet number which in turn would affect the augmentation in thermal conduction. The temperature field would also be affected. The effect of a skimming layer, which would likely be more important at higher concentrations of the dispersed phase, was not considered in the derivation of the governing equations of the Couette flow apparatus. An estimation of the effect is presented here.

As shown in Appendix A, the effect of curvature in the velocity field was unimportant to the measurement of augmentation in thermal conductivity in the experment. Instead of considering the problem of heat conduction in a suspension undergoing flow in a concentric Couette flow device, it is sufficient to consider the problem in one dimension.

I. The Effect of a Skimming Layer to the Velocity Field

Within a particle-free skimming layer, the viscosity is essentially that of the suspending fluid, μ_f. Between the two skimming layers adjacent to each wall is the suspension with a viscosity of μ_s.

Since curvature effects were shown to be unimportant macroscopically, the problem can be reduced to one dimension. An illustration of the

problem is given in Figure D1. The thickness of the skimming layers near the moving and stationary walls are denoted as δ_1 and δ_2, respectively. Between the two skimming layers is the suspension of thickness $[(R_2 - R_1) - (\delta_1 + \delta_2)]$.

The governing equation for the velocity field is

$$\frac{d^2V_{zj}}{dx^2} = 0 \qquad j = I,II,III \; . \tag{C1}$$

V_{zj} is the z-component velocity in region j. The boundary conditions are:

$$V_{z_I}(0) = R_1\omega_1$$

$$V_{z_{III}}(R_2 - R_1) = 0$$

$$V_{z_I} = V_{z_{II}}\Big|_{x=\delta_1}$$

$$\mu_f \frac{dV_{z_I}}{dx} = \mu_s \frac{dV_{z_{II}}}{dx}\Bigg|_{x=\delta_1} \tag{C2}$$

$$V_{z_{II}} = V_{z_{III}}\Big|_{x=R_2-R_1-\delta_2}$$

$$\mu_s \frac{dV_{z_{II}}}{dx} = \mu_f \frac{dV_{z_{III}}}{dx}\Bigg|_{x=R_2-R_1-\delta_2}$$

The solutions to the above system of equations are:

$$V_{z_j}(x) = a_jx + b \qquad j = I,II,III \; . \tag{C3}$$

The shear rates a_j, the quantities of interest in this analysis, are given by:

$$a_I = a_{III} = \frac{\mu_s}{\mu_f} a_{II}$$

$$a_{II} = -\frac{\omega_1}{(K-1)} \cdot \frac{1}{1 + \left(\frac{\mu_s}{\mu_f} - 1\right)\left(\frac{\delta_2 + \delta_2}{R_2 - R_1}\right)} \tag{C4}$$

where $K = \frac{R_2}{R_1}$.

Since the skimming layers are caused by geometric exclusion, the thicknesses of the skimming layers are therefore of the same order as the size of particles in the suspension:

$$\delta_1, \delta_2 << R_2 - R_1$$

The results can then be further simplified:

$$a_{II} \simeq -\frac{\omega_1}{K-1}\left[1 - \frac{(\delta_1 + \delta_2)}{R_2 - R_1}\left(\frac{\mu_s}{\mu_f} - 1\right)\right] \tag{C5}$$

Without the skimming layers, the shear rate is $-\frac{\omega_1}{K-1}$, the same as that used in the data analysis. With the presence of the thin skimming layers, the correction to the shear rate is

$$-\left(\frac{\delta_1 + \delta_2}{R_2 - R_1}\right)\left(\frac{\mu_s}{\mu_f} - 1\right) .$$

At the highest volume concentration of 25% of the dispersed phase used in the suspension, the ratio $\frac{\mu_s}{\mu_f}$ was about 2 (Figure 5). The diameter

of the largest particles used was about 82 times smaller than the gap width, $(R_2 - R_1)$. The correction to the shear rate is therefore small for this worst case.

II. The Effect of a Skimming Layer to the Temperature Field

The effect of the skimming layer on heat transfer can be estimated by an analysis analogous to the above calculation. The thermal conductivity of the skimming layer is essentially that of the suspending fluid, k_f. The thermal conductivity of the suspension between the skimming layers is k_s, which includes the contribution due to the presence of the particles and the shear flow. The temperature difference across the entire sample is therefore given by

$$\begin{aligned} \Delta T &= T(R_2) - T(R_1) \\ &= q_1 \left[\frac{1}{k_f} (\delta_1 + \delta_2) + \frac{(R_2 - R_1) - (\delta_1 + \delta_2)}{k_s} \right] \\ &= q_1 \frac{(R_2 - R_1)}{k_s} \left[1 + \frac{\delta_1 + \delta_2}{R_2 - R_1} \left(\frac{k_s}{k_f} - 1 \right) \right] \end{aligned} \tag{C6}$$

The thermal conductivity k_s can be written as a sum of the thermal conductivity of the suspending fluid, k_f, and the contributions from the particles and the shear Δk:

$$k_s = k_f + \Delta k \quad .$$

Therefore, the temperature difference can be expressed as:

$$\Delta T = q_1 \frac{(R_2 - R_1)}{k_s} \left[1 + \left(\frac{\delta_1 + \delta_2}{R_2 - R_1}\right) \frac{\Delta k}{k_f}\right] \qquad (C7)$$

The correction to the temperature field is therefore equal to

$$\left(\frac{\delta_1 + \delta_2}{R_2 - R_1}\right) \Delta k \quad .$$

Equivalently, the correction to the measured Δk is $\left(\frac{\delta_1 + \delta_2}{R_2 - R_1}\right)$. Using the same argument as presented in section I, this correction is negligible.

The above calculation demonstrates that the skimming layers are unimportant as long as they are thin compared to the gap width $(R_2 - R_1)$. The experimental data indicated this to be the case as no significant difference in the augmentation to thermal conductivity was observed for the different sizes of the particles used in the actual experiments.

APPENDIX D: The Rheological Properties of Suspensions of Rigid Spherical Particles

Experimental and theoretical work on the rheological properties of suspensions in recent years have demonstrated that suspensions have to be treated as non-Newtonian fluids. The rheological properties of suspensions are influenced by the concentration, shape and size distribution of the particles, the presence of electrical charges, Brownian motion and the type of flow being experienced. Detailed discussions of the origin and importance of these various effects can be found in several recent reviews (Batchelor, 1974; Jinescu, 1974; Brenner, 1972; Jeffrey and Acrivos, 1976). The importance of these non-Newtonian effects as relevant to the suspensions and experimental conditions used in this study will be considered here.

It is well known that dilute suspensions of rigid spheres are Newtonian at low particle Reynolds numbers. By assuming that the particles are far enough apart to be treated independently of each other and that the flow around each particle is described by the equations of motion with inertia neglected, Einstein (see Einstein, 1956)) obtained the relation

$$\mu_s = \mu_f\left(1 + \frac{5}{2}\phi\right) \qquad \text{(D1)}$$

Here, μ_s is the effective viscosity of the suspension, μ_f the viscosity of the suspending fluid, and ϕ the volume fraction of suspended particles.

The nonhydrodynamic forces consist of Brownian forces, electrical forces arising from charges on the particles and London-van der Waals forces. Brownian forces are important only to small particles that are typically submicron in size. Since all the spherical particles used in

this study were more than 30 microns in diameters, the Brownian forces should be unimportant. The same is true of the effect of electrical charges because the typical Debye length, a measure of the thickness of the layer of charge surrounding each particle and opposite to the charge on the particle, is on the order of 1 micron. The relatively large sizes of the particles used in the experiments made the electroviscous effects unimportant. The weak attractive London-van der Waals forces, because of their very short range, should also be unimportant for the moderate concentrations of suspended particles ($\phi \leq 0.25$) used.

When the concentration of the suspended particles increases and the particles do interact with each other, the result obtained by Einstein (Equation D1) no longer holds. Einstein's calculation is the first, $O(\phi)$ contribution in an integer power series representation for the shear viscosity:

$$\mu_s = \mu_f \left(A\phi + B\phi^2 + C\phi^3 + \ldots\right) \qquad (D1)$$

in which the first term $\frac{5}{2}\phi$ is due to the effects of the non-interacting particles. The next correction, of order ϕ^2, involves hydrodynamic interactions between two particles and requires knowledge of the statistical distribution of relative particle location (Batchelor and Green, 1972). This statistical distribution depends strongly on the flow and other forces such as translational Brownian motion and inertia effects on the particles. As a result, the effective viscosity is not a unique material property of the suspension and is in general non-Newtonian. For this reason, the viscosities of the suspensions used in the experiments were measured in a Stormer Viscometer. The Stormer Viscometer, a rotating cup device capable

of creating rotational shear flows similar to those of the Couette flow device used in this study, was operated at shear rates and temperatures encountered in the experiments. For shear rates up to about 40 sec^{-1}, with the corresponding particle Reynolds number no more than 10^{-3}, the effective viscosity was virtually independent of shear rate and size of the particles at any of the concentrations used. These observations were in agreement with the experimental results of Krieger (1972). At the higher concentrations used, deviations from Einstein's result was substantial. The relative viscosity, $\mu_r = \mu_s/\mu_f$, at $\phi = 0.25$ was measured to be about 2.

Nomenclature

$\bar{a}$ = average radius of particles dispersed in suspension.

C_p = heat capacity of Ucon Oil.

E = voltage applied across test heater.

δE = error in the measured E.

G = local shear rate.

$\bar{G}$ = radially average shear rate.

I = electrical current passing through test heater.

δI = error in the measured I.

k = thermal conductivity.

k_s = effective thermal conductivity of suspension

k_{so} = effective thermal conductivity of stationary suspension measured.

δk = error in the effective thermal conductivity measured.

Δk = contribution to the effective thermal conductivity from simple shear.

k_1 = thermal conductivity of suspending fluid.

k_2 = thermal conductivity of dispersed phase.

k_g = thermal conductivity of outer glass cylinder.

K = R_2/R_1.

L = length of test heater.

Pe_1 = Peclet number based on the radius of particle and thermal properties of the suspending fluid = $\frac{\rho C_p G \bar{a}^2}{k}$.

q = heat flux per unit area.

r = radial position as measured from the axis of the cylinders.

R = relative augmentation in thermal conductivity = $\Delta k/\phi k_1$.

R_1 = radius of inner cylinder.

R_2 = inner radius of outer cylinder.

δR_1 = thickness of outer cylinder.

T = temperature field.

Tw = temperature of conditioning water.

δTw = error in measured Tw

ΔT = temperature difference across the annular gap in the apparatus.

V_θ = velocity in θ-direction.

$V = \frac{V_\theta}{\omega_1 R_1}$ = dimensionless velocity in θ-direction.

α = k_2/k_1.

β = empirical constant used in the correlation $\mu = \mu_o \exp[-\beta(T-T_o)/T_o]$.

γ = $(\alpha - 1)/(\alpha + 2)$.

ϕ = volume fraction of dispersed phase.

ρ = $\frac{r}{R_1}$ = dimensionless radial position.

ρ_f = density of test fluid.

θ = $\beta(T - T_o)/T_o$.

θ_k = $\beta[T(R_2) - T_o]/T_o$.

μ_o = viscosity of suspension at T_o .

μ_f = viscosity of suspending fluid.

μ_s = viscosity of suspension.

ω_1 = rotational speed of inner clyinder.

References

Batchelor, G. K., 'Heat Transfer by Free Convection Across a Closed Cavity between Vertical Boundaries at Different Temperatures". Quant. Appl. Math. 12, pp. 209-233, 1954.

Batchelor, G. K., 'Transport Properties of Two-Phase Materials with Random Structure', Ann. Rev. Fluid Mech. 6, pp. 227-255, 1974.

Batchelor, G. K., Green, J. T., 'The Determination of the Bulk Stress in a Suspension of Spherical Particles to Order C^2', J. Fluid Mech. 56, pp. 401-427, 1972.

Brenner, H., 'Suspension Rheology', in Progressive Heat and Mass Transfer, Vol. 5, Pergamon Press, Oxford, England, W. R. Schowalter, ed., 1972.

Chung, Y-C., PhD Thesis, California Institute of Technology, 1979.

Einstein, A., 'A New Determination of Molecular Dimensions', contained in Investigations on the Theory of Brownian Movement, R. Furth (Ed.), pp. 36-62, Dover Publications, 1956.

Ho, B. P., Leal, L. G., 'Inertial Migration of Rigid Spheres in Two-Dimensional Unidirectional Flows', J. Fluid Mech. 65, pp. 365-400, 1974.

Jeffrey, D. J., 'Conduction through a Random Suspension of Spheres', Proc. Roy. Soc. (London) A 335, pp. 355-367, 1973.

Jeffrey, D. J., 'Group Expansions for the Bulk Properties of a Statistically Homogeneous, Randon Suspension', Proc. Roy. Soc. (London), A 338, pp. 503-516, 1974.

Jeffrey, D. J., Acrivos, A., 'The Rheological Properties of Suspensions of Rigid Particles', AIChE J. 22, pp. 417-432, 1976.

Jimeseu, V. V., 'The Rheology of Suspensions', Intern. Chem. Eng. 14, pp. 397-420, 1974.

Krieger, I. M., 'Rheology of Monodisperse Lattices', Adv. Colloid Interface Sci. 3, 111-136, 1972.

Leal, L. G., 'On the Effective Conductivity of a Dilute Suspensions of Spherical Drops in the Limit of Low Particle Peclet Number', Chem. Eng. Comm. 1, 21-31, 1973.

Maxwell, J. C., 'Electricity and Magnetism', 1st ed., Oxford: Claredon Press, 1873.

McMillen, T. J., PhD Thesis, California Institute of Technology, 1976.

McMillen, T. J., Leal, L. G., 'The Effect of Deformation on the Effective Conductivity of a Dilute Suspension of Drops in the Limit of Low Particle Reynolds Number', Int. J. Multiphase Flow 2, pp. 105-112, 1975.

Nahme, R., 'Beiträge zur hydrodynamischen Theorie des Lagerreibung', Ingr.-Arch. 11, pp. 191-209, 1940.

Nir, A., Acrivos, A., 'The Effective Thermal Conductivity of Sheared Suspensions', J. Fluid Mech. 78, pp. 33-40, 1976,

Rocha, A., Acrivos, A., 'On the Effective Thermal Conductivity of Dilute Dispensions', Quant. J. Mech. Appl. Math. 26, pp. 217-233, 1973.

Segre, G., Silberberg, A., 'Behavior of Macroscopic Rigid Spheres in Poiseuille Flow. Part 2. Experimental Results and Interpretation', J. Fluid Mech. 14, pp. 136-157, 1962.

Taylor, G. I., 'Stability of a Viscous Liquid Contained between Two Rotating Cylinders', Phil. Trans. A 223, pp. 289-343, 1932.

Union Carbide, 'Ucon Fluids and Lubricants', 1971.

List of Tables

Empire Correlations for Relative Augmentation $R = CPe_1^d$ as a Function of ϕ and Pe_1:

Table II: For the case $\bar{a} = 17.3$ μm, $\Delta T \approx 2^oC$

Table IIIa: For the case $\bar{a} = 26.7$ μm, $\Delta T \approx 2^oC$

Table IIIb: For the case $\bar{a} = 26.7$ μm, $\Delta T \approx 6^oC$

Table IV: For the case $\bar{a} = 61$ μm, $\Delta T \approx 2^oC$

Table II

ϕ	Range of Pe_1	C	d
0.01	0.0270 - 0.102	29.9	1.91
0.02	0.0206 - 0.100	16.3	1.58
0.05	0.0113 - 0.100	21.3	1.64
0.10	0.0119 - 0.111	18.6	1.66
0.15	0.0122 - 0.103	20.4	1.78
0.20	0.0128 - 0.107	11.4	1.74
0.25	0.0132 - 0.109	12.1	1.84

$\Delta T = 2^{o}C$

$\bar{a} = 17.3\ \mu m$

$R = CPe_1^d$

Table IIIa

ϕ	Range of Pe_1	C	d
0.01	0.0428 - 0.266	10.6	1.62
0.05	0.0310 - 0.248	17.8	1.58
0.10	0.0459 - 0.249	10.1	1.48
0.15	0.0310 - 0.214	8.12	1.61

$\Delta T \simeq 2^{o}C$

$\bar{a} = 26.7\ \mu m$

$R = cPe_1^d$

Table IIIb

ϕ	Range of Pe_1	C	d
0.01	0.0309 - 0.214	8.83	1.34
0.02	0.0309 - 0.214	9.66	1.40
0.05	0.0309 - 0.214	13.7	1.48
0.10	0.0309 - 0.250	5.91	1.21
0.15	0.0309 - 0.250	8.33	1.58
0.20	0.0309 - 0.214	5.72	1.57
0.25	0.0309 - 0.233	6.65	1.62

$\Delta T \simeq 6^{o}C$

$a = 26.7\ \mu m$

$R = CPe_1^d$

Table IV

ϕ	Range of Pe_1	C	d
0.01	0.0786 - 0.476	5.41	1.12
	0.582 - 1.28	3.81	0.840
	0.786 - 1.28	4.06	0.957
0.02	0.0800 - 0.474	6.81	1.26
	0.579 - 1.28	4.63	0.886
	0.0800 - 1.28	4.98	1.08
0.05	0.0786 - 0.470	1.01	1.40
	0.568 - 1.26	4.83	0.748
	0.0786 - 1.26	5.44	1.04
0.09	0.0820 - 0.474	5.54	1.29
	0.572 - 1.17	2.66	0.555
	0.0820 - 1.17	3.11	0.955
0.15	0.0816 - 0.470	3.64	1.12
	0.568 - 1.16	2.09	0.638
	0.0816 - 1.16	2.33	0.861
0.20	0.0823 - 0.481	3.60	1.28
	0.566 - 1.17	1.87	0.754
	0.0823 - 1.17	2.13	0.987
0.25	0.0817 - 0.480	2.97	1.28
	0.582 - 1.08	1.69	0.871
	0.0817 - 1.08	1.88	1.016

$\Delta T \approx 2^{o}C$

$\bar{a} = 61\ \mu m$

$R = CPe_1^d$

Figure Captions

Figure 1: The experimental apparatus.

Figure 2: The electrical circuit and instruments used for the generation and measurement of heat flux.

Figure 3a,b: Photomicrographs of polystyrene latex spheres.

Figure 4: Resistance - temperature characteristics of test heater.

Figures 5-6: Measured thermal conductivity of Ucon Oil at various rotational speeds.

Figures 7-8: Measured thermal conductivity of stationary suspensions at different volume fractions.

Figures 9-15: Plots of relative augmentation in thermal conductivity R vs. Pe_1 at fixed volume fractions.

Appendix C

Figure D1: Schematic of skimming layers.

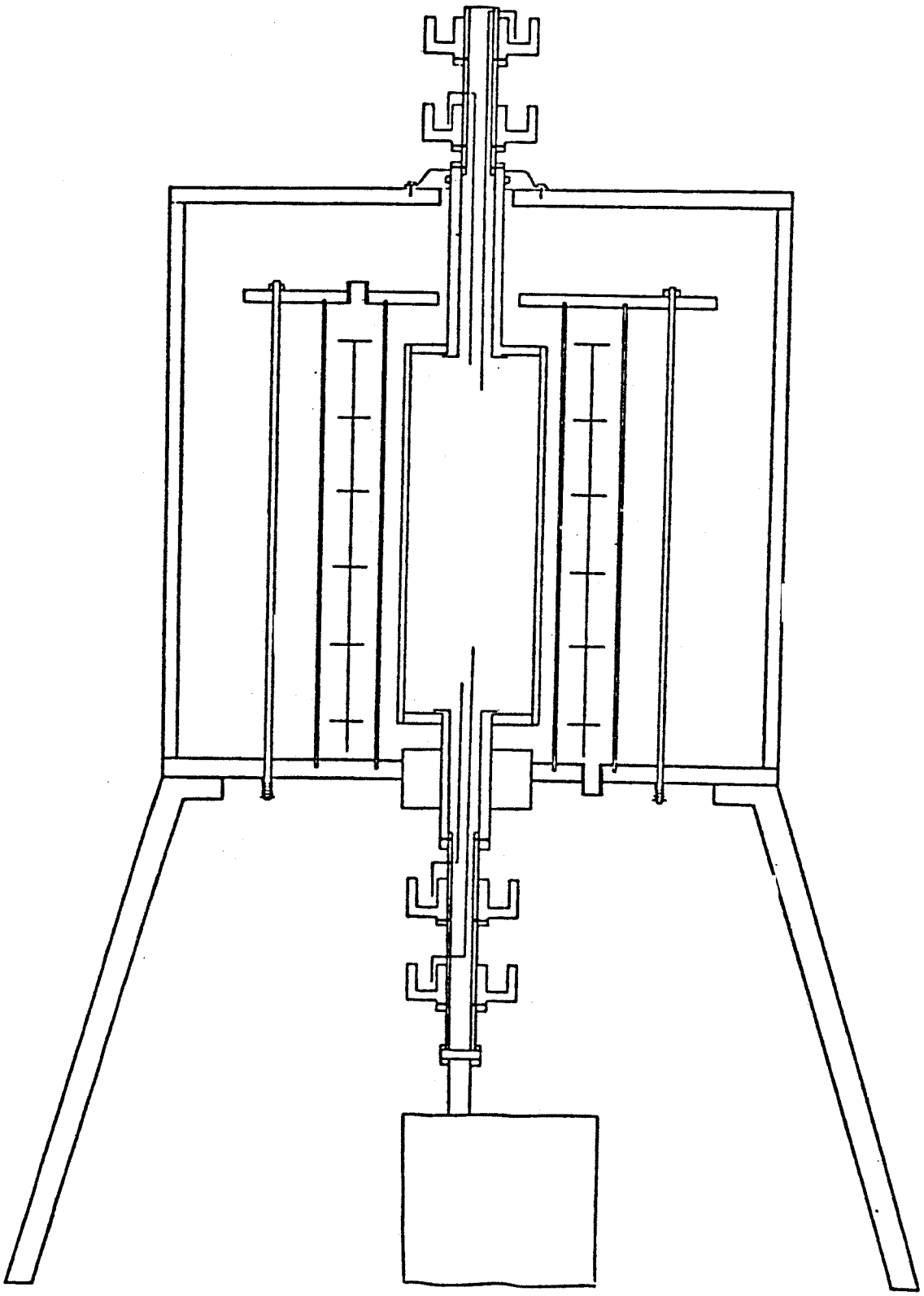

Figure 1: The Experimental Apparatus

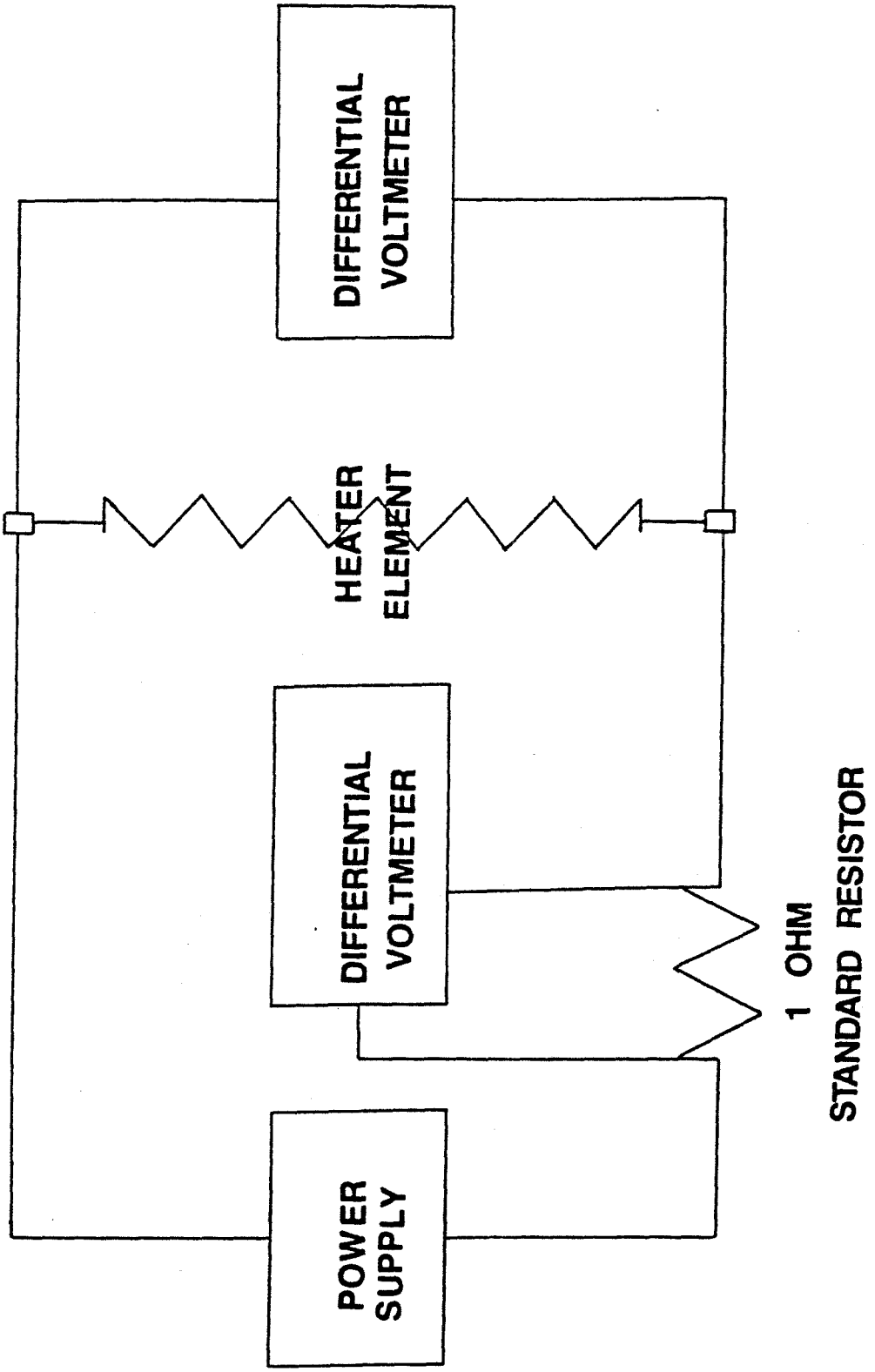

Figure 2: The Electrical Circuit

2a=53.4μm

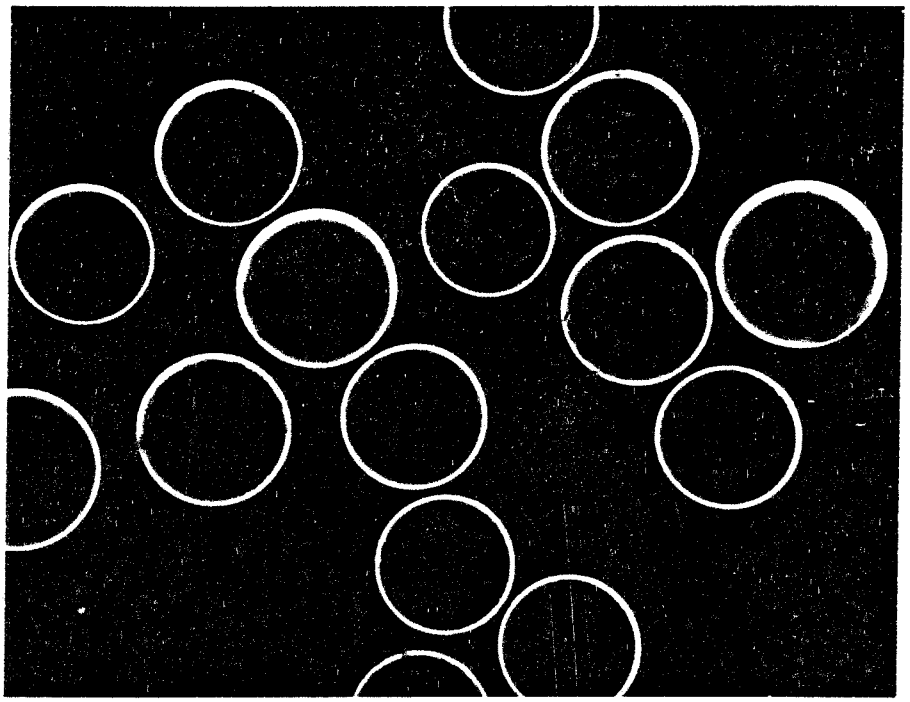

50μm

2a=122μm

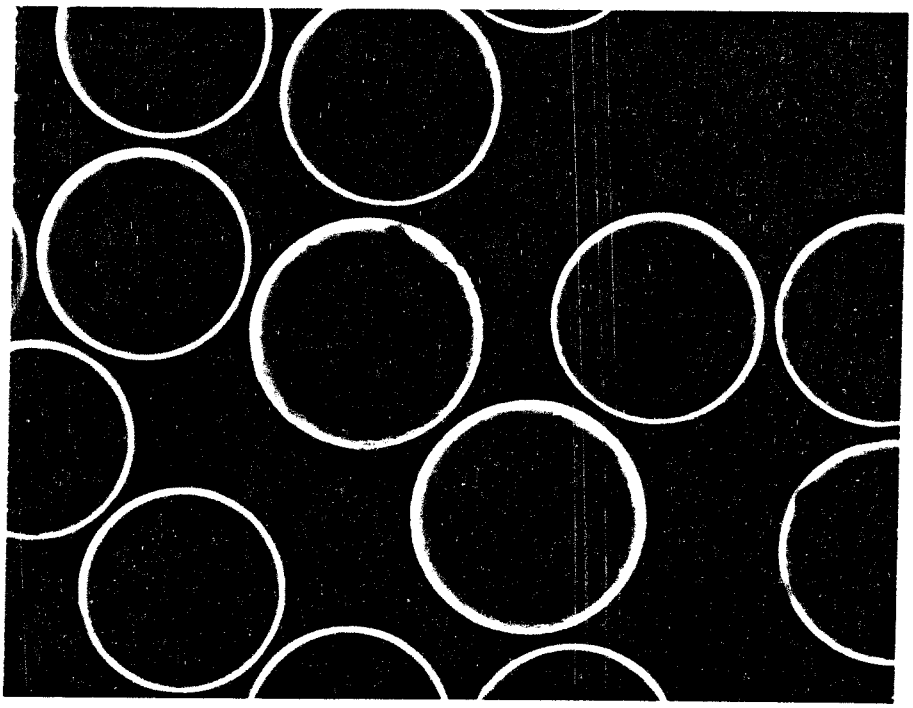

100μm

Fig. 3b: Dark Field Micrographs of Polystyrene Particles of Different Sizes

2a=34.6 m

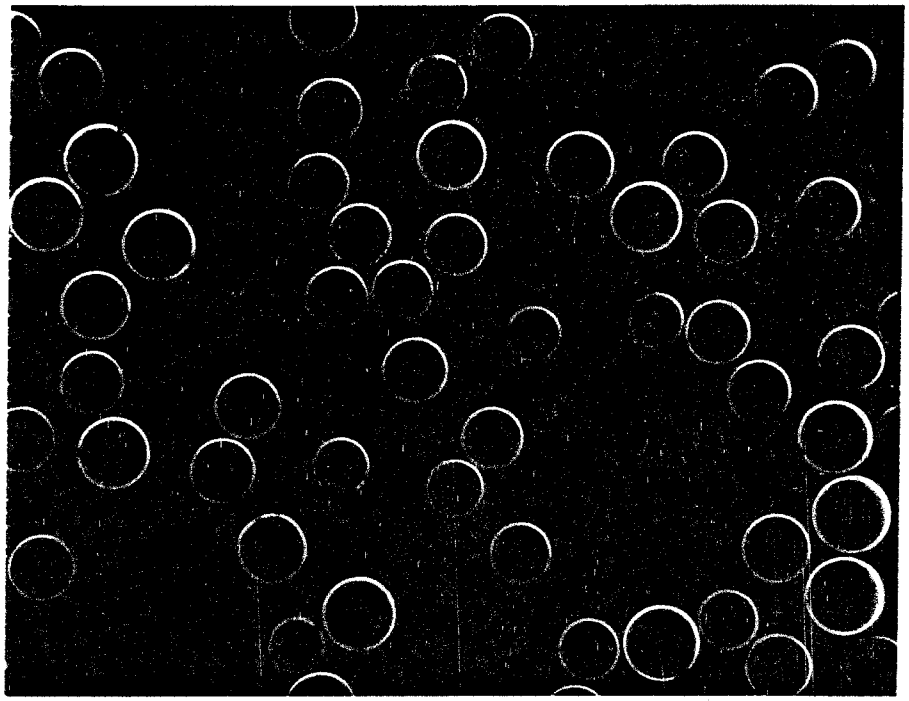

14 m

2a=34.6 m

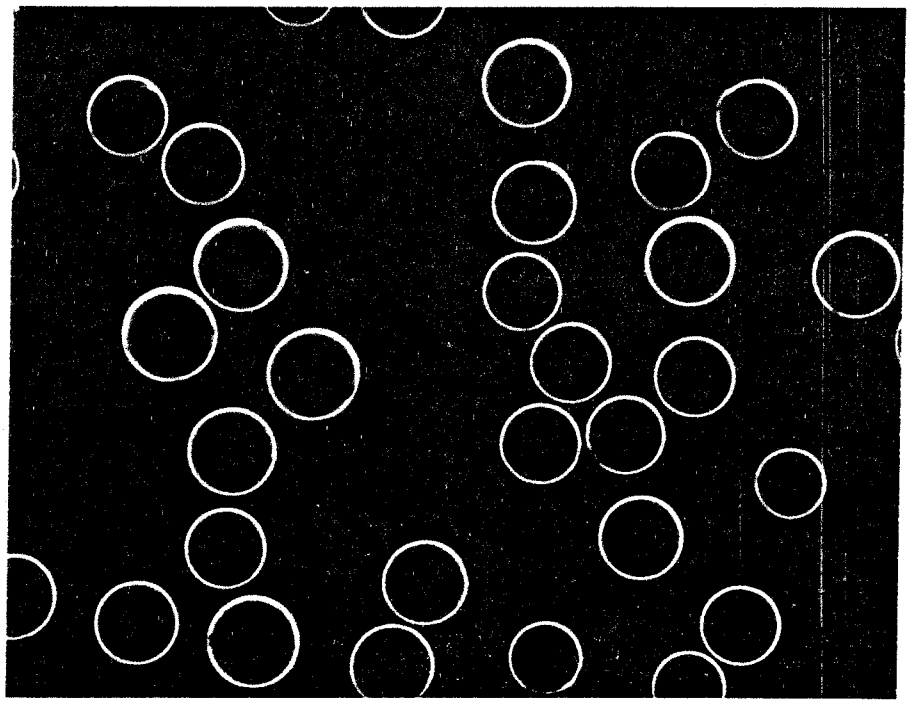

30 m

Fig. 3a: Dark Field Micrographs of Polystyrene Particles at Different Magnifications

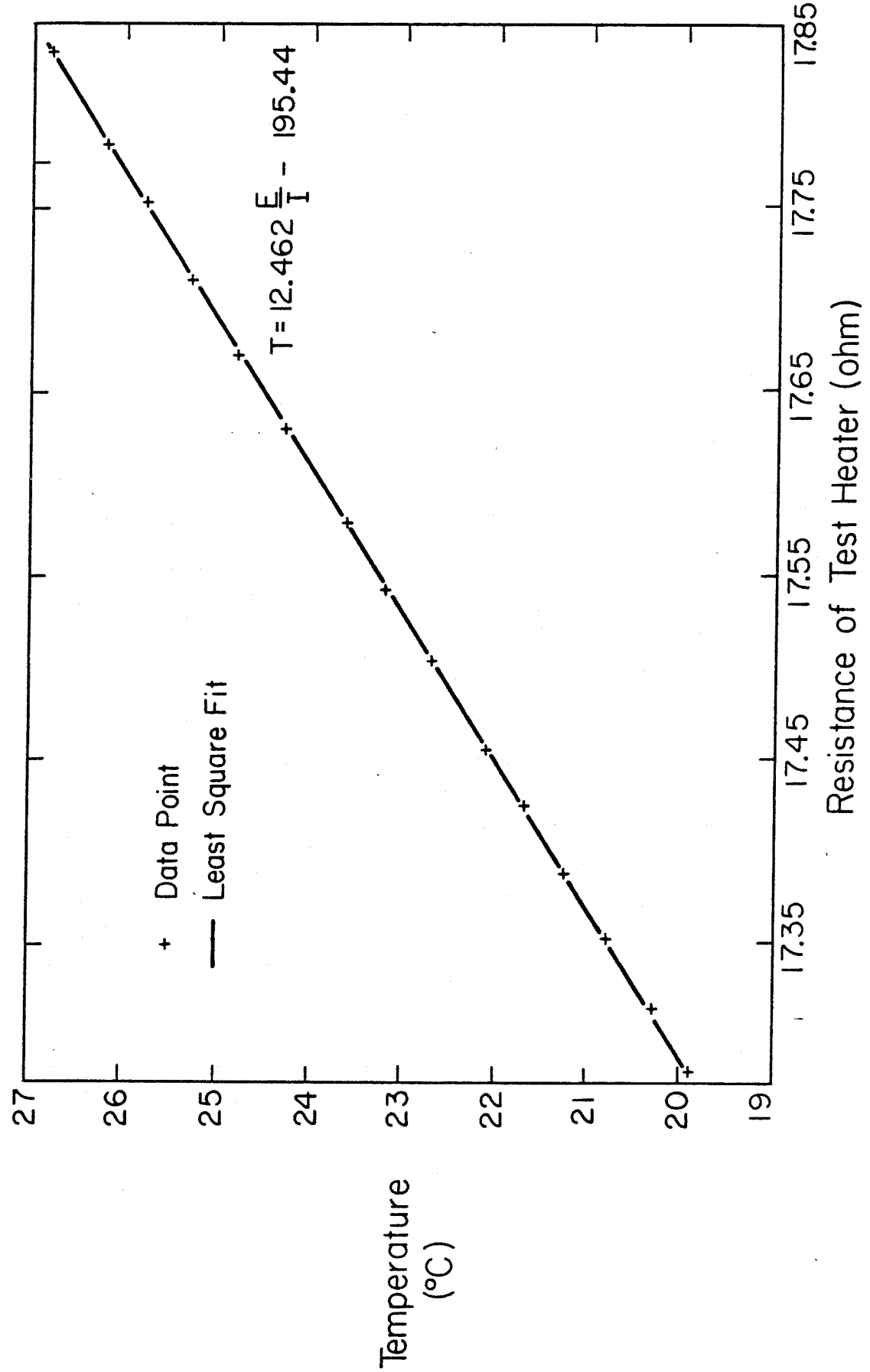
T= 12.462 E/I - 195.44
+ Data Point
— Least Square Fit
Temperature (°C)
Resistance of Test Heater (ohm)
27
26
25
24
23
22
21
20
19
17.35
17.45
17.55
17.65
17.75
17.85

Figure 4

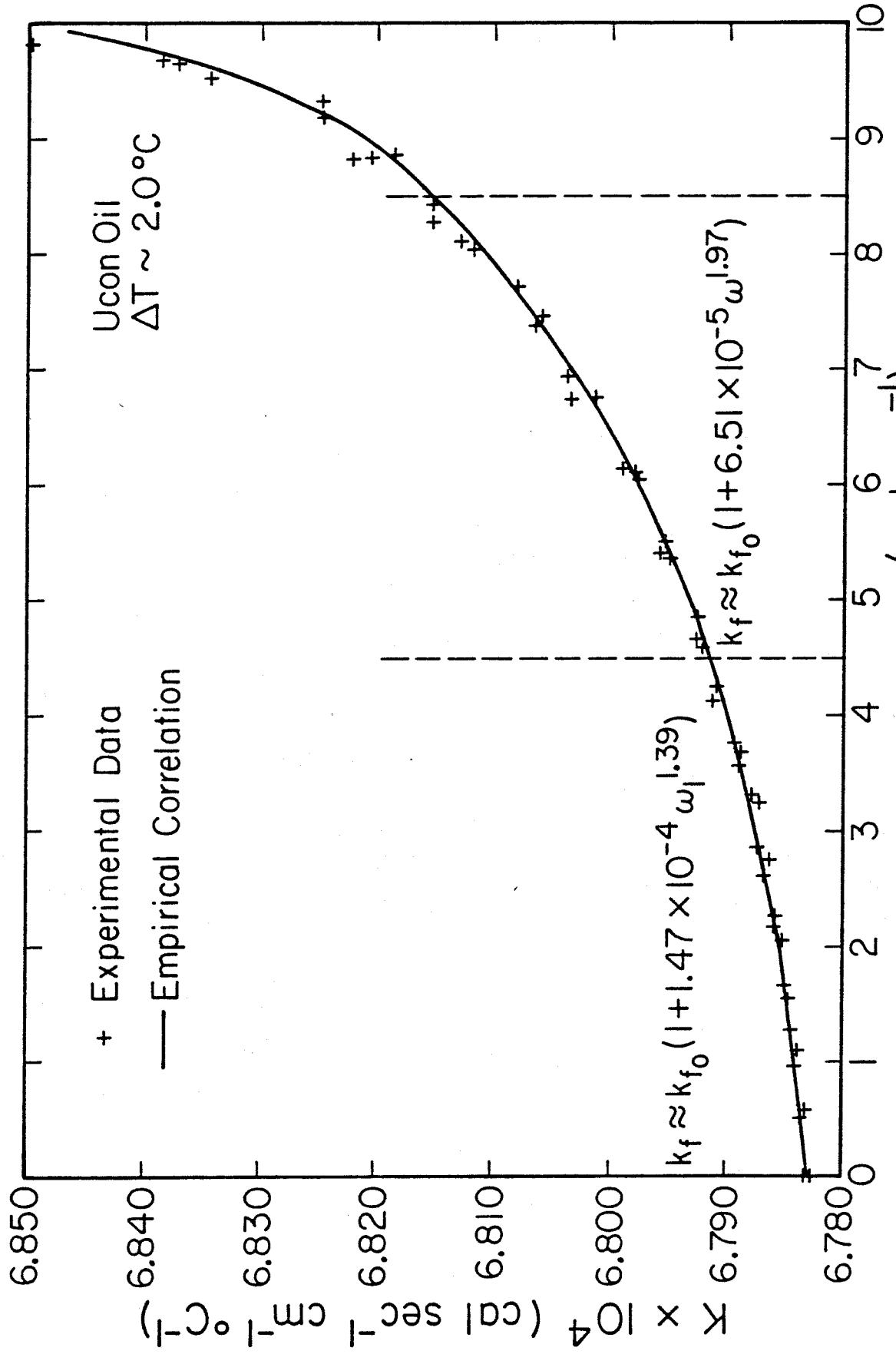
Ucon Oil
ΔT ~ 2.0°C
+ Experimental Data
— Empirical Correlation
$k_f \approx k_{f_0}(1+1.47\times10^{-4}\omega_1^{1.39})$
$k_f \approx k_{f_0}(1+6.51\times10^{-5}\omega^{1.97})$
K x 10⁴ (cal sec⁻¹ cm⁻¹ °C⁻¹)
6.850
6.840
6.830
6.820
6.810
6.800
6.790
6.780
0
1
2
3
4
5
6
7
8
9
10
ω₁ (rad sec⁻¹)

Figure 5

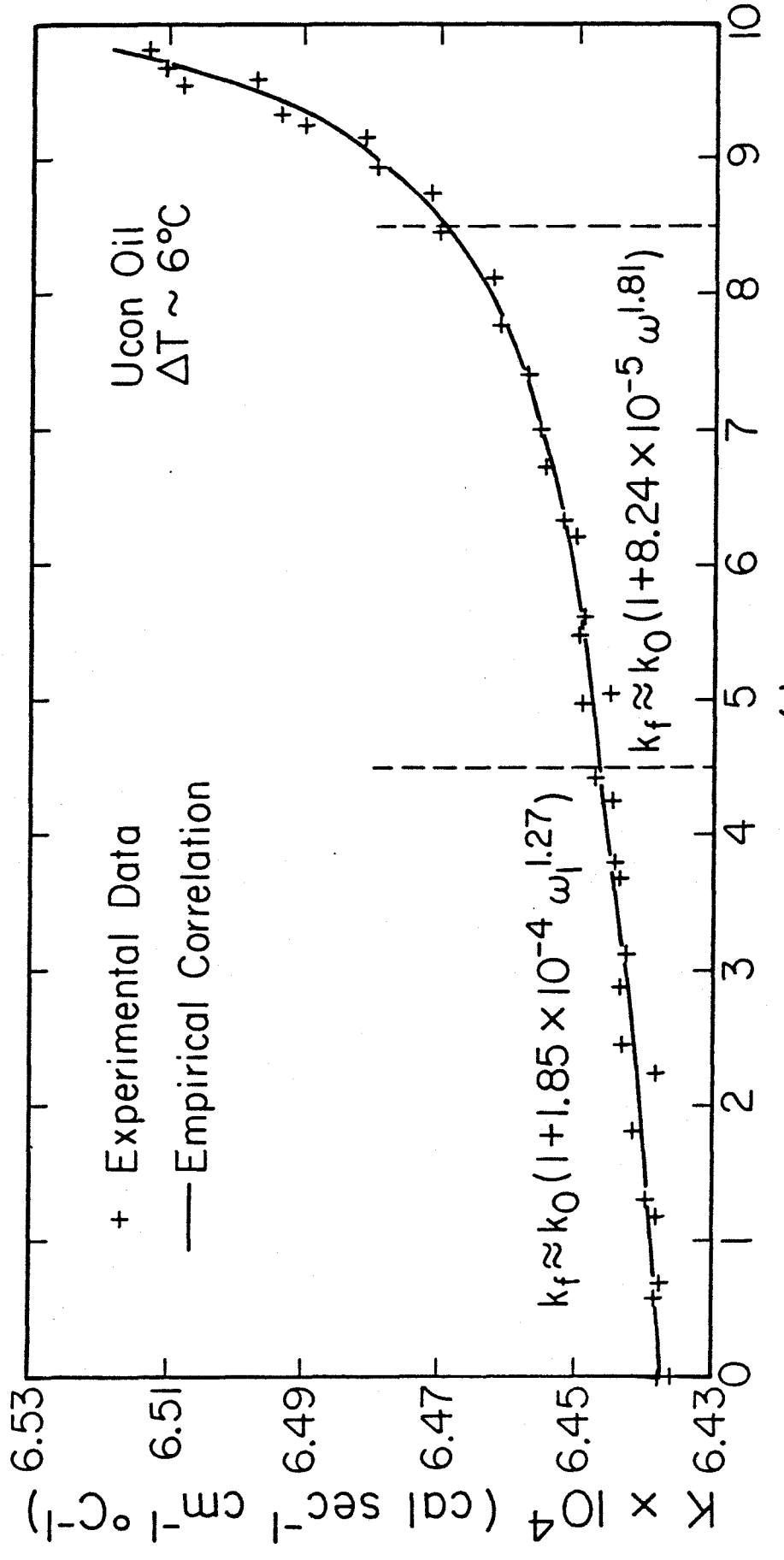
Ucon Oil
ΔT ~ 6°C
+ Experimental Data
— Empirical Correlation
$k_f \approx k_0(1+1.85\times10^{-4}\,\omega_1^{1.27})$
$k_f \approx k_0(1+8.24\times10^{-5}\,\omega^{1.81})$
ω_1
$K \times 10^4$ (cal sec^{-1} cm^{-1} °C^{-1})
6.53
6.51
6.49
6.47
6.45
6.43
0
1
2
3
4
5
6
7
8
9
10

Figure 6

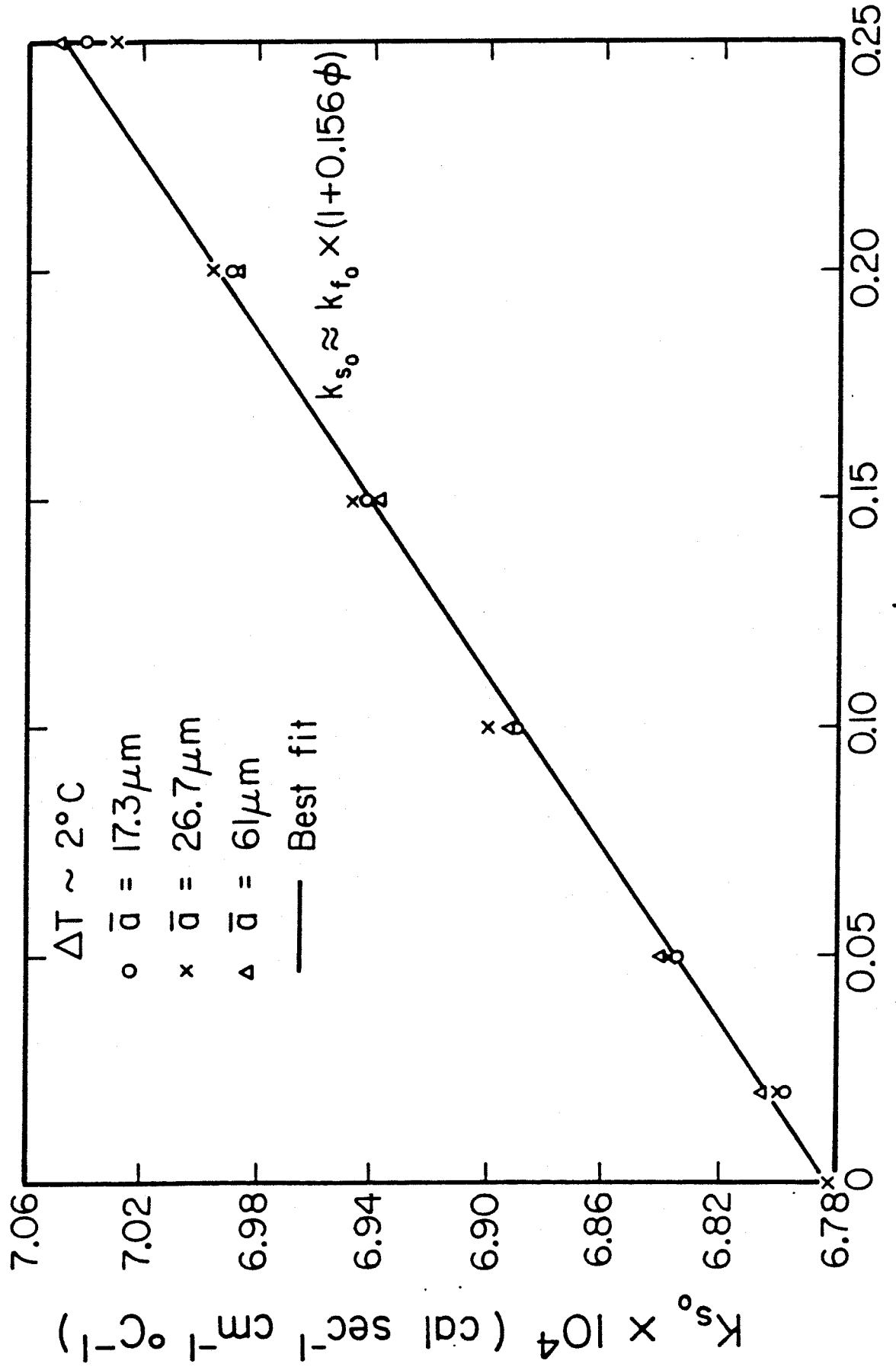
K_{s_o} x 10^4 (cal sec^{-1} cm^{-1} $^oC^{-1}$)
7.06
7.02
6.98
6.94
6.90
6.86
6.82
6.78
0
0.05
0.10
0.15
0.20
0.25
ϕ
$k_{s_o} \approx k_{f_o} \times (1+0.156\phi)$
$\Delta T \sim 2^oC$
o $\bar{a}$ = 17.3μm
x $\bar{a}$ = 26.7μm
Δ $\bar{a}$ = 61μm
Best fit

Figure 7

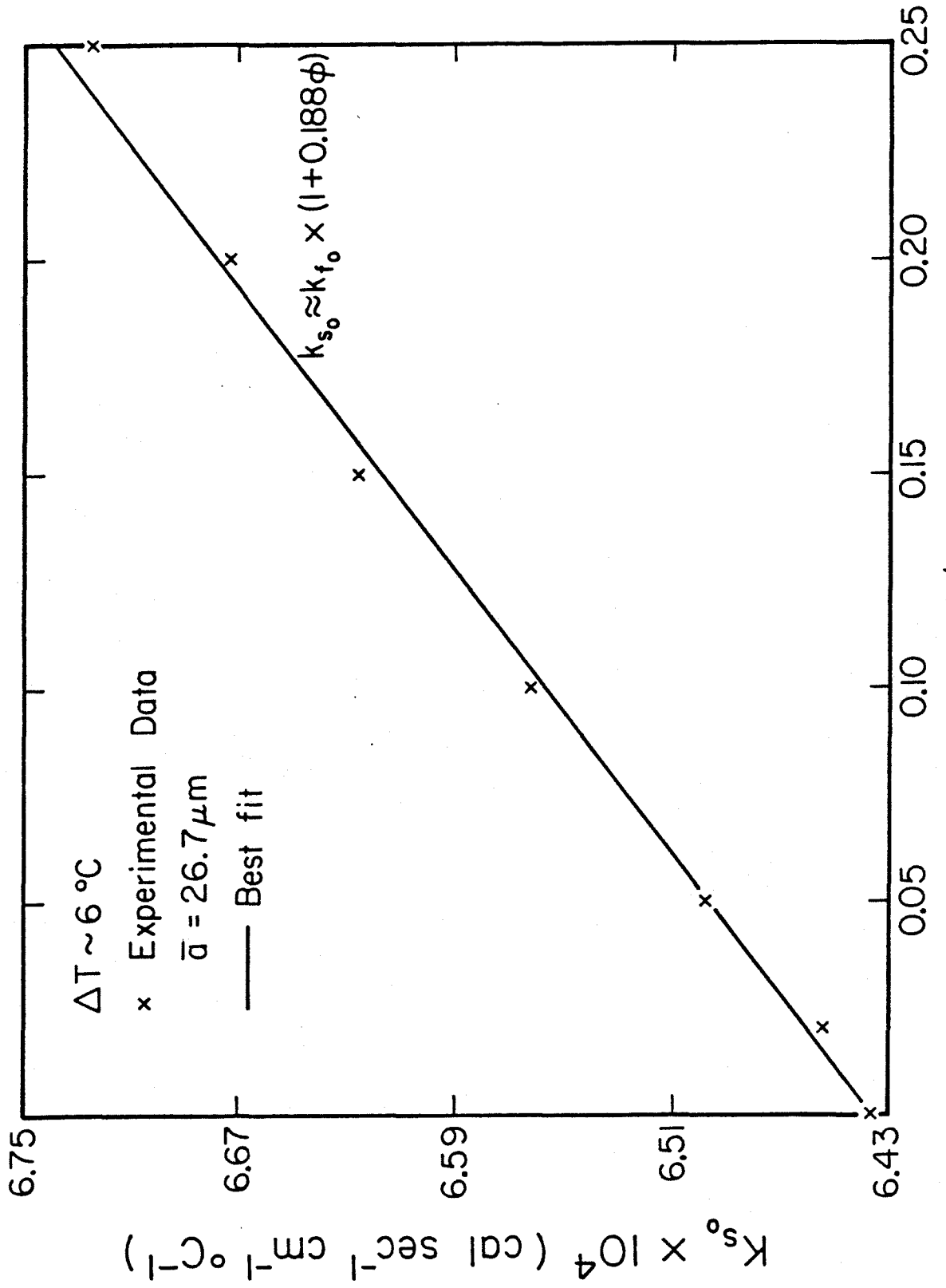
$K_{s_o} \times 10^4$ (cal sec^{-1} cm^{-1} °C^{-1})
6.75
6.67
6.59
6.51
6.43
0.05
0.10
0.15
0.20
0.25
ϕ
$k_{s_o} \approx k_{f_o} \times (1+0.188\phi)$
$\Delta T \sim 6$ °C
× Experimental Data
$\bar{a} = 26.7\mu m$
Best fit

Figure 8

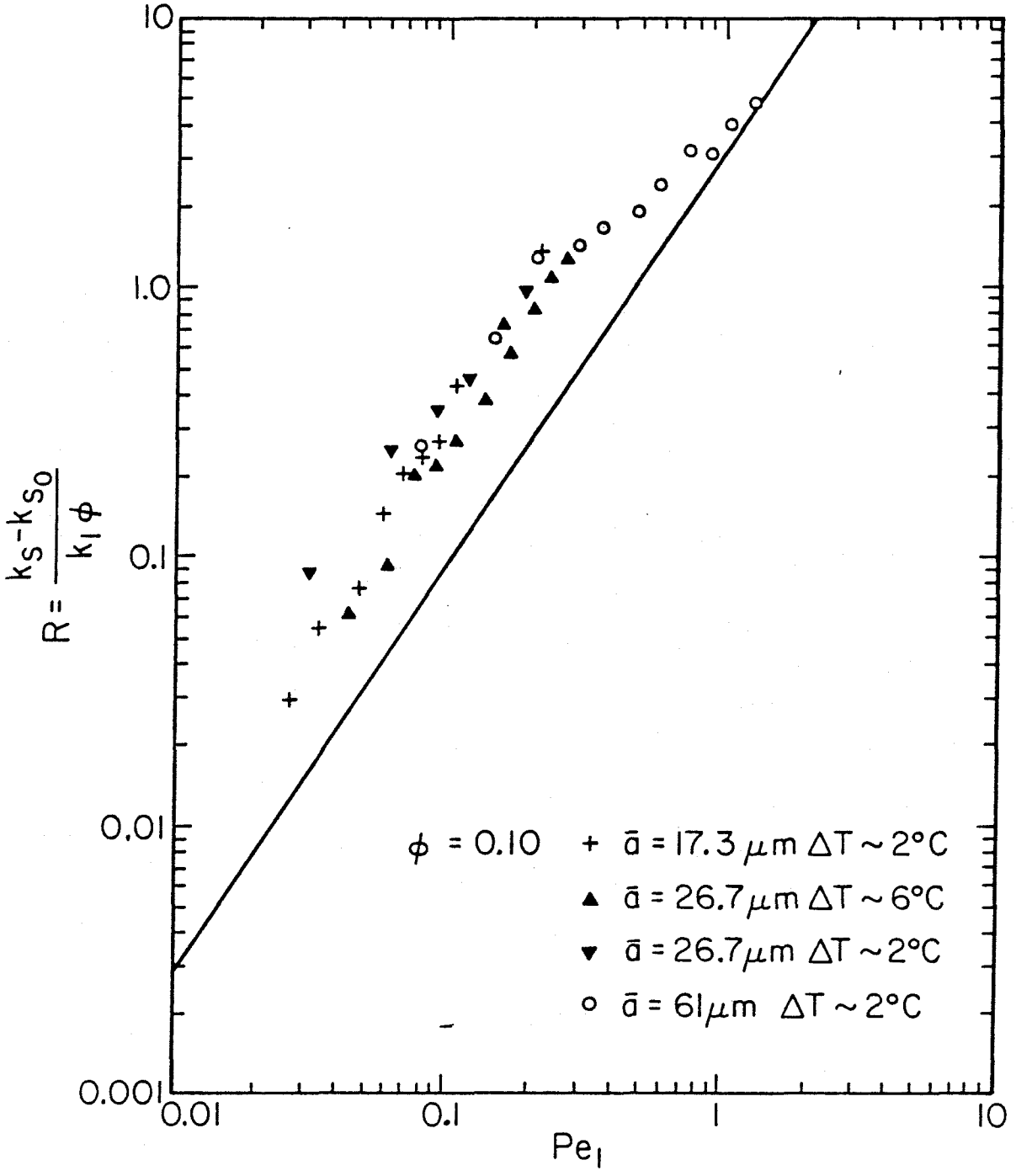
10
1.0
0.1
0.01
0.001
0.01
0.1
1
10
$R = \frac{k_S - k_{S_0}}{k_1 \phi}$
Pe_1
ϕ = 0.10
+ $\bar{a}$ = 17.3 μm $\Delta T \sim 2°C$
▲ $\bar{a}$ = 26.7 μm $\Delta T \sim 6°C$
▼ $\bar{a}$ = 26.7 μm $\Delta T \sim 2°C$
○ $\bar{a}$ = 61 μm $\Delta T \sim 2°C$

Figure 9

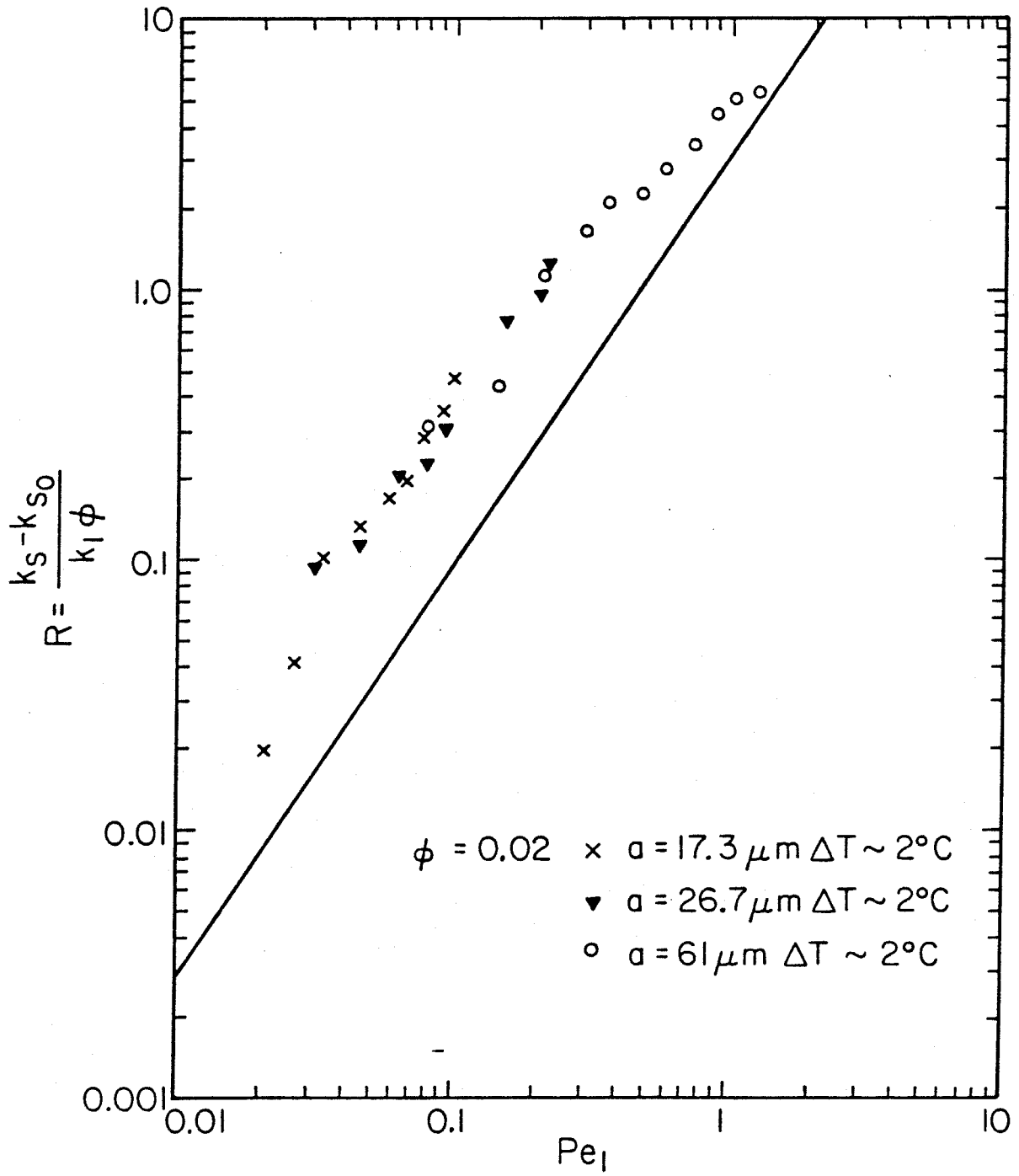
10
1.0
0.1
0.01
0.001
0.01
0.1
1
10
$R = \frac{k_s - k_{so}}{k_l \phi}$
Pe_l
ϕ = 0.02 × a = 17.3 μm ΔT ~ 2°C
▼ a = 26.7 μm ΔT ~ 2°C
○ a = 61 μm ΔT ~ 2°C

Figure 10

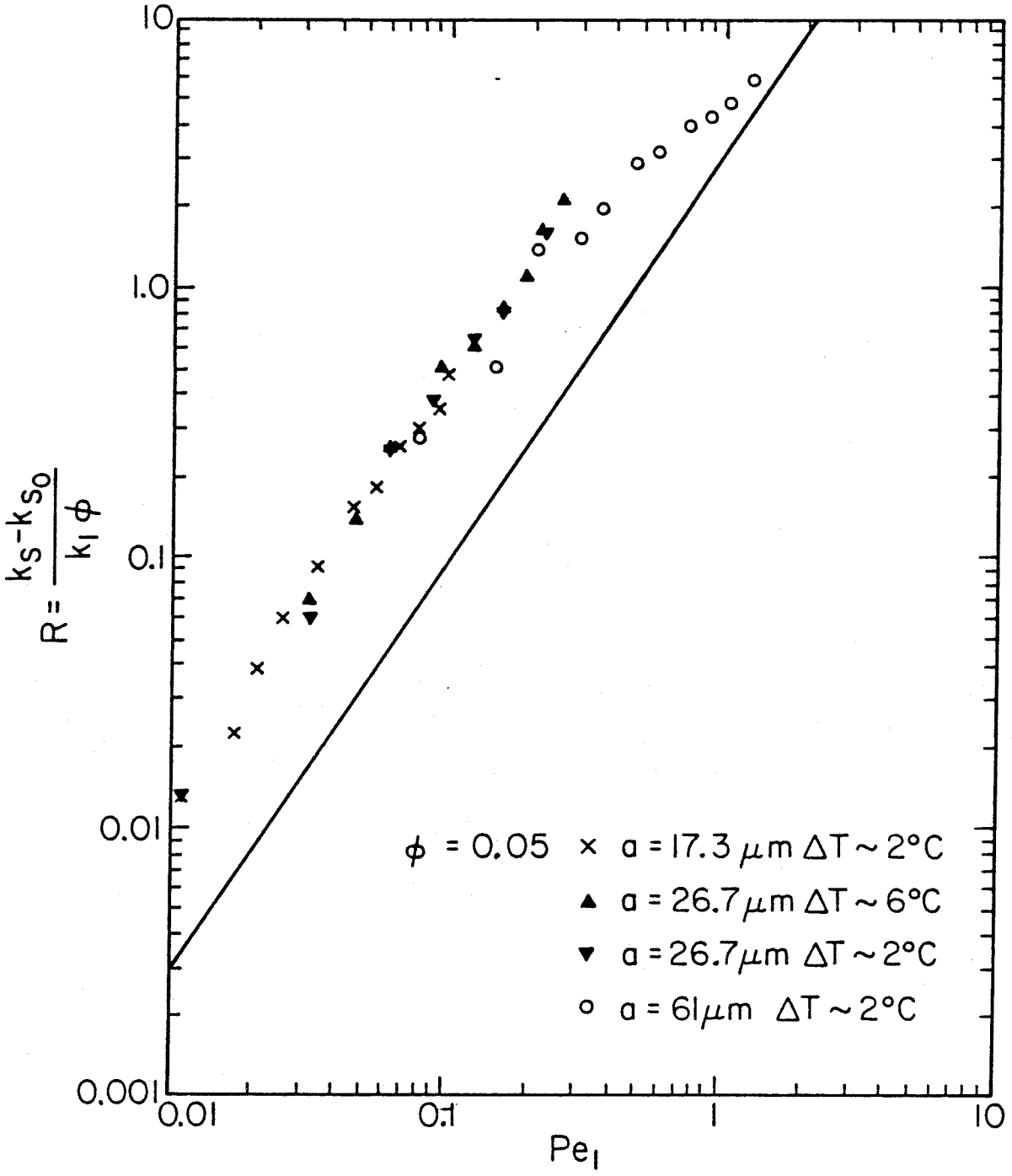
10
1.0
0.1
0.01
0.001
0.01
0.1
1
10
$R = \frac{k_S - k_{S_0}}{k_l \phi}$
Pe_l
ϕ = 0.05 × a = 17.3 μm ΔT ~ 2°C
▲ a = 26.7 μm ΔT ~ 6°C
▼ a = 26.7 μm ΔT ~ 2°C
○ a = 61 μm ΔT ~ 2°C

Figure 11

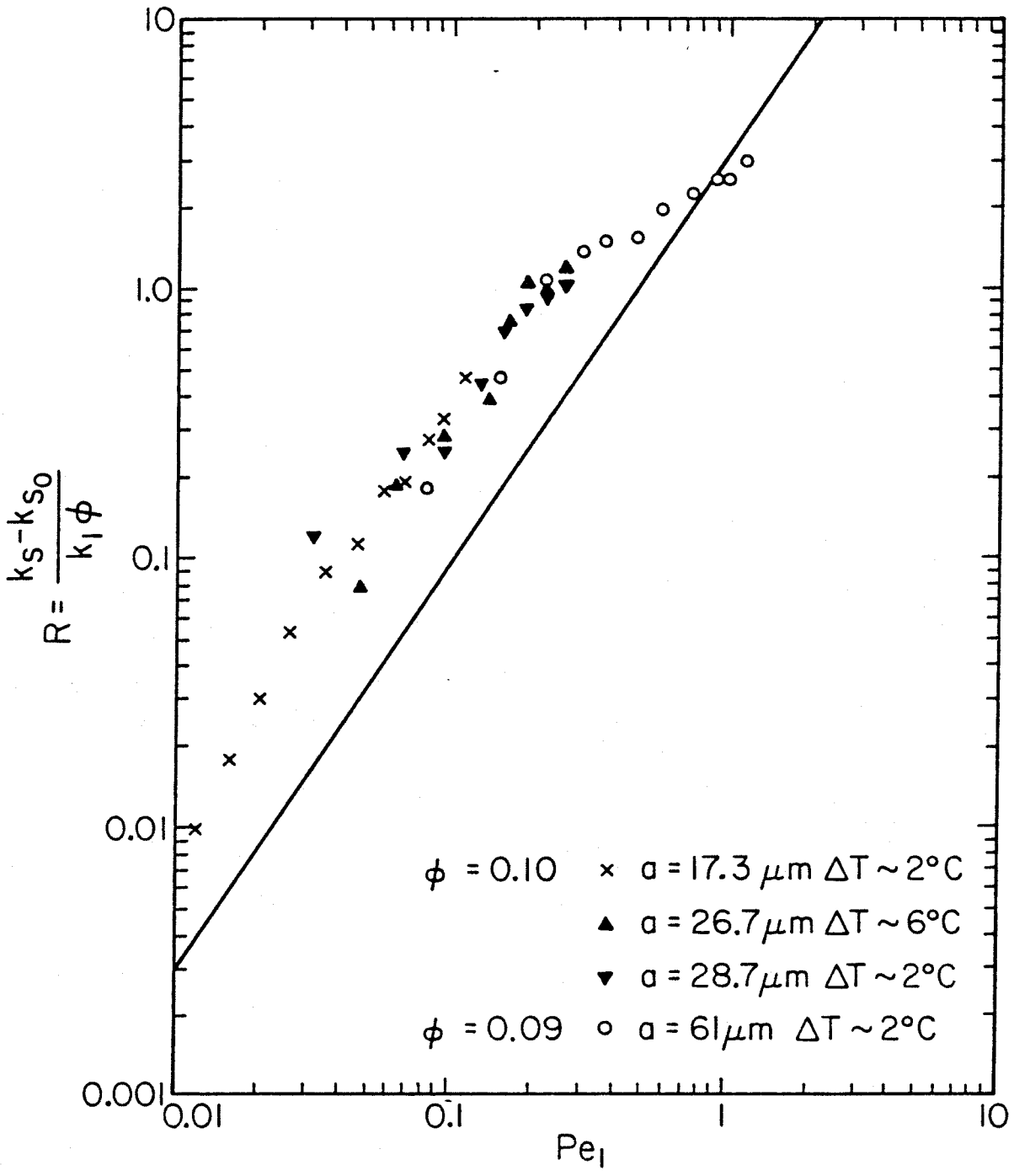
10
1.0
0.1
0.01
0.001
0.01
0.1
1
10
$R = \frac{k_s - k_{s_0}}{k_1 \phi}$
Pe_1
ϕ = 0.10 × a = 17.3 μm ΔT ~ 2°C
▲ a = 26.7 μm ΔT ~ 6°C
▼ a = 28.7 μm ΔT ~ 2°C
ϕ = 0.09 ○ a = 61 μm ΔT ~ 2°C

Figure 12

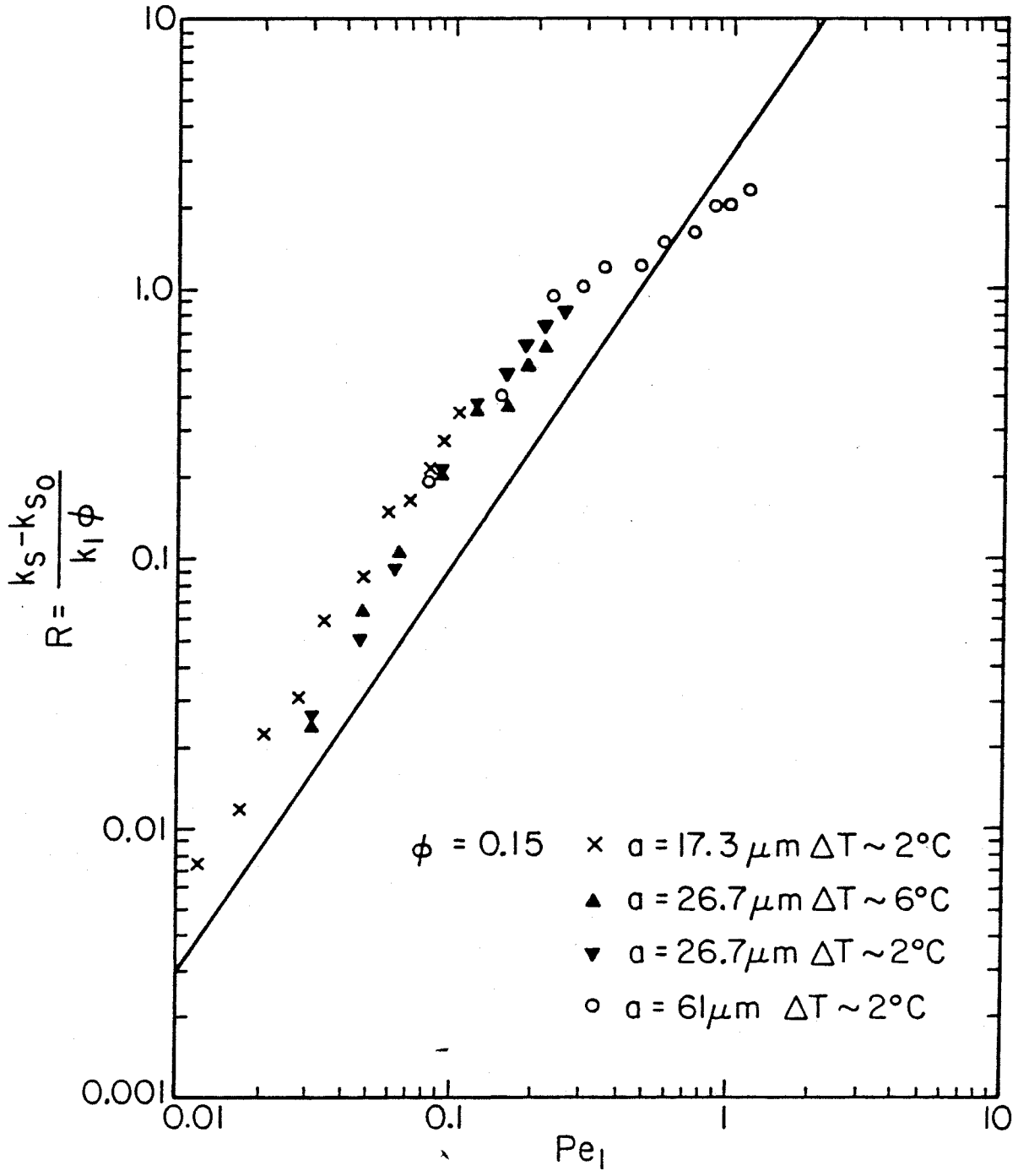
10
1.0
0.1
0.01
0.001
0.01
0.1
1
10
$R = \frac{k_S - k_{S0}}{k_l \phi}$
Pe_l
ϕ = 0.15
× a = 17.3 μm ΔT ~ 2°C
▲ a = 26.7 μm ΔT ~ 6°C
▼ a = 26.7 μm ΔT ~ 2°C
○ a = 61 μm ΔT ~ 2°C

Figure 13

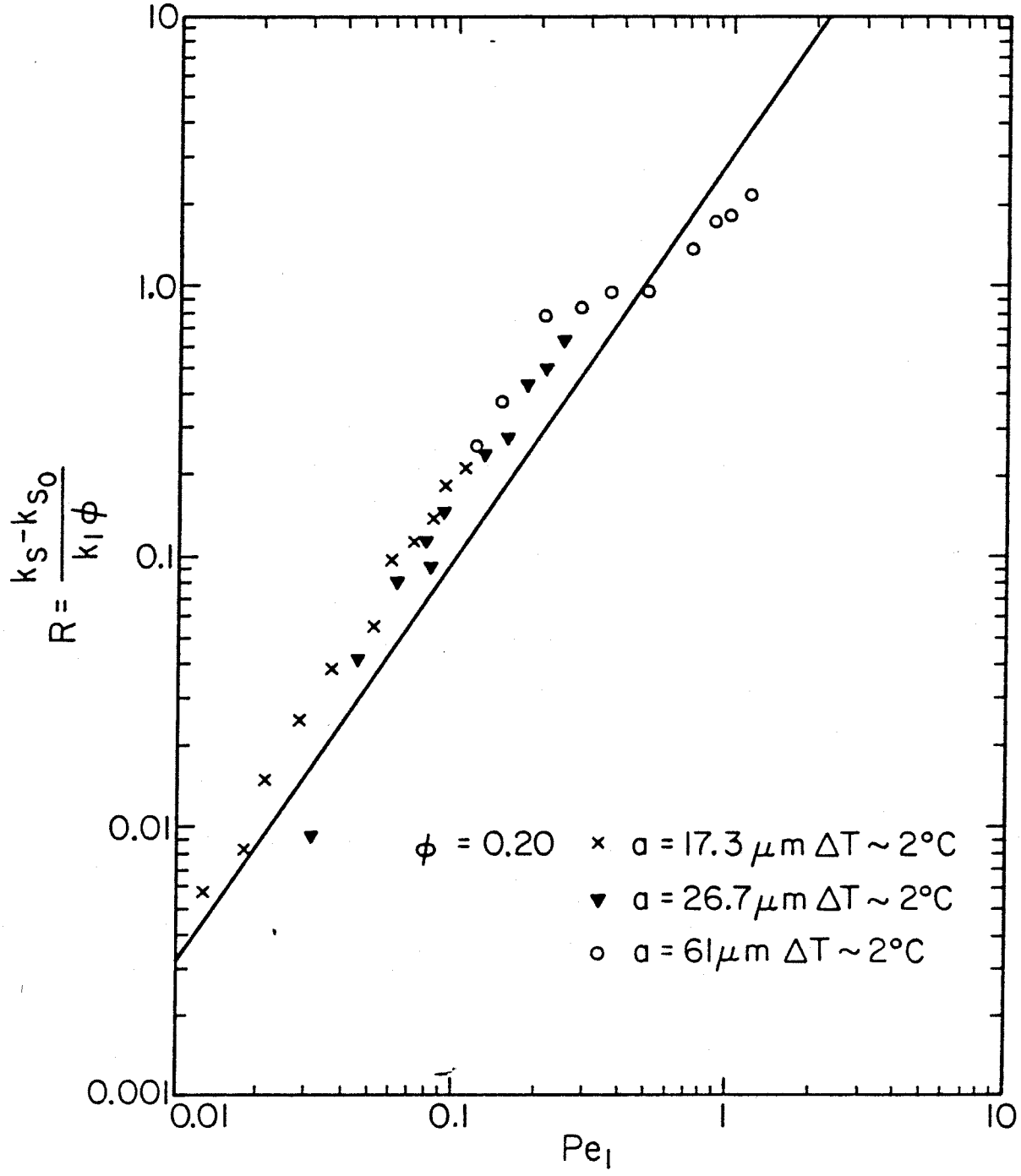
10
1.0
0.1
0.01
0.001
0.01
0.1
1
10
$R = \frac{k_s - k_{s_0}}{k_1 \phi}$
Pe_1
ϕ = 0.20 × a = 17.3 μm ΔT ~ 2°C
▼ a = 26.7 μm ΔT ~ 2°C
○ a = 61 μm ΔT ~ 2°C

Figure 14

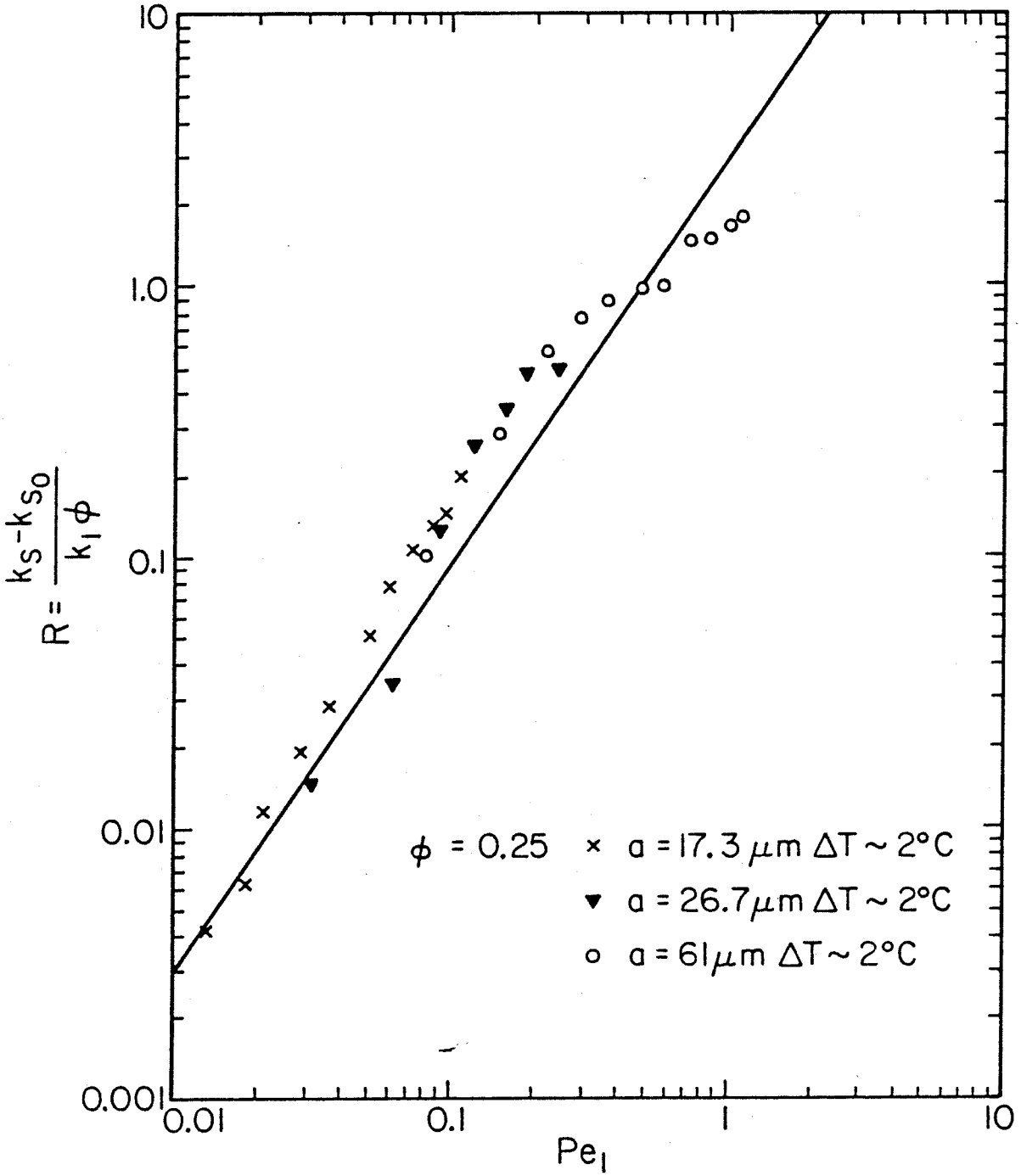
10
1.0
0.1
0.01
0.001
0.01
0.1
1
10
$R = \frac{k_s - k_{s0}}{k_1 \phi}$
Pe_1
ϕ = 0.25
× a = 17.3 μm ΔT ~ 2°C
▼ a = 26.7 μm ΔT ~ 2°C
○ a = 61 μm ΔT ~ 2°C

Figure 15

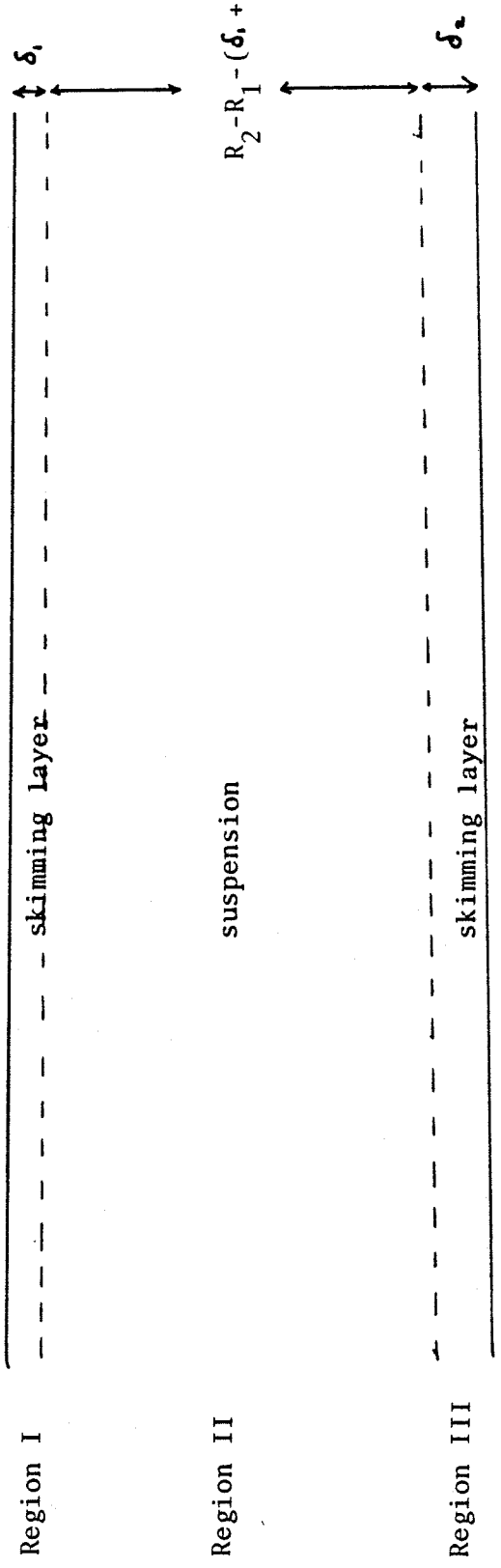

Fig. D1: Schematic of Skimming Layers

Part III: Fluorescence Correlation Spectroscopy

This is an analysis of the application of fluorescence correlation spectroscopy to measure molecular diffusion and velocity fields in a flowing system. The method, first proposed by Elson and Madge (1974), was designed to characterize molecular diffusivity and chemical kinetics in stationary systems by measurements made at thermodynamic equilibrium. Essentially, the method makes use of the fact that the components of the system, even at equilibrium,are continually fluctuating about their thermodynamic-mean concentrations. The fluctuations are due to random variations in the number of molecules which enter or leave the observed region by diffusion or chemical reaction. Since the same phenomenological diffusion and chemical rate coefficients which describe the rates at which the system returns to equilibrium after a macroscopic perturbation of its state also describe the rates at which spontaneous fluctuations decay, observations of these spontaneous fluctuations can give the phenomenological rate coefficients equivalent to those obtained by conventional means. With this method, these coefficients are determined without disturbing the equilibrium of the system. The number of molecules of a specified type is measured in a defined open volume of solution as a function of time. From the average time behavior of spontaneous concentration fluctuation, the rate coefficients can be derived. The principle of this method is therefore analogous to the method of quasi-elastic light scattering. The use of fluorescent molecules, however, allows the identification of specific molecules from the emission spectrum of fluorescence and, by choosing fluorescent dyes of high quantum yield, provides a much more sensitive indication to fluctuations in concentration. Quasi-elastic light scattering, on the other hand, depends on the fluctuations of the refractive index of

the medium, and is much less sensitive to different types of molecules. All molecules of similar size scatter light to more or less the same extent so long as the frequency of the incident light is not near a resonant absorption. As a result, it is difficult to use quasi-elastic light scattering to measure the diffusivity of a specified component in a multicomponent system or to study chemical kinetics of complex reactions. The important advantage in measuring concentration by way of properties like fluorescence and absorbance is the chemical specificity which results from their spectral properties.

Subsequently, Berne and Pecora (1976) extended the analysis of Elson and Madge to flowing systems and demonstrated the applicability of the method to measure velocity fields as well. Berne and Pecora showed that the average time behavior of deviations from the thermodynamic mean number is strongly dependent on the flow fields. Therefore, the velocity field can also be measured from the stochastic time record of this deviation. Berne and Pecora, however, only considered the bulk velocity components and did not consider the effect of velocity gradients that might be present in the flow system.

In the analysis presented here,[†] the effect of the velocity gradient is considered. The motivation in performing this analysis was to realize an experimental method to study local material transport in a system undergoing simple shear, a problem analogous to the experimental study (Part II) undertaken in this research program on heat transfer in suspensions undergoing simple shear flow. Due to the lack of any appropriate experimental

[†]The author was not aware of the work of Berne and Pecora when this analysis was undertaken.

technique, only measurements on the macroscopic heat transfer were made in the experimental study. For the experimental conditions used, it was determined that the effect of the variation of the local shear rate was unimportant and that the result could be adequately correlated with the average shear rate of the system. This statement, however, is not true in general. An experimental method that allows measurements on the local scale is therefore desirable.

As stated above, a simple shear flow was employed in this analysis. This choice was directed towards the need of this research program. It should be noted that by choosing a sufficiently small local scale, it is often sufficient to represent the local velocity distribution by a simple shear flow. The analysis presented here can also be extended to velocity fields of multicomponents but was not made.

In this present derivation, a component that fluoresces when excited is considered. A laser beam with an appropriate frequency is used as the source of excitation. The z-axis of the coordinates is chosen to be along the axis of propagation and in the center of the incident beam of light. The dimensions of the system in the x and y directions are much larger than the diameter of the beam. The fluorescence is observed along the z-direction through a slit which admits a Gaussian spatial profile of width w_2, while the beam has a Gaussian spatial profile in the x and y directions of width w_1. The illuminated volume can therefore be represented by

$$I(\vec{r}) = I_o \exp - \frac{(x^2 + y^2)}{2w_1^2} \exp \frac{-z^2}{2w_2^2}$$

If $c(\vec{r},t)$ is the concentration (in number of molecules per unit volume) of the component under consideration at position $\vec{r}$ and time t,

its thermodynamic mean,

$$\bar{c} = \langle c(r,t) \rangle$$

is independent of position and time. The fluctuation at $\vec{r}$ and t is

$$\delta c(\vec{r},t) = c(\vec{r},t) - \bar{c}. \tag{1}$$

The concentration $c(\vec{r},t)$ and its fluctuation are detected from the anode current of the photodetector, i(t):

$$i(t) = g\varepsilon Q \int I(\vec{r})c(\vec{r},t)d^3\vec{r} \tag{2}$$

The fluctuations in i(t), $\delta i(t)$, is therefore given by

$$\delta i(t) = g\varepsilon Q \int I(\vec{r})\delta c(\vec{r},t)d^3\vec{r} \tag{3}$$

The factor g accounts for the quantum efficiency and gain of the photodetector as well as geometric and optical filtering losses inherent in the experimental arrangement, while ε and Q are the optical extinction coefficient and fluorescent quantum yield of the component measured at the excitation and emission wavelengths appropriate to experiment. The low concentration of absorbing solutes ensures that the intensity is essentially constant along the z-axis.

For the case of a simple shear flow in two dimensions, the velocity field can be represented by

$$u = u_x = u_o + \gamma z \tag{4}$$

where u_o = velocity at the center of the illuminated volume, and

γ = shear rate.

The light beam is therefore positioned in the direction of the velocity gradient.

With the above velocity field, the governing equation for δc is

$$\frac{\partial(\delta c)}{\partial t} + (u_o + bz)\frac{\partial(\delta c)}{\partial x} = D\bar{v}^2(\delta c) \tag{5}$$

with the boundary conditions

$$\delta c \to 0 \qquad \text{as} \qquad x,y,z \to \infty \tag{6}$$

The boundary conditioned, derived from Eq. (3), is possible as δc is observed through δi. Eq. (5) is solved by using Fourier transform:

$$\tilde{c}(t,\vec{\nu}) = F_\nu(\delta c) = \int_{-\infty}^{\infty}\int\int dxdydz\ \exp[i(x\nu_x + y\nu_y + z\nu_z)](\delta c) \tag{7}$$

where $\vec{\nu} = (\vec{\nu}_x,\vec{\nu}_y,\vec{\nu}_z)$.

The inverse transform is

$$\delta c(t,\vec{r}) = F_r^{-1}(\tilde{c}) = \int_{-\infty}^{\infty}\int\int d\nu_x d\nu_y d\nu_z\ \exp[-i(x\nu_x + y\nu_y + z\nu_z)]\tilde{c} \tag{8}$$

Applying the transform to Eq. (5) yields the following first-order partial differential equation:

$$\frac{\partial\tilde{c}}{\partial t} - \gamma\nu_x\frac{\partial\tilde{c}}{\partial\nu_z} = -(D\nu^2 + iu_o\nu_x)\tilde{c} \tag{9}$$

where $\nu^2 = \nu_x^2 + \nu_y^2 + \nu_z^2$.

By applying the method of characteristics (Webster, 1933), the solution to Eq. (9) is

$$\tilde{c} = \tilde{c}_o\exp\left[-t(D\nu^2 + D\gamma\nu_x\nu_z t + iu_o u_x + \frac{1}{3}D\gamma^2\nu_x^2 t^2)\right] \tag{10}$$

Defining the concentration correlation function as

$$\phi(\vec{r},\vec{r}',t) = <\delta c(\vec{r},t)\delta c(\vec{r}',t+\tau)> ,$$

ϕ can be rewritten as

$$\begin{aligned}\phi &= \langle \delta c(\vec{r},t)\delta c(\vec{r}',t+\tau)\rangle \\ &= \langle \delta c(\vec{r},o)\delta c(\vec{r}',\tau)\rangle \\ &= F^{-1}_{r'}\left\{\exp\left[-t(D\nu^2 + D\gamma\nu_x\nu_z t + \tfrac{1}{3}D\gamma^2\nu_x^2 t^2)\right] \times F_\nu\left[\phi(\vec{r},\vec{r}'',o)\right]\right\}\end{aligned} \tag{11}$$

For the random fluctuations, the following expression can be written without loss of generality:

$$\phi(\vec{r},\vec{r}',o) = \langle \delta c(\vec{r},o)\delta c(\vec{r}',o)\rangle = A\underline{\delta}(\vec{r} - \vec{r}')$$

where $\underline{\delta}$ is the Dirac function and A a constant. Eq. (11) then becomes

$$\begin{aligned}\phi(\vec{r},\vec{r}',t) = A_1 F^{-1}_{r'}\Big\{&\exp\left[-t(D\nu^2 + D\gamma\nu_x\nu_z t + iu_o\nu_x + \tfrac{1}{3}D\gamma^2\nu_x^2 t^2)\right] \\ &\times \exp\left[i(\nu_x x + \nu_y y + \nu_z z)\right]\Big\}\end{aligned} \tag{12}$$

where A_1 = constant.

With Eq. (12), the temporal autocorrelation of the photocurrent, $G(\tau)$, can be evaluated:

$$\begin{aligned}G(\tau) &= \langle \delta_i(o)\delta i(\tau)\rangle \\ &= A_2 \int I(\vec{r})I(\vec{r}')\phi(\vec{r},\vec{r}',\tau)d^3\vec{r}d^3\vec{r}'\end{aligned} \tag{13}$$

where A_2 = constant.

$G(\tau)$ is therefore given by:

$$G(\tau) = A_3 \int_{\infty}^{\infty} \left\{ \int\int\int_{-\infty}^{\infty} d\nu_x d\nu_y d\nu_z \exp\left[-\tau(D\nu^2 + D\gamma\nu_x\nu_z\tau + iu_o\nu_x + \frac{1}{3}D\gamma^2\nu_x^2\tau^2)\right] \right.$$

$$\left. \times \exp\left[-i(x'\nu_x + y'\nu_y + z'\nu_z)\right] \exp\left[i(\nu_x x + \nu_y y + \nu_z z)\right] \right\}$$

$$\times \exp\left[-\frac{(x^2 + y^2)}{2w_1^2}\right] \exp\left[-\frac{(x'^2 + y'^2)}{2w_1^2}\right] \exp\left[-\frac{(z^2 + z'^2)}{2w_2}\right] dx\,dy\,dz\,dx'\,dy'\,dz'$$

$$= A_4 \frac{1}{\left(1 + \frac{\tau}{\tau_2}\right)^{\frac{1}{2}}} \frac{1}{\left(1 + \frac{t}{\tau_1}\right)^{\frac{1}{2}}} \frac{\exp\left\{-(t/\tau_3)^2 \Big/ 4 \left[\frac{1}{\tau_1\tau_2} \frac{\gamma^2\tau^4}{\left(\frac{\tau}{\tau_2} + 1\right)} + \frac{\tau}{\tau_1} + \frac{1}{3}\frac{\gamma^2\tau^3}{\tau_1} + 1\right]\right\}}{\left[\frac{\gamma^2\tau^4}{\tau_1\tau_2\left(\frac{\tau}{\tau_2} + 1\right)} + \frac{\tau}{\tau_1} + \frac{1}{3}\frac{\gamma^2\tau^3}{\tau_1} + 1\right]^{\frac{1}{2}}} \tag{14}$$

The characteristic times τ_1, τ_2 and τ_3 are defined as

$$\tau_1 = \frac{w_1^2}{4D}, \quad \tau_2 = \frac{w_2^2}{4D}, \quad \tau_3 = \frac{w_1}{u_o}$$

For $\gamma = 0$, this result reduces to that of Berne and Pecora (1976).

Typically, D is of the order of 10^{-6} cm^2 sec^{-1}, while $w_1 \sim 5 \times 10^{-4}$ cm and $w_2 \sim 10^{-2}$ cm. For these values,

$\tau_1 \sim 6 \times 10^{-2}$ sec and $\tau_2 \sim 25$ sec.

For experimental purposes, τ is typically less than 1 sec. Eq. (14) can therefore be simplified and rewritten as

$$G(\tau) \approx A_4 \frac{1}{\left[1 + \frac{\tau}{\tau_1}\right]^{\frac{1}{2}}} \frac{\exp\left\{-(\tau/\tau_3)^2 \Big/ 4 \left[\frac{\tau}{\tau_1} + \frac{1}{3}\frac{\gamma^2\tau^3}{\tau_1} + 1\right]\right\}}{\left[\frac{\tau}{\tau_1} + \frac{1}{3}\frac{\gamma^2\tau^3}{\tau_1} + 1\right]^{\frac{1}{2}}} \tag{15}$$

By using different τ's in the experiment, Eq. (15) can be used to measure τ_1, τ_3 or γ or a combination of these parameters. This point is demonstrated briefly in the following:

First, ignore the presence of u_o and compare the characteristic times τ_1 and $\frac{1}{\gamma}$:

The effect of γ is unimportant if

$$\frac{\tau}{\tau_1} >> \frac{1}{3}\frac{\gamma^2\tau^3}{\tau_1} \quad ,$$

which implies that γ can be ignored if τ satisfies

$$\tau << \left(\frac{3}{\gamma}\right)^{\frac{1}{2}} \tag{16}$$

Now, ignore the presence of γ and compare the characteristic times τ_1 and τ_3:

τ_3 is unimportant if

$$\frac{\tau}{\tau_3} << 1.$$

Equivalently, the effect of bulk flow can be ignored if the time of experimentation τ satisfies

$$\tau << \frac{w_1}{u_o} \tag{17}$$

By using the smaller of the two τ's in Eq. (16) and (17), the characteristic time τ_1, and therefore D, can be measured directly.

Similar comparisons can be made to determine the necessary τ to measure the other characteristic times. In doing so, the same experiment can be used to measure the various characteristic times simultaneously.

References

Berne, B. J., Pecora, R., 'Dynamic Light Scattering - With Applications to Chemistry, Biology and Physics,' - Wiley, N.Y., 1976.

Elson, E. L., Madge, D., 'Fluorescence Correlation Spectroscopy. I. Conceptual Basis and Theory.' Biopolymers 13, pp. 1-27, 1974.

Webster, 'Partial Differential Equations of Mathematical Physics' - Stechert and Co., New York (1933).